Multi-Telescope Studies of Neutron Stars

INAUGURAL-DISSERTATION

zur
Erlangung des Doktorgrades
der Mathematisch-Naturwissenschaftlichen Fakultät
der Universität zu Köln

vorgelegt von

Kosmas Lazaridis

aus Thessaloniki, Griechenland

Köln 2009

Abstract

Neutron stars are unique stellar remnants with extreme properties, as their density and magnetic field. Their study can be the key to a number of unanswered problems in fundamental physics and astronomy, ranging from stellar evolution to strong field gravity. One of the best ways of studying these objects is with observations at radio wavelengths, the efficiency of which can be vastly improved with the combination of data from multiple radiotelescopes. In this thesis, we use the largest European radiotelescopes for performing high quality studies of the properties of objects belonging into two separate categories of neutron stars, millisecond pulsars and magnetars.

In the first part of this thesis (Chapter 2), a complete description of the observing systems and calibration procedures for the multiple telescopes used is presented. Specifically, all observations were made with the European Pulsar Timing Array (EPTA) telescopes, which are the Effelsberg 100m radiotelescope in Germany, the Lovell 76m radiotelescope in UK, the Westerbork 94m equivalent synthesis radiotelescope in the Netherlands and the Nançay 94m equivalent decimetric radiotelescope in France. In addition, the different procedures for the data acquisition and improvement of the latest and archival data of the Effelsberg radiotelescope are described. Finally, the techniques and advantages of the combination of multi-telescope data sets are being presented.

In the second part of the thesis (Chapters 3 and 4) we concentrate on the study of millisecond pulsars using the pulsar timing technique. Specifically, we analyse a set of 15 millisecond pulsars from the Effelsberg source list, showing that most of them are good candidate sources for the EPTA efforts to detect gravitational waves in the nano-Hertz regime. We present, in most cases only for the Effelsberg data set, improved preliminary results for their astrometric, spin and binary parameters. Finally, we report on the complete timing analysis of one of these sources. Specifically, we present results from the high precision timing analysis of the pulsar-white dwarf binary PSR J1012+5307 using 15 years of EPTA multi-telescope data. All the timing parameters have been improved from the previously published values, at least by an order of magnitude. In addition, a parallax measurement is obtained for the first time for PSR J1012+5307, being consistent with previous optical estimations from the WD companion. Combining improved 3D velocity information and models for the Galactic potential the complete evolutionary Galactic path of the system is obtained. While a new intrinsic eccentricity upper limit is acquired, being one of the smallest calculated for a binary system and providing evidence for the stellar evolution of this system, a measurement of the variation of the projected semi-major is also constraining the systems orbital orientation for the first time. Finally, combining the fact that PSR J1012+5307 is an ideal laboratory for testing alternative theories of gravity, with a measurement for the first time of the change of the orbital period of the system, stringent, general, theory independent upper limits for the dipole gravitational wave emission and the variation of the gravitational constant are being derived.

In the final part of this thesis (Chapter 5), we study the category of magnetars and specifically the case of the first radio emitting anomalous X-ray pulsar (AXP) J1810-197. With a simultaneous and quasi-simultaneous multi-frequency and multi-telescope campaign from July 2006 until July 2007 we obtained flux density measurements and spectral features of this 5.5-sec radio-emitting magnetar. We monitored the spectral evolution of its pulse shape which consists of a main pulse (MP) and an interpulse (IP). We present the flux density spectrum of the average profile and of the separate pulse components. We observe a decrease of the flux density by a factor of 10 within 8 months and follow the disappearance of one of the two main components. Although the spectrum is generally flat, we observe large fluctuations of the spectral index with time. We conclude that AXP J1810-197 is not like any other radio pulsar we know with spectral properties and temporal fluctuations differing remarkably from normal pulsars. Significant variability exists on all considered time scales, from pulse to pulse, day-to-day and over the time of weeks and months. Analysis of the interstellar scintillation for AXP J1810-197 shows that only some of the variability is affected by scintillations and most of it is due to intrinsic variations, better described by a model of turbulent magnetosphere. Further analysis on the single pulse properties of AXP J1810-197 confirms these results.

Zusammenfassung

Neutronensterne sind eine besondere Gruppe von Sternüberresten, die sich durch extreme Dichten und Magnetfelder auszeichnen. Die Erforschung von Neutronensternen kann der Schlüssel zur Lösung einer großen Anzahl ungeklärter Fragen der Physik und der Astronomie sein. Diese umfassen das Gebiet der Sternentwicklung ebenso wie das der Eigenschaften starker Gravitationsfelder. Die Radioastronomie bietet eine der besten Studienmöglichkeiten für diese Objekte. Die Kombination der Beobachtungen mehrerer Radioobservatorien kann dabei eine große Effizienzsteigerung bewirken. In dieser Dissertation werden Beobachtungen an Europas größten Radioteleskopen kombiniert um die Eigenschaften von zwei Klassen von Neutronensternen, die der Millisekundenpulsare und die der Magnetare zu untersuchen.

Das erste Kapitel beschreibt die Beobachtungssysteme und die Kalibrationsverfahren der verschiedenen Teleskope. Alle Beobachtungen wurden an Teleskopen durchgeführt, die zum "European Pulsar Timing Array" (=EPTA) gehören. Es handelt sich dabei um das deutsche 100m Radioteleskop in Effelsberg, das britische 76m Lovell Teleskop in Jodrell Bank, das niederländische Westerbork Interferometer mit einer Sammelfläche, die einem 94m Spiegel entspricht und nicht zuletzt das etwa gleich große französische Dezimeterteleskop in Nançay. Weiterhin werden die verschiedenen Verfahren der Datenerfassung und die Verbesserung der Datenauswertung der Effelsbergdaten beschrieben. Dieser Teil der Dissertation endet mit einer Beschreibung des Verfahrens zur Kombination von Messdaten verschiedener Observatorien und der Vorteile die dadurch entstehen.

Der zweite Teil der Dissertation ist dem Studium von Millisekundenpulsaren mittels der präzisen Messung der Pulsankunftzeiten gewidmet. Es wurden 15 Millisekundenpulsare aus der Liste der in Effelsberg regelmäßig beobachteten Quellen untersucht. Dabei zeigte sich, daß die meisten gute Kanditaten für die EPTA Suche nach Gravitationswellen im nano–Hertz Bereich sind. Für die meisten Objekte konnten wir allein schon durch sorgfältige Analyse der Effelsberg Daten verbesserte astrometrische, Spin- und Orbitparameter gewinnen. Abschließend wird in diesem Teil die vollständige Analyse der Kombination aller verfügbaren Messdaten vorgestellt. Hier sind insbesondere die neuen Ergebnisse für das weiße Zwerg–Pulsar System PSR J1012+5307, die aus EPTA Daten die einen Zeitraum von 15 Jahren überdecken, gewonnen wurden, zu erwähnen. Alle Pulsar- und Orbitparameter konnten im Vergleich zur Literatur um wenigstens eine Größenordung verbessert werden. Zum ersten Mal konnte auch die Parallaxe für PSR J1012+5307 gemessen werden. Der Wert steht im Einklang mit der optischen Entfernungsbestimmung des begleitenden weißen Zwergsternes. Die verbesserte Abschätzung der 3-D Eigenbewegung ergibt zusammmem mit den Modellen für das galaktische Potential eine Beschreibung der vergangenen Trajektorie des Objektes in unserer Milchstraße. Die verbesserte Bestimmung der Orbitalexzentrizität von PSR J1012+5307 ergibt, daß es sich hier um eines der Systeme kleinster Exzentrizität handelt, welches wichtige Implikationen für die Sternentwicklung in diesem weißer Zwerg–Pulsar System hat. Die erfolgreiche Messung

der Variation der Orbithauptachse konnte erstmalig eine Beschränkung der Orbitorientierung im Raum ermöglichen. Aus der Tatsache, daß PSR J1012+5307 ein idealer Testfall für alternative Gravitationstheorien darstellt, konnten im Zusammenhang mit der erstmaligen Bestimmung der Änderung der Bahnperiode neue Grenzwerte für die Stärke etwaiger gravitativer Dipolstrahlung ermittelt werden.

Der letzte Teil der Dissertation behandelt die Untersuchung von Magnetaren, insbesondere das Objekt AXP J1810−197, welches der erste anomale Röntgenpulsar ist, bei dem auch Radioemission beobachtet wurde. Simultane und quasi–simultane Multifrequenzmessungen an verschiedenen Teleskopen vom Juli 2006 bis Juli 2007 ergaben Aussagen über den Radiofluß und das Radiospektrum dieses Magnetars mit einer 5.5 Sekunden Rotationsperiode. Es wurden fequenzabhängige Veränderungen des Pulsprofiles, welches einen Haupt- und einen Interpuls aufweist, beobachtet. Der Radiofluß der Quelle änderte sich dabei in acht Monaten um einen Faktor zehn. Das Radiospektrum war im wesentlichen flach, zeigte aber auch zeitweise starke Fluktuationen des Spektralindexes. Wir folgern daraus, daß es sich bei AXP J1810−197 nicht um ein mit normalen Radiopulsaren vergleichbares Objekt handeln kann. Starke Variabilität wurde auf allen Zeitskalen, von Puls zu Puls bis hin zu Wochen und Monaten beobachtet. Eine Betrachtung des Beitrages der interstellaren Szintillation zeigt, daß diese nur zum kleinen Teil die Ursache für die beobachtete Veränderlichkeit sein kann. Die Variabilität rührt zumeist von inneren Fluktuationen her, wie sie in Modellen turbulenter Magnetosphären beschrieben werden. Eine weitergehende Analyse der Einzelpulseigenschaften von AXP J1810−197 hat das bestätigt.

Contents

List of Figures

List of Tables

1. Introduction to Neutron Stars

Astronomy compels the soul to look upwards and leads us from this world to another.

Plato

1.1 Neutron stars

The story begins in the lab of Chadwick (1932) where alpha particles produced in vacuum by the decay of the radioactive Polonium, hit a Beryllium target and a new particle was emitted (Figure 1.1)

$$^{4}He + {}^{9}Be \longrightarrow {}^{1}n + {}^{12}C. \tag{1.1}$$

With a mass a bit larger than proton's and no electric charge is being named neutron.
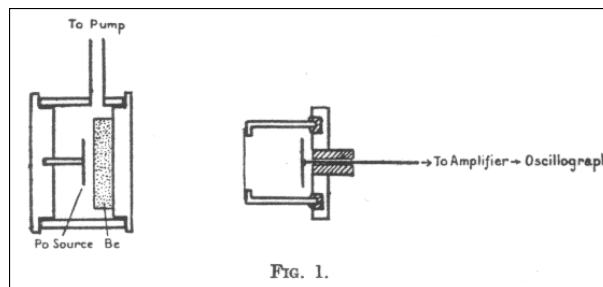
Figure 1.1: **Chadwick's experiment and the discovery of neutron.**

Two years later Baade & Zwicky (1934), in their effort to examine the origin of cosmic rays, suggest for the first time that a supernova represents the transition of an ordinary star into a neutron star. A star with very small radius and very high density. After analysing the structure of a star consisting of degenerate neutron gas Oppenheimer & Volkoff (1939) showed that the only important relationship in which the composition of these stars depends on is the one between pressure and density (Equation Of State (EOS)). Thus, knowledge of the EOS could lead to derivation of the mass and radius of a neutron star.

Today, we believe that a typical neutron star has (Lyne & Graham-Smith 2006) a radius of 10-20 km, a mass of $1.4\,M_{\odot}$ and mean density of $6.7 \times 10^{14}\,\mathrm{g}\ \mathrm{cm}^{-3}$ (similar to the density of nuclear matter $2.7 \times 10^{14}\,\mathrm{g}\ \mathrm{cm}^{-3}$). It consists of a neutron fluid in equilibrium with $\sim$5%

protons and electrons and an outer solid crystalline lattice (crust) of about 1 km thick, made of heavy nuclei on the surface and neutron rich heavy nuclei below.

Even though, the existence of neutron stars was predicted theoretically, it was not until 1967 that Jocelyn Bell and Antony Hewish (Hewish et al. 1968) discovered the first radio pulsar, while investigating the angular structure of compact radio sources, by observing the interplanetary scintillation with an array of 2048 dipoles in 16 rows of 128 elements at 81.5 MHz. C 1919+21 (PSR B1919+21) with a period of P=1.34 sec was the first pulsar discovered (Figure 1.2). The most important reason that pulsars were not discovered earlier is that their pulsations were confused with RFI. A property of the Hewish survey, was a short response time and a repetitive observing routine, virtue of which RFI could be discriminated against. The identification of pulsars with neutron stars has happened a bit earlier by Pacini (1967) and later by Gold (1968).
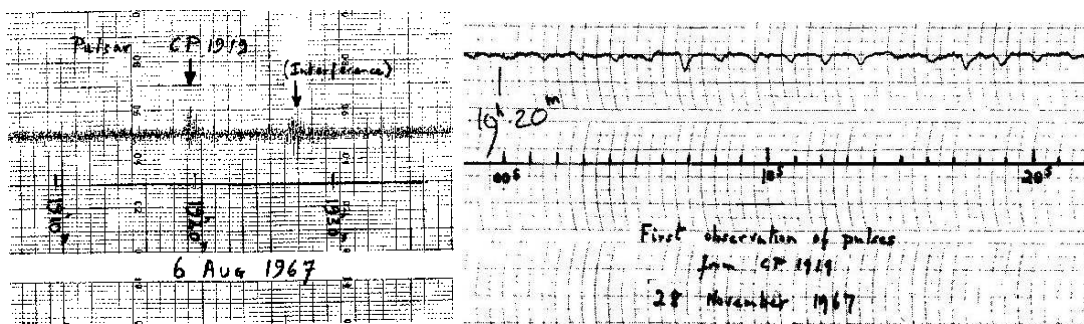
Figure 1.2: **Original paper charts. (Left) The discovery of the first pulsar PSR B1919+21. (Right) Single pulses from this pulsar.**

Pulsars (pulsating stars) are highly magnetised (dipolar magnetic field $\sim 10^{12}$ G) fast rotating neutron stars with a surface temperature of $10^6 - 10^7$ K, emitting narrow radio pulses along the magnetic axis (Figure 1.3). If Earth lies in the path of the beam of this "cosmic lighthouse" we can observe its pulses arriving on each rotation, reflecting its spin period. The pulse period
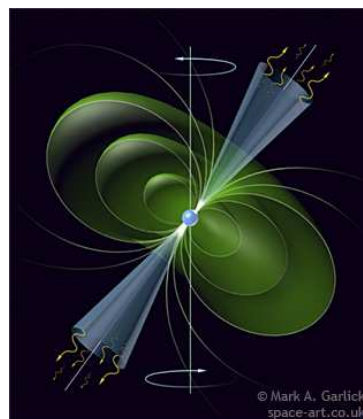
Figure 1.3: **Artistic impression of a pulsar (M. A. Garlick).**

of pulsars is increasing with time and can be connected to the rate of loss of rotational kinetic

energy or else the spin-down luminosity (total power output by the neutron star)

$$\dot{E} = -I\Omega\dot{\Omega} = 4\pi^2 I\dot{P}P^{-3}\,\mathrm{erg\,s^{-1}}, \tag{1.2}$$

(Lorimer & Kramer 2005) where $\Omega = 2\pi/P$ is the rotational angular frequency and I the moment of inertia. The age estimation of pulsars for a perpendicular dipole magnetic field (braking index $n = 3$) is

$$\tau_c = \frac{P}{2\dot{P}}, \tag{1.3}$$

(Lorimer & Kramer 2005) where τ_c is the characteristic age. Finally, the magnetic field strength at the surface of a typical neutron star with $I = 10^{45}$ g cm^2 and 10 km radius is

$$B = 3.2 \times 10^{19}\,\mathrm{G}\,\sqrt{P\dot{P}}, \tag{1.4}$$

(Lorimer & Kramer 2005) and called the characteristic magnetic field, where P is in seconds.

From the initial discovery until today many more steps have been taken in pulsar astronomy. In 1974, Hulse & Taylor (1974), discover the P=59 ms PSR B1913+16, a member of a neutron star binary system with an orbital period of 7.75 hours. In addition, they manage to measure variations of this orbital period. Specifically, the orbital shrinkage of 1 cm/day of this system (Figure 1.4) was proven to be caused by gravitational wave radiation (Weisberg & Taylor 1984), being the first experimental demonstration of gravitational waves existence.
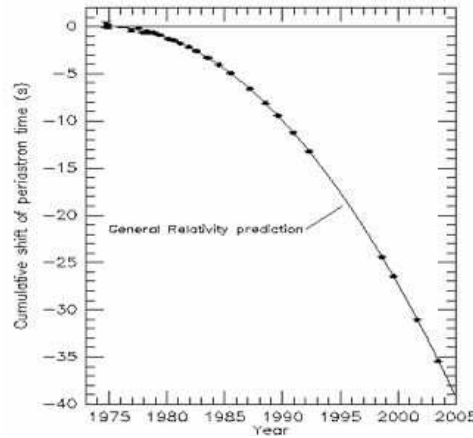
Figure 1.4: **Orbital decay of PSR B1913+16 (Weisberg & Taylor 2005). Periastron shifts caused by emission of gravitational radiation.**

Backer et al. (1982) discovered the fast rotating millisecond pulsar PSR B1937+21 with a period of 1.558 ms, reaching the theoretical rate that centrifugal forces balance gravitational forces at the surface of a neutron star. This discovery not only was important for setting limits on the equation of state of pulsars but initiated a new era in pulsar timing observations, since millisecond pulsars are extremely stable clocks. The technique of pulsar timing is the regular monitoring of the rotation of a neutron star by tracking the times of arrival (TOAs) of the radio pulses and will be described in the next chapter. Two years ago, the fastest rotating pulsar, PSR J1748-2446ad, was discovered by Hessels et al. (2006), with a period of P=1.396 ms.

Among other important discoveries over the years, such as the first extra-solar planets orbiting a pulsar (Wolszczan & Frail 1992) and the first and only double pulsar (Burgay et al. 2003; Lyne et al. 2004), is the one of a new category of neutron stars. Initially, Duncan & Thompson (1992) suggested the existence of magnetars, which are slowly rotating neutron stars with a rapid spin-down and emission powered by the decay of their extremely strong magnetic fields. Observations of the X-ray activity after a γ-ray burst from SGR 1806-20 revealed pulsed X-ray emission (Kouveliotou et al. 1998). This pulsed emission with a period of 7.47 sec and spin-down rate of 2.6×10^{-3} s/yr was suggesting a magnetic field of $B \sim 8 \times 10^{14}$ G, proving for the first time the existence of magnetars. Magnetars consist of the Soft Gamma-ray Repeaters (SGRs) and the Anomalous X-ray Pulsars (AXPs).

From 1967 until today around 1800 neutron stars have been detected, mostly along the galactic plane. In Figure 1.5 the $P - \dot{P}$ (period vs period derivative) diagram is presented, where all the distinct categories of neutron stars are plotted over lines of constant characteristic age, magnetic field strength and spin-down luminosity. One way of categorising the sample is as follows:

1) Young pulsars (upper left part): They spin fast (30 ms$\leq$P$\leq$0.5 s) and they are usually expected to be associated with supernova remnants. They are energetic and their magnetic field is $B \sim 10^{11} - 10^{14}$.

2) Normal pulsars (middle right part): They represent the biggest bulk of the population being $\sim$ 90% of all pulsars. They spin fast (30 ms$\leq$P$\leq$8.5 s) and they have a magnetic field of $B \sim 10^{11} - 10^{14}$ G.

3) Millisecond pulsars (lower left part): They spin very fast (1.397 ms$\leq$P$\leq$30 ms) and they are usually in binary systems. Their magnetic field is smaller ($B \sim 10^{8} - 10^{9}$) and they are very stable and accurate clocks.

4) Magnetars (upper right part): They are spinning slower (2 $\leq$P$\leq$12 sec) and they spin-down rapidly. Their magnetic field is very big (B$>10^{14}$ G) and its decay is powering their emission. They are rarely detected in radio while most often they emit in X-rays and usually in bursts.

A typical evolutionary scenario on the $P - \dot{P}$ diagram for a normal pulsar would be to be born with a short spin period (upper left part) followed by a rapid spin-down in the main bulk of the pulsars on a timescale of $10^5 - 10^6$ yr and finally becoming too faint to be detectable (cross over the graveyard) after 10^7 yr. As will be presented in the next section, if the pulsar is in a binary system it might come back from the "dead" as a millisecond pulsar (lower left part) with a slow spin-down, continuing to emit for a very long time.

1.2   Evolution of neutron stars and millisecond pulsars

A brief description of the most probable evolutionary scenarios for the formation of neutron stars and millisecond pulsars will be presented here (see Lorimer (2005) and references therein) following the steps of Figure 1.6.

Initially we have a binary star system where the primary, more massive star, has a mass range between 8 and 20-30 M$_\odot$ and the secondary has approximately a M$<$8 M$_\odot$. After the gravitational collapse of the primary star (since it is more massive it will exhaust more rapidly its core hydrogen), a neutron star is formed from a type II supernova explosion. If during the supernova explosion more than half of the pre-supernova mass is ejected from the system the latter will be separated with a high velocity neutron star from one side and an OB runaway star from the other. This scenario can explain well the fact that most of the normal pulsars are
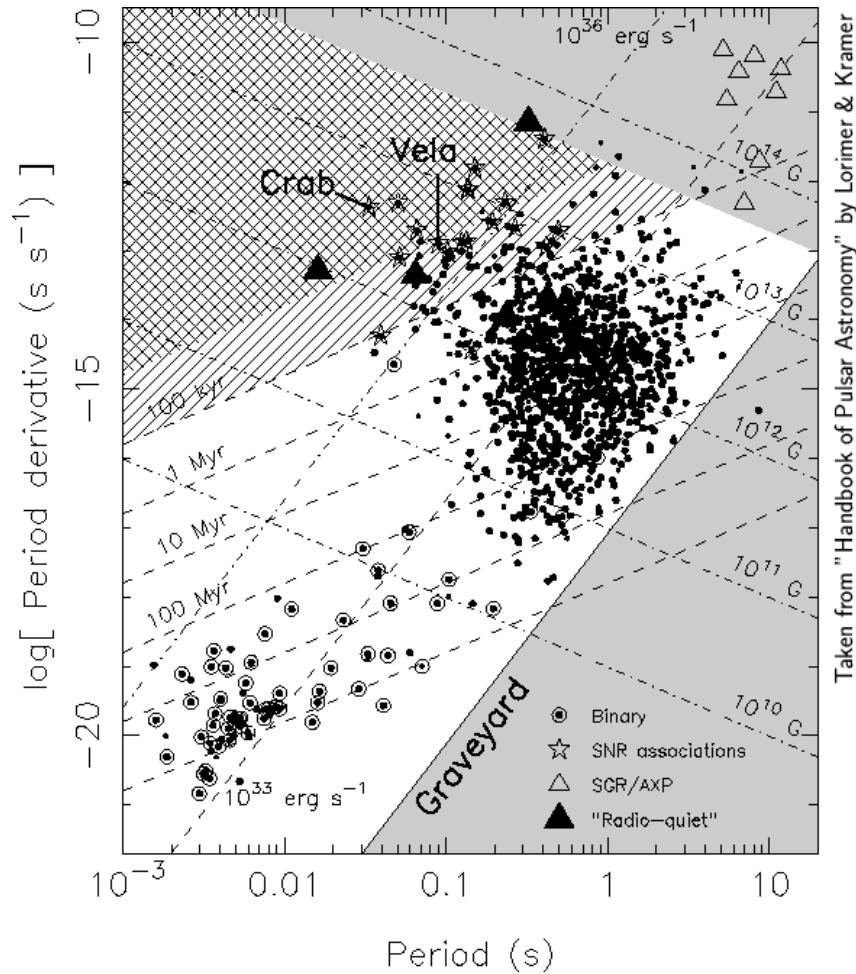
Figure 1.5: The $P - \dot{P}$ diagram for all the different categories of neutron stars where lines of constant characteristic age, magnetic field and spin-down luminosity are shown (Lorimer & Kramer 2005). Pulsars in binary systems are highlighted by a circle. Pulsars associated with supernova remnants are shown by stars.

isolated, although there are few identified cases of binary systems with a normal pulsar and a main sequence companion.

In the latter cases the secondary star is evolving into a red giant filling its Roche lobe and matter accretion on the old neutron star begins. During the accretion the loss of orbital angular momentum (orbital shrinkage) of the system is converted into an angular momentum gain for the pulsar which spins-up (a small part is also lost into space). During this long timescale process the pulsar is becoming a millisecond pulsar and tidal forces circularise the orbit. The envelope of the companion is exhausted and it usually stabilises to a low-mass helium white dwarf (HWD). In the phase of the accretion, X-rays are being produced by the release of gravitational energy of the in-falling matter to the pulsar and we expect to observe the system as a low-mass X-ray binary (LMXB). Although, LMXBs have been detected in X-rays no radio pulsations have been observed from them. This is possibly because of absorption of the radio emission by the thick accretion disk or reduction of the accelerating potential in the magnetosphere of the
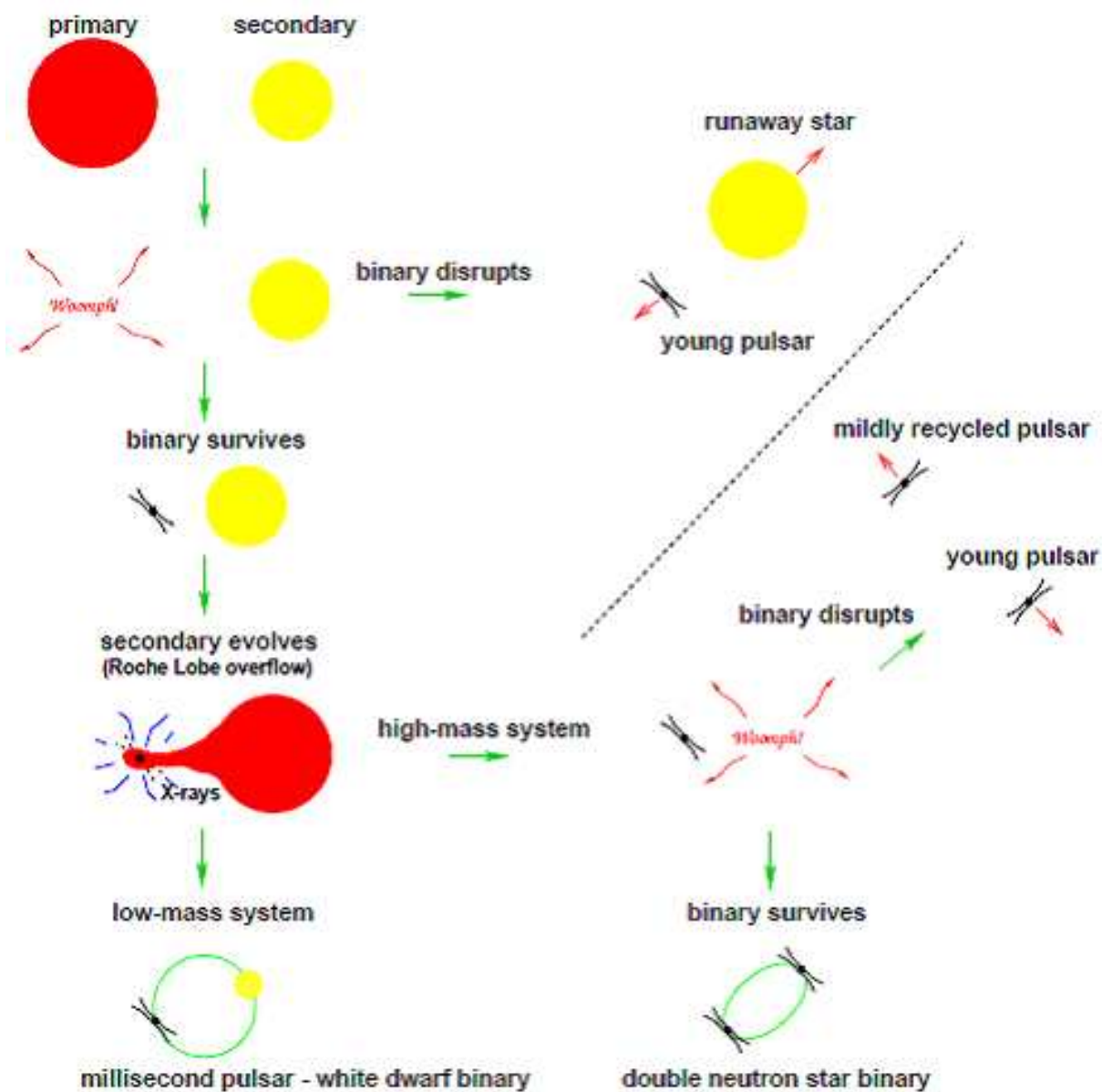
Figure 1.6: **Sketch of evolutionary scenarios of neutron stars and millisecond pulsars (Lorimer 2005).**

neutron star by in-falling matter. After mass transfer ends, the pulsar starts to emit in radio and the white dwarf is cooling down, thus efforts are being made to connect and compare the cooling age of the WD with the spin-down age of the millisecond pulsar in a binary system. Recently, Archibald et al. (2009) observed the "missing link" of radio pulsating millisecond pulsars and LMXBs confirming the aforementioned theories. This is the radio source FIRST J102347.67+003841.2 which was detected for the first time as an 1.69 ms radio pulsar in orbit with a low mass companion. Previous optical observations indicate that an accretion disk was present in this system within the last decade proving the transition from the LMXB phase to the "active" millisecond pulsar.

Apart from the previous evolutionary track there is the case that the secondary star is also a

high mass star ($M>8\,M_\odot$). The first steps are the same, but instead of a LMXB we now have a high-mass X-ray binary. The accretion phase is not as long as before and the secondary might also explode as a supernova leaving behind a second neutron star. If the system is separated from the explosion the result will be an isolated normal young pulsar and an isolated "slow" millisecond pulsar. This might the explanation for the 15 isolated millisecond pulsars already observed on contradiction with the less realistic theory where the companion is being ablated. Finally, if the system survives the supernova explosion the result is a binary neutron star system. Around 8 of this systems are known where only one of the two neutron stars is being observed as a radio pulsar. The first direct confirmation of this theory was given with the discovery of the, so far, only double pulsar J0737$-$3039. A 22.7 ms pulsar (A) orbiting a 2.77 s normal pulsar (B) every 2.4 hrs is representing clearly the high-mass evolutionary scenario, described before, where A is the first neutron star formed and B the second one.

1.3   Magnetic fields of magnetars

So far 16 magnetars (6 SGRs and 10 AXPs) have been discovered. From birthrate calculations it is not clear yet if and how they are evolutionary connected with the rest of the neutron stars (Keane & Kramer 2008), although they have similar origins. One of the main subjects of many discussions is their extreme magnetic field and their extreme bursting emission.

Magnetars, as all neutron stars, are believed to be formed in the supernova explosion of a massive star. As far as we know they are isolated sources. The most possible origins of the large magnetic field strength of neutron stars is inheritance from the main sequence progenitor. However this is not sufficient for a magnetar. Only the addition of a dynamo action (Thompson & Duncan 1993) at some stage of evolution of the SN progenitor could create a seed field, amplification of which, during the core-collapse, could lead to an extremely strong surface magnetic field strength ($\sim 10^{15}$ G) (Spruit 2008). For the amplification Spruit (2008) suggests that differential rotation in the final stages of core collapse is the most possible scenario, since simply magnetic flux conservation is not enough. However, the conversion of differential rotation into magnetic energy has to be fairly efficient. We must also mention two basic requirements of this theory, stratification and helicity. The internal field is being brought to the surface by magnetic buoyancy, where the magnetic loops float upwards while the strong field reduces the gas pressure and density in it. The part of the loop outside the star forms a vacuum field with a dipole moment, but it has to reach the surface before stratification becomes stable and before the neutron star has formed completely (otherwise $B < 10^{17}$ G are being blocked). In addition, stratification is holding the field from escaping totally to the surface. Magnetic helicity $H = \int B \cdot A dV$, where A is a vector potential of B and the integral is over the magnetic field volume, is needed for the field to finally reach a stable magnetic equilibrium.

Thompson et al. (2000) also explain how magnetars emit radiation with the twisted magnetosphere model. Although they are born spinning very fast they spin down rapidly by emitting magnetic waves carrying off its rotational energy. This process is very efficient when the field is strong. Because of this it has been suggested that almost all magnetars are radio quiet since to a radio beam, rapid rotation is needed. Thus, most of the time the radio beams of magnetars are very narrow or turned-off, something that makes them difficult to observe. While the magnetic field of normal pulsars is almost constant, in magnetars, the magnetic field evolves over time, seeking a lower energy state. During this process, it subjects the crust to strong magnetic forces. Specifically, magnetic field lines continually drift through the star's liquid interior, stressing the

crust from below. The field is driving significant twisting motion of patches of crust along horizontal directions and whenever this happens, magnetic field lines outside the star also get twisted because they are connected to the crust. This process and its consequences are shown in Figure 1.7[1].
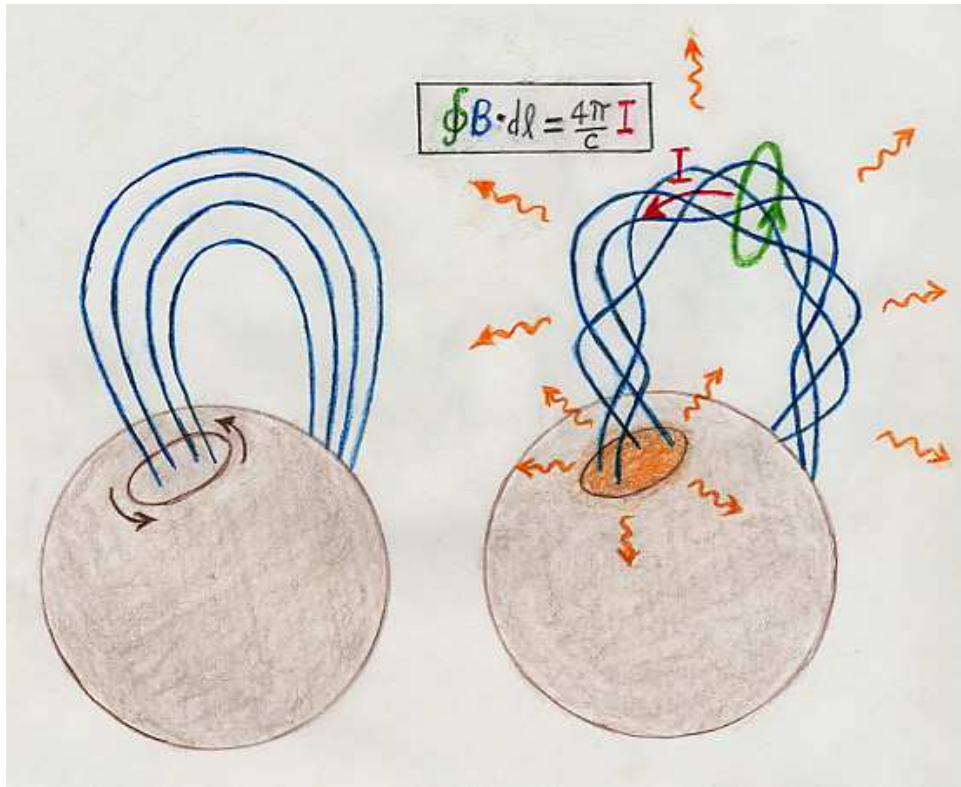
Figure 1.7: **Twisted magnetic filed lines and X-ray emission. (Left) Relaxed state. (Right) Crust deformations (sketch from R. Duncan).**

On the left the magnetar in its relaxed state is shown. Blue are the magnetic field lines crossing though the star. If there is a twist of the crust (brown arrows), caused by stresses from below, then immediately the field lines outside the magnetars will get twisted, as shown on the right. This twist, will lead to a current I along the magnetic field lines. The equation in the figure is Amperes law, together with the green loop magnetic field caused by the twist requires a current. Thus, we have electrons and protons, ions flowing opposite directions along the magnetic field lines and impact the magnetar's surface at the two opposite foot-points heating it and causing it to glow in soft X-rays. Especially electrons achieve very high velocities and they can often also collide with X-ray photons outside the star giving most of their kinetic energy and boosting them in high energies. This emission mechanism which is happening in bursts is believed to be what has been observed from both SGRs and AXPs.

---

[1]Taken from http://solomon.as.utexas.edu/ duncan/

1.4   Interstellar medium

The signal from a pulsar is affected in various ways while it propagates through the cold, ionised plasma of interstellar medium (ISM). The basic properties (as described in Lorimer & Kramer (2005) and references therein) of the effects of dispersion and interstellar scintillation in pulsar observations will be presented here.

1.4.1   Dispersion measure

The column density of the free electrons in the ISM along the line of sight is called dispersion measure (DM) and it is:

$$\mathrm{DM} = \int_0^d n_e dl (\mathrm{cm^{-3}pc}) \tag{1.5}$$

where d is the length from the pulsar to Earth and n_e is the electron number density ($\sim 0.03\mathrm{cm^{-3}}$). The interaction of the radio waves from a pulsar with the free electrons of the ISM lead to a frequency-dependent group velocity, so that pulses at lower frequencies travel slower and arrive later. Hence, by a measurement of the time delay between pulses at two different frequencies one can determine the DM of each pulsar via

$$\Delta t \simeq 4.15 \times 10^6 \mathrm{ms} \times (f_1^{-2} - f_2^{-2}) \times \mathrm{DM} \tag{1.6}$$

where Δt is the time delay between frequencies f_1 and f_2 (in MHz) and 4.15 is the dispersion constant

$$D = \frac{e}{2\pi m_e c} = (4.148808 \pm 0.000003) \times 10^3 \mathrm{MHz^2 pc^{-1} cm^3 s}, \tag{1.7}$$

where e and m_e are the charge and mass of an electron respectively.

Knowledge of the DM can be also used to infer a distance estimation to the pulsar, by integrating Equation (1.6) after assuming a model for the Galactic electron density distribution n_e.

1.4.2   Interstellar scintillation

The electron density inhomogeneities in the ISM contribute to pulsar observations as interstellar scintillation. Depending also on the distance, scintillation can be divided into three categories. The weak and the strong, which is in addition divided in the diffractive and refractive scintillation. For simplicity, we use the thin-screen model for the inhomogeneities in the ISM, thus we consider the waves passing through a thin scattering screen mid-way between the observed and the pulsar and their phases are being scattered into an angular spectrum of width θ_d. Interference can occur only if the phases of the waves are different by less than 1 radian (the size of the circular region on the scattering screen centred around the source, $s_0 = 1/\kappa\theta_d$, field coherence scale) and waves of frequencies outside the so-called scintillation bandwidth will not contribute. At distance d, the final phase modulation is producing a pattern of intensity variation in frequency and time and that can be measured in a dynamic spectrum, a two dimensional image of pulse intensity as a function of time and frequency. A strong chunk of flux density on this spectrum is called scintle and from its size in frequency and time the scintillation bandwidth Δf and timescale Δt can be measured respectively.

Apart from Δf and Δt we need to measure two more quantities for describing interstellar scintillation. The modulation index

$$m = \sigma / < S >, \tag{1.8}$$

where σ is the standard deviation of the observed flux densities and $< S >$ is their mean. The scintillation strength, u, which can be used to define the transition between weak ($u < 1$) and strong scintillation ($u > 1$):

$$u = \frac{l_F}{s_0} = \sqrt{\frac{f}{\Delta f_{DISS}}} \propto f^{-1.7} d^{1.1}. \tag{1.9}$$

l_F is the radius of the first Fresnel zone (used in diffractive optics for interference patterns), s_0 the field coherence scale, f the observing frequency and Δf_{DISS} the scintillation bandwidth of strong (diffractive) scintillation. For $u = 1$ (after also calculating Δf_{DISS}, see below) we can estimate the transition frequency from weak to strong scintillation, f_c. In general for a pulsar at a distance of 1 kpc the f_c is a few GHz, thus most pulsars are being observed in the strong scintillation regime.

Weak scintillation

Weak scintillation produces small phase perturbations at the distance to the observer. If the pulsar moves with a relative speed V_{ISS} to the observer the scintle pattern is moving. For a fixed observer an intensity modulation appears with a timescale:

$$\Delta t_{weak} = \frac{l_F}{V_{ISS}} \tag{1.10}$$

and a modulation index:

$$m_{weak} = \sqrt{u^{5/3}} = \left(\frac{f}{\Delta f_{DISS}}\right)^{5/12} \propto f^{-1.4} d^{0.9}. \tag{1.11}$$

The scintillation bandwidth is $\sim f$ and therefore very large.

Diffractive scintillation

Diffractive interstellar scintillation (DISS) produces large phase perturbations at the distance to the observer, therefore strong intensity variations. These variations are both in timescale

$$\Delta t_{DISS} = \frac{s_0}{V_{ISS}} \propto f^{1.2} d^{-0.6} \tag{1.12}$$

and frequency

$$\Delta f_{DISS} = \frac{1.16}{2\pi\tau_s} \simeq 185\,\text{Hz} \left(\frac{\tau_s}{\text{ms}}\right)^{-1}, \tag{1.13}$$

where τ_s is the scattering time being (from an empirical relationship)

$$\log \tau_s = -6.46 + 0.154 \log(DM) + 1.07(\log DM)^2 - 3.86 \log f. \tag{1.14}$$

Because of the large modulations in intensity the flux density of the pulsar may differ from its intrinsic flux density. Thus, long averaging is needed either in time or frequency in order to sample more than one scintles and obtain reliable flux measurements.

Refractive scintillation

The second category of strong scintillation is the refractive one and it is responsible for long and weak intensity modulations, increasing with distance to the pulsar. Theoretically, we can consider the effect of refractive scintillation as the focusing and defocusing of rays from the scattering screen. Its long timescale is

$$\Delta t_{RISS} = \frac{l_R}{V_{ISS}} = \frac{l_F^2}{s_0 V_{ISS}} = \frac{l_F^2}{s_0^2} \frac{s_0}{V_{ISS}} = u^2 \Delta t_{DISS} = \frac{f}{\Delta f_{DISS}} \Delta t_{DISS} \propto f^{-2.2} d^{1.6}. \quad (1.15)$$

It is clear that Δt_{RISS} is increasing with distance in contrast to Δt_{DISS}. The modulation index for refractive scintillation is

$$m_{RISS} = u^{-1/3} = \left(\frac{l_F}{s_0}\right)^{-1/3} = \left(\frac{\Delta f_{DISS}}{f}\right)^{1/6} \propto f^{0.57} d^{-0.37}. \quad (1.16)$$

Because of the long timescale of refractive scintillation it is not always possible to avoid its effects by time averaging, as in the case of the diffractive one.

1.5   Keplerian orbit & post Keplerian parameters

For the description of the orbit of a binary system Kepler's laws are being used. The six Keplerian parameters needed to describe a system are the orbital period P_b, the projected semi-major axis $\alpha = \alpha' \sin i$ (or $x = \alpha' \sin i/c$), the orbital eccentricity e, the longitude of the periastron ω, the epoch of the periastron passage T_0 (time when pulsar passes the periastron) and the position angle of the ascending node Ω_{asc} (Lorimer & Kramer 2005). For pulsar timing only the first five are needed. In Figure 1.8 (Freire et al. 2001) most of those parameters are shown schematically. Specifically, the orbit of a pulsar (P) around the centre of mass of the binary system (O)
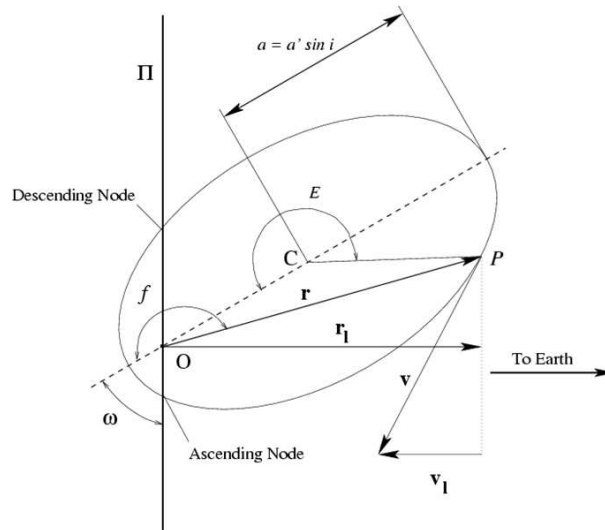
Figure 1.8: **Keplerian description of a binary orbit (Freire et al. 2001).**

projected onto the plane that contains the direction towards Earth (i.e perpendicular to the plane of the sky, Π) and the line of nodes where the orbital plane intersects Π is shown. On this figure

we clearly see an elliptical orbit of eccentricity e and projected semi-major axis $\alpha = \alpha' \sin i$, where i is the inclination angle of the orbital plane relatively to the plane of the sky. In addition, the longitude of the periastron ω and f which is the "true anomaly" (the angle of the pulsar to the periastron measured at O), are shown. Finally, also present are the vector r, connecting O to the pulsar's projected position and r_l which is the projection to the line-of-sight of the distance of the pulsar to O.

The aforementioned Keplerian parameters are enough to describe orbits when no relativistic effects are taken into account. However, relativistic or even classical effects, which cannot be ignored in some pulsar binary systems, can cause secular changes of the Keplerian parameters. In order to describe and measure these effects the "Post Keplerian" (PK) description has been used and the following "PK parameters" are introduced. The change of the longitude of periastron and orbital period, $\dot{\omega}$ and $\dot{P}_b$, respectively, the amplitude γ of the Einstein delay (caused by the varying effects of the gravitational redshift due to the presence of the companion and time dilation as the pulsar moves on its orbit at varying speed and distances from the companion) and the range, r and shape s of the Shapiro delay (caused by the gravitational field of the companion) (Lorimer & Kramer 2005).

Measurements of PK parameters are vital for tests of GR and alternative theories of gravity. We know that for point masses with negligible spin contributions, the PK parameters should be only functions of the Keplerian parameters and the masses of the two bodies of the binary system. Thus, with the masses as free parameters, an observation of two PK parameters can determine the masses for a given theory. In addition, measurements of three PK parameters provide a consistency check for this theory. The best example is the case of the double pulsar PSR J0737$-$3039 (Kramer et al. 2006) where 5 PK parameters and the mass ratio were measured providing 4 independent tests of General Relativity. In Figure 1.9 these GR tests together with the latest measurement of the spin precession rate of pulsar B, Ω_{SO}, are shown on a "mass-mass" diagram (Kramer private communication). All the lines intersect in a single point, a pair of mass values, which means that GR manages to pass the best strong-field regime test.

1.6   The European Pulsar Timing Array (EPTA)

The European Pulsar Timing Array (EPTA) network (Figure 1.10) is a collaboration between the five institutes (ASTRON, JBO, INAF, MPIfR and Nançay observatory) operating the largest radio telescopes in Europe. It is consisting of the Effelsberg 100m radiotelescope of the Max-Planck-Institute for Radioastronomy (MPIfR) in Germany, the 76m Lovell radiotelescope of the Manchester University, at Jodrell Bank, UK, the 94m equivalent Westerbork Synthesis Radio Telescope (WSRT) of ASTRON in the Netherlands, the 94m equivalent Nançay decimetric radio telescope (NRT) in France and soon the 64m Sardinia Radio Telescope (SRT) in Italy.

The EPTA is using the available telescopes for high-precision timing in a coordinated way, in schedules and source lists. This results, in larger and denser datasets in multiple frequencies. In addition, exchange of data, people and knowledge between the working groups is ordinarily happening, resolving swiftly any systematic telescope problems or other issues. The main aim of the EPTA is to increase the precision and quality of pulsar timing measurements, to study the astrophysics of millisecond pulsars and to detect cosmological gravitational waves in the nano-Hertz regime.
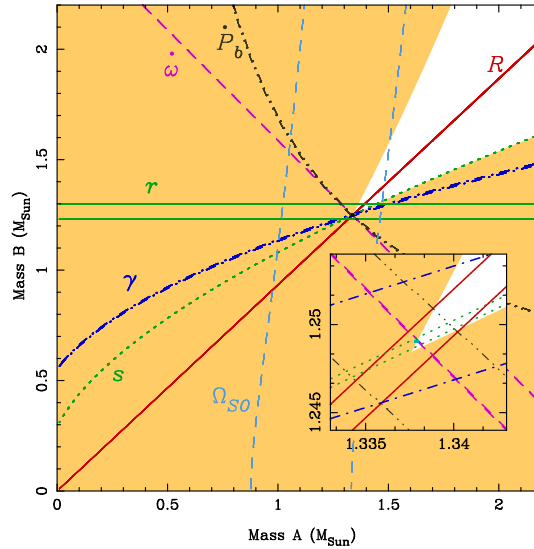
Figure 1.9: Mass-mass diagram of PSR J0737−3039 where all the GR tests are represented by the different lines. The shaded region is forbidden because $i \leq 1$. With R the mass ratio derived from the measured semi-major axes of the A and B orbits is shown. In addition, the spin precession rate of pulsar B, Ω_{SO} yields a new constraint on the mass-mass diagram. In the zoom in box it is clear that the intersection of all line pairs is consistent with a single point that corresponds to the masses of A and B (Kramer private communication).

Figure 1.10: The European Pulsar Timing Array.

1.6.1 Gravitational wave detection

One of the main predictions of Einstein's general theory of relativity is the existence of gravitational waves. Gravitational waves are ripples in the curvature of spacetime generated from the accelerated masses in it, propagating as waves. Generally, gravitational waves are radiated over a wide range of frequencies by accelerated objects, provided that the motion is not perfectly symmetric. Although, strong indirect evidence of their existence has been obtained by binary pulsar experiments (i.e. PSR B1913+16 and PSR J0737−3039), a direct detection has not been yet achieved.

One approach of detecting gravitational waves are the ground based interferometers such us the current GEO600 (Danzmann & et al. 1995), VIRGO (Caron & et al. 1998), LIGO (Abramovici et al. 1992) and the future Advanced LIGO (Barish 2000) and space mission LISA Danzmann (2000). These are gravitational wave detectors sensitive to the high frequency regime of the gravitational wave spectrum (i.e. Advanced LIGO $\sim$100 Hz, LISA $\sim$mHz), as presented on the left part of Figure 1.11 (i.e. coalescing stellar-mass binaries).

An alternative, but complementary to the previous, technique to observe gravitational waves is with a pulsar timing array (PTA). Let us assume that the solar system barycentre and a distant pulsar are opposite ends of an imaginary arm in space. Then the pulsar can be used as a reference clock sending regular signals observed on Earth over a timescale T. If a gravitational wave passes, it will perturb the local spacetime metric and the observed effect will be a change in the apparent rotational period of the pulsar. If the uncertainty of the pulse times of arrivals is σ the detector will be sensitive to waves with dimensionless amplitudes of $A \geq \sigma/T$ and frequencies $f \sim 1/T$ (Bertotti et al. 1983; Blandford et al. 1984), thus in the nano-Hertz regime (left part of Figure 1.11). If this arrangement is extended with the use of high precision timing data from more millisecond pulsars (more stable clocks) distributed across the sky, we have a PTA (right part of Figure 1.11). With a PTA we have the capability to cross-correlate the residuals for pairs of pulsars (Jenet et al. 2005; van Haasteren et al. 2009) in order to distinguish the noise in the timing data from the signature of the stochastic gravitational wave background. The latter, has been predicted to originate i.e. from coalescent super massive black holes in the early universe, from relic GWs form the big bang and from cosmological sources like cosmic strings, inflation and phase transitions (Kramer et al. (2004) and references therein). The GW strain spectrum, $h_c(f)$, can be described by a power-law in the GW frequency

$$h_c(f) = A \left(\frac{f}{yr^{-1}} \right)^{\alpha},$$ (1.17)

where the spectral exponent $\alpha = -2/3, -1$ and $-7/6$ for GW backgrounds, originates from coalescent super massive black holes, from relic GWs from the big bang and from cosmic strings respectively. The energy density of the background per unit logarithmic frequency interval is

$$\Omega_{GW}(f) = \frac{2}{3} \frac{\pi^2}{H_0^2} f^2 h_c(f)^2,$$ (1.18)

where H_0 is the Hubble constant (Hobbs (2008) and references therein).

EPTA, as mentioned before is one of the most important efforts in gravitational wave detection in this regime, using more than 10 years of timing data from 15-20 pulsars. The next step, the Large European Array for Pulsars (LEAP), which will be a phased array of the 5 EPTA telescopes increasing vastly the sensitivity, together with the Parkes pulsar timing array (PPTA) and nanoGrav (GBT and Arecibo) will be able to form a global pulsar timing array with full sky coverage wishing to lead the way in the detection and study of gravitational waves.

A major part of the current thesis is playing an important role in this EPTA effort (Chapter 4). New techniques are applied for calibration and improvement of the Effelsberg timing data which are combined with the datasets from the rest of the EPTA telescopes (Janssen PhD thesis, 2009; Purver PhD thesis, in prep.; Desvignes PhD thesis, in prep.; van Haasteren PhD thesis, in prep.) The current preliminary upper limit for the amplitude of a stochastic gravitational wave background signal of the EPTA is $A = 1.9 \times 10^{-14} yr^{1/2}$, using data only from the best six EPTA pulsars (van Haasteren et al. (2009); van Haasteren PhD thesis, in prep.). This compares
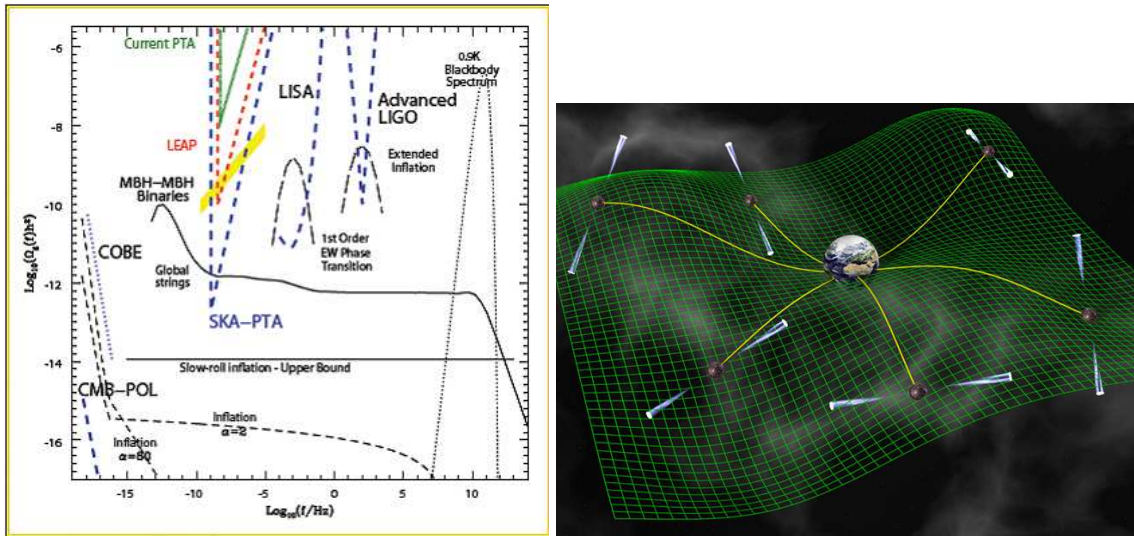
Figure 1.11: **(Left) Gravitational wave energy density spectrum with the frequency range of the current and future detectors and the sources of GW emission. The GW limit of PTA is in the nano-Hertz regime, complementary with the LISA and Advanced LIGO ones (Kramer et al. 2004) (Right) A pulsar timing array (D. Champion).**

to $A = 1.04 \times 10^{-14} yr^{1/2}$ by Jenet et al. (2006) who used Parkes data along with archival data from the Arecibo telescope. The current work is vital for increasing the timing accuracy and the number of extremely precise timed sources, improving the detection capabilities of the EPTA.

2. Multi-telescope Observations, Data Reduction and Techniques

The world is full of obvious things which nobody by any chance ever observes.

Sherlock Holmes (Sir Arthur Conan Doyle)

This chapter is divided into three major sections. 1) The section of observations. In this the different observing systems and calibration procedures of all the telescopes used for the current study are being described. 2) The section of data reduction. It is the most important part of this work, which is actually concentrated on the different techniques used for acquiring and improving the new and archival Effelsberg data. 3) The techniques and their advantages, used for combining the various different sets of multi-telescope and multi-frequency data.

2.1 Observations

The section is divided according to the two major observing modes that were used for the current work, single pulse mode and timing mode. The telescopes contributed in total are all EPTA ones. The 100m radio telescope of the Max-Planck-Institute for Radioastronomy (MPIfR), at Effelsberg, Germany, is the second largest fully steerable telescope. With an alt-azimuth mount, a primary focus of 100 m diameter , a secondary Gregorian focus of 6.5 m and receivers mounted in prime and secondary focus, it operates at frequencies between 0.4 and 96 GHz. The 76m Lovell radio telescope at Jodrell Bank observatory of the University of Manchester, UK, is the 3rd largest radio telescope in the world. With an alt-azimuth fully steerable mount the primary focus paraboloid antenna can reach up to 8 GHz. The Westerbork Synthesis Radio Telescope (WSRT) in the Netherlands with an effective area of $\sim 7000\,\mathrm{m}^2$ (94m equivalent), is a powerful aperture synthesis interferometer consisting of 14 antennas arranged on a 2.7 km East-West line. It can operate at frequencies between 120 MHz and 8.3 GHz. The 94m equivalent Nançay decimetric Radio Telescope (NRT), in France has a unique Kraus-type design with two mirrors at a 460 m distance between them. With a primary mirror consisting of 10 panels (20 m long and 40 m high) and a secondary shaped as a section of a sphere of 560 m radius it is observing mostly at frequencies between 1.4 to 4 GHz. A summary of all the telescopes instrumentation and the calibration procedures for each mode will be presented in sections 2.1.1 and 2.1.2, while a more

detailed description of the two major observation systems of the Effelsberg[1] radio telescope can be found in the Appendix. Some details of the receivers used during the observations are available in Table 2.1

Telescope	Mode	Frequency (MHz)	BW (MHz)
Effelsberg	Singe Pulse	2640	100
	Singe Pulse	4850	500
	Singe Pulse	8350	1000
	Singe Pulse	14600	1000
	Singe Pulse	32000	2000
	Timing	860	40
	Timing	1400	100
	Timing	2700	80
Lovell	Single Pulse	1420	32
	Timing	400	8
	Timing	600	8
	Timing	1400	64(32[1])
WSRT	Single Pulse	4896	160
	Timing	350	80[2]
	Timing	840	80
	Timing	1380	160
Nancay	Timing	1400	128

Table 2.1: **Details on the made single pulse and timing observations**

[1]: For polarisation measurements.

[2]: Usually two bands centered at 328 and 382 MHz are used with 10 MHz BW each.

2.1.1　Single pulse mode

Single pulse observations are of fundamental importance to neutron star studies itself. The explanation of the structure complexity and the various phenomena like nulling, mode changing and drifting can only be achieved by observing a sequence of single pulses. Single pulse mode is divided into two categories. The asynchronous mode, where search of new pulsars is performed offline by looking for periodic signals of unknown pulse period and dispersion measure (DM) in time series of de-dispersed candidate single pulses. The continuous stream of data is recorded having no Doppler corrected sample time. On the other hand, in the synchronous mode, the one used and described further in the current work, the observation is performed synchronously to the known apparent pulse period. In this work observations of slow bursting neutron stars (Chapter 5) were used in order to understand their long-term morphology, to measure the exact time they appear and to get the averaged profile and flux density. In each telescope the general methods of achieving the previously mentioned were more or less same but the technical characteristics and as a consequence the techniques used for each one differ.

---

[1]http://www.mpifr.de/div/effelsberg/receivers/receiver.html contains all the technical information about Effelsberg receivers

Effelsberg: For single pulse studies and eventually flux density measurements at Effelsberg (Lazaridis et al. 2008) we used the 2.64 GHz, 4.85 GHz, 8.35 GHz, 14.6 GHz and 32 GHz cooled HEMT receivers that are installed in the secondary focus (Karastergiou et al. 2001). Each system provides a total bandwidth of 100, 500, 1000, 1000 and 2000 MHz respectively. The wide-bandwidth circularly polarised intermediate frequency (IF) signals are fed into a multiplying polarimeter and detector in the focus cabin and are digitised by fast voltage-to-frequency (V/f) converters. All Stokes parameters are recorded with 1024 phase bins of few ms duration. A noise diode signal is injected into the wavefront following the horn synchronously with the pulse period in the first 50 bins of each measurement in order to calibrate the flux density of a pulsar reliably (Figure 2.1). A more detailed description of the whole Effelsberg Pulsar Observing System (EPOS) is given in the Appendix A.1. The power output of the diode is compared with the power that is received from the pulsar. The signal of the noise diode itself is frequently calibrated and monitored by observing known reference sources during regular pointing observations. The sources that were mostly used for calibration were 3C273, 3C274, 3C286 and NGC7027. They were observed at the beginning and the end of each session, in combination with checks on pointing and focus stability. The whole procedure of Effelsberg calibration is described further in section 2.2.1 and Angelakis (2007). The quality of our observations was also monitored by taking data for well known pulsars such as PSR B1929+10 (Figure 2.1) which is strong enough to be detected at all frequencies. The observed properties of this pulsar, extensively studied at Effelsberg, were compared to archival data to confirm that the system was functioning correctly at all frequencies. An important aspect is that from December 2006 the new sub-reflector of the telescope was used. It was installed in October 2006, improving the sensitivity and resulting in flatter gain curves but also allowing fast receiver changes, the importance of which will be fully understood in Chapter 5.

Lovell: At Jodrell Bank (Kramer et al. 2007) the 1.4 GHz receiving system was employed (Karastergiou et al. 2001) with a bandwidth of 32 MHz. After conversion to IF, two orthogonal circularly polarised signals were fed into a 32×1.0 MHz channel filter bank system, with incoherent de-dispersion performed in hardware producing all four Stokes parameters. Specifically for the case of AXP J1810-197 (Chapter 5), because of hardware constraints of the de-disperser it was impossible to record the complete period. The period was divided into 3 phase intervals separated by small gaps which were needed for the recording of the data. At the beginning of each observation, the pulse phase of the first sampled bin was chosen such that the gaps were located in off-pulse regions.

WSRT: At Westerbork (Kramer et al. 2007) we mostly used the 4.9 GHz receiving system with a bandwidth of 80 MHz distributed evenly in 10 MHz sections across a total band of 160 MHz. The two linear polarisations from all the 14 telescopes were added by taking account of the relative geometrical and instrumental phase delays between them. Phase differences between the two linear polarisations were corrected by making observations of a known polarised calibrator. The baseband data were passed to the PuMa pulsar backend which formed a digital filter bank for the four Stokes parameters (Voûte et al. 2002). De-dispersion and folding are carried out offline.

2.1.2 Timing mode

High precision timing is the regular monitoring of the rotation of a neutron star by tracking the times of arrival (TOAs) of the radio pulses. The general procedure of pulsar timing, shown in Figure 2.2, demands a radio telescope to observe the source, a hardware or software processing
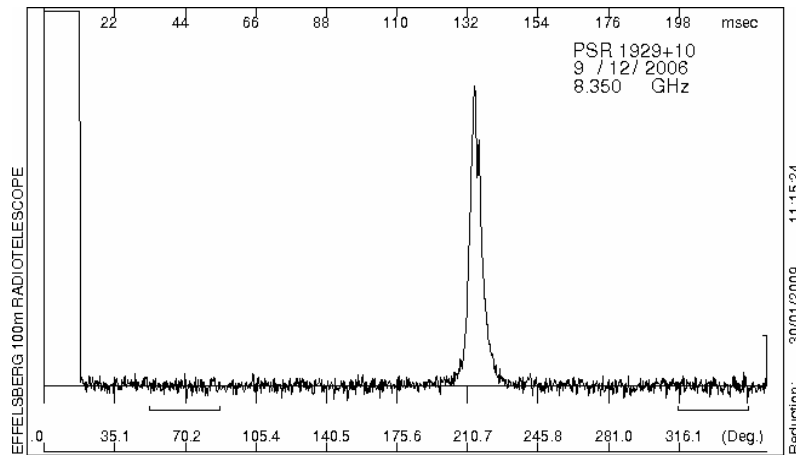
Figure 2.1: **Integrated pulse profile of PSR B1929+10 at 8.35 GHz. In the first 50 bins the calibration signal from the diode is inputed.**

of the signal in order to de-disperse it and a high signal-to-noise (S/N) (or synthetic) template profile (section 2.2) to compare the observed pulsar profiles with. All the radio telescopes follow the same general path but there are important differences in the hardware and the techniques used in different observatories.
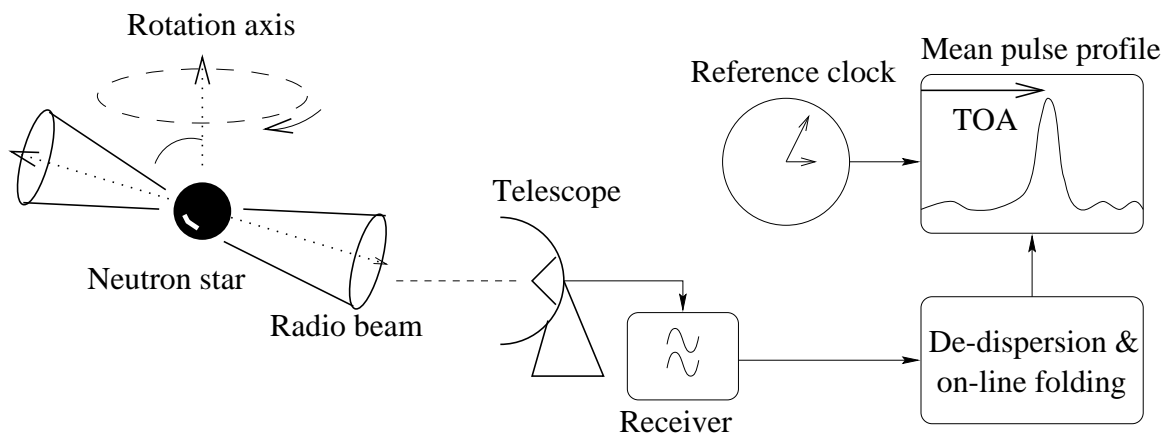
Figure 2.2: **General procedure of pulsar timing observations as provided by Lorimer & Kramer (2005) where the major steps are presented.**

Effelsberg: Timing observations in Effelsberg were made at irregular intervals at 860 MHz and once per month at 1.4 and 2.7 GHz. The first two used primary focus receivers, uncooled and cooled respectively, achieve typical system temperatures of 60 and 25 K. The 2.7 GHz is a cryogenically cooled HEMT receiver placed in the secondary focus. It has a typical system temperature at the zenith of 17 K. The bandwidths obtained with the three dual polarisation receivers are 40, 100 and 80 MHz respectively. For each polarisation the band was split into four sub-bands which themselves were subdivided into eight digitally sampled channels. Each of these 32 bands per polarisation was coherently de-dispersed by programmable digital filters

and then recombined with the appropriate channel dispersion delay (Backer et al. 1997) and synchronously summed up with the topocentric period. A detailed description of the Effelsberg-Berkeley Pulsar Processor (EBPP) is presented in the Appendix A.1.

A TOA was calculated for each average profile obtained from a single 5-15 min observation scan. In every session each pulsar was observed for three consequent scans resulting in three individual TOAs per source. In the data reduction process, the observed profile was cross correlated with a synthetic template, which was constructed out of a sufficiently large (3-7) number of Gaussian components fitted to a high S/N standard profile (Kramer et al. 1998, 1999a). Finally the TOA is obtained by adding the time delay between the profile and the start of the pulse phase window (phase bin 1) which is itself synchronised to a local H-maser clock. This clock is corrected offline to Coordinated Universal Time (UTC) using recorded maser offset information from Global Positioning System (GPS) satellites.

Lovell: At Jodrell Bank (e.g. Janssen et al. 2008) timing observations were made approximately every two weeks at centre frequencies around 410, 610 and 1400 MHz. They provide the longest time baseline TOAs obtained for this work. All receivers are cryogenically cooled, providing left-hand and right-hand circularly polarised signals. These signals are fed into an analogue filter bank system where the polarisations are detected, filtered, digitised at appropriate sampling intervals and incoherently de-dispersed in hardware. The sampling time is chosen every time for each pulsar to match the dispersion smearing across one filter bank channel. Both LHC and RHC signals are observed using a $2 \times 64 \times 0.1250$ MHz filter bank at 410 and 610 MHz, while most of the data acquired are recorded with a $2 \times 64 \times 1$ MHz system at 1400 MHz.

The resulting de-dispersed time-series are folded on-line with the topocentric pulsar period and finally written to disc. In the off-line reduction, the two polarisations are summed to form total intensity profiles. A standard pulse template is used at each frequency to determine the TOA. During this process, TOAs are referred to the local H-maser time standard and already corrected to UTC using information obtained via the GPS.

WSRT: At the Westerbork Synthesis Radio Telescope (e.g. Janssen et al. 2008) pulsar timing observations were made approximately every month with the Pulsar Machine (Puma) (Voûte et al. 2002) and since September 2006 PuMaII (Karuppusamy et al. 2008), at frequencies centred at 350, 840 and 1380 MHz. The typical system temperatures for the receivers were 120, 75 and 27 K respectively. The sampling time was from 51.2 to few hundreds of μs, and the bandwidth used was 8×10 MHz where each 10 MHz band was split into 64 channels. The 1380 MHz data taken after September 2006 (PuMaII) used 80 MHz of bandwidth spread in 8 steps of 10 MHz over a range of 160 MHz. The data are being de-dispersed and folded off-line, and then integrated over frequency and time over the whole duration to get a single profile for each observation. Each profile is cross-correlated with a template profile, obtained from the summation of high S/N profiles, to calculate a TOA for each observation. These are referred to local time stamps from a H-maser at the station. Finally the TOAs are converted to UTC using GPS maser offset values measured at the observatory.

Nançay: At Nançay radio telescope (e.g. Janssen et al. 2008) timing observations were made approximately every week with the Berkeley-Orleans-Nancay (BON) coherent dedispersor for typical integration times of 45 min. Coherent de-dispersion of a 64 MHz band centred on 1398 MHz is carried out on 16×4 MHz channels using a PC cluster. The typical system temperature is 35 K. A UTC(GPS) receiver is used in a permanent link to control the Nancay clock (Rubidium) and the international UTC time scale. Differences between UTC and UTC(GPS) are less than 10 ns at maximum, and therefore no laboratory clock corrections are

needed. One TOA is calculated from cross-correlation with a pulse template for each observation of $\sim 45\,\mathrm{min}$.

2.2 Data reduction & cleaning techniques

In this section the description of the data acquisition procedure of Effelsberg (the rest of the telescopes follow the same steps) will be outlined. In addition, all the techniques used for the correction and improvement of the Effelsberg timing data will be presented. A major part of the results in the following chapters is achieved by the thorough and extensive work discussed in here.

2.2.1 Effelsberg flux calibration

Here we present the detailed procedure of Effelsberg receiver calibration and average pulse flux density acquisition, as described by Kraus (2007) and Jessner (2007). The initial step is the conversion of the measured signal from V/f counts (raw power units detected from the receiver) into temperatures (i.e. system temperature T_{sys} and antenna temperature T_A). For this we must know the value of the noise diode in K. TOOLBOX[2] is a software that can make the conversion by multiplying the given value T_{cal} (variable with frequency) to the data to get temperatures instead of counts (eq. 2.1):

$$T_{A[K]} = T_{cal[K]} \cdot T_{obs[counts]}. \tag{2.1}$$

The second step is the opacity correction. The atmosphere is causing an attenuation of the observed signal by a factor of $e^{-\tau AM}$, where τ is the zenith opacity and $AM = 1/\sin{(ELV)}$ the "airmass" and the following correction is applied: $T_A^* = T_A \cdot e^{\tau AM}$. In order to derive the actual opacity at a given time we use: $T_{sys} = T_0 + T_{Atm}(1 - e^{-\tau \cdot AM}) \simeq T_0 + T_{Atm} \cdot \tau \cdot AM$. We know the system temperature for each observation and the air mass and we assume the atmospheric temperature to be equal the air temperature (on ground level). The opacity (strongly dependent on the weather) is finally:

$$\tau = -\frac{1}{AM} \cdot \ln(1 - \frac{T_{sys} - T_0}{T_{Atm}}) \tag{2.2}$$

The third step is the gain-elevation correction, caused by small scale deformations (because of the homology principle no large deformations happen) of the surface when the telescope is moving to higher or lower elevation than 32° (elevation for which the dish is adjusted by holography measurements). The correction factor that we apply during the data analysis is:

$$T_A^{**} = \frac{T_A^*}{G(ELV)} = \frac{T_A^*}{A_0 + A_1 \cdot ELV + A_2 \cdot ELV^2}, \tag{2.3}$$

where G is the standard gain of the receiving system normalised to one, ELV the elevation of the antenna for the observation and A_0, A_1, A_2 are the gain coefficients for the elevation correction. In order to also get flux densities in Jy from antenna temperature we calculate the sensitivity of the telescope Γ which is:

$$\Gamma = \frac{\pi}{8\kappa}\eta_A D^2 = 2.844 \cdot 10^{-4}\eta_A D_{[m]}^2 \stackrel{(Effelsberg)}{=} \eta_A \cdot 2.844\,\mathrm{K/Jy}, \tag{2.4}$$

---

[2]Software package created and developed in Effelsberg

where D is the diameter of the antenna and η_A is the aperture efficiency. Since we don't know η_A a priori we finally determine Γ by observing known calibration sources. Hence, we finally get the flux density in Jansky: $S_{[Jy]} = \frac{T^{**}_{A[K]}}{\Gamma_{[K/Jy]}}$.

Specifically for pulsar observations, starting from the antenna temperature for a given calibration source of strength S_{cat} we use equation (2.5) (from equations (2.2) and (2.3)):

$$T_A = S_{cat}(\nu) \cdot e^{\frac{-\tau}{\sin{(ELV)}}} \cdot G_{rx} \cdot (A_0 + A_1 \cdot ELV + A_2 \cdot ELV^2), \tag{2.5}$$

where G_{rx} is the standard gain of the receiving system in K/Jy. Now (from equation (2.1) and (2.5)) we determine the actual value of T_{cal} from the pointing scan on a calibration source and the pointing results (T_{source}) obtained with TOOLBOX:

$$T_{cal} = \frac{S_{cat}(\nu) \cdot e^{\frac{-\tau}{\sin{(ELV)}}} \cdot G_{rx} \cdot (A_0 + A_1 \cdot ELV + A_2 \cdot ELV^2)}{T_{source} \cdot A_{tt_{cal}}}. \tag{2.6}$$

Since this is a receiver dependent quantity it should be constant during every session. $A_{tt_{cal}}$ is an additional attenuation for the calibration in the pulsar observations, used only for the 4.85 GHz receiver where the calibration is 10dB weaker than for the continuum pointing.

In the case of EPOS data, which are V/f encoded intensity data, we find the frequency increment (f_{cal}, strength of the calibration signal), in order to calibrate them. Thus, we initially specify two intervals at the beginning and the end of the pulse window for baseline calculations and one window covering the calibration signal. Then from C (the mean of the data in calibration) and $B_{1,2}$ (the means of the data in the baseline regions) we calculate f_{cal} and system temperature as follows:

$$f_{cal} = \frac{C - \frac{B_1+B_2}{2}}{t_{bin} \cdot N_{int}} \tag{2.7}$$

and

$$T_{sys} = T_{cal} \frac{\frac{B_1+B_2}{2}}{C - (B_1 + B_2)} \cdot \frac{e^{\frac{\tau}{\sin{(ELV)}}}}{A_0 + A_1 \cdot ELV + A_2 \cdot ELV^2} \tag{2.8}$$

Here the ELV is the actual elevation for the pulsar observation.

After determining the f_{cal} and calculating the opacity correction for the day we can obtain the flux density of the pulsar. Initially we subtract the baseline from each channel by fitting a straight line through the mean of the baseline intervals (not coinciding with the pulse or calibration signal). Then we divide the data (V/f counts) by duration of a phase bin, τ_{sample} times the number of integrations N_{int} as well as f_{cal} in order to get the signal in units of the calibration. By multiplying this with the ratio of T_{cal} with the gain factor G_{rx} we obtain the calibrated signal for each channel:

$$S(\phi) = T_{cal} \frac{D(\phi) - (a \cdot \phi + b)}{\tau_{sample} \cdot N_{int} \cdot f_{cal} \cdot G_{rx}} \tag{2.9}$$

where S(ϕ) is the flux density of one record as a function of pulse phase ϕ and D(ϕ) are the data at phase ϕ and a and b are the coefficients of the baseline fit. Finally we compute the flux density of the pulse found within the window (w1, w2) as the mean flux density of all pulses in that interval, corrected for the pulse duty cycle, elevation dependent telescope gain and sky opacity:

$$S_{mean,1} = \frac{\sum_{i=w1}^{w2} \sum_{j=1}^{N_{records}} S_j(\phi_i)}{(w2 - w1)N_{records}} \cdot \frac{\tau_{sample}(w2 - w1)}{P} \cdot \frac{e^{\frac{\tau}{\sin{(ELV)}}}}{A_0 + A_1 \cdot ELV + A_2 \cdot ELV^2} \tag{2.10}$$

We apply the elevation corrections only at the end of the processing. We follow the same procedure for both total power channels (polarisations) and we use the mean of the flux densities $S_{mean} = \frac{S_{mean,1} + S_{mean,2}}{2}$. We finally compute the error of the mean flux density from the standard deviations found for the sequence of fluxes in the individual records, representing the statistical properties of the pulses and their noise background.

2.2.2 Slow neutron stars

The software used for the whole procedure was mainly JHSPULS[3] but in many cases the MATLAB EPOS package[4] was used as well. The flux calibrated individual pulses can be used for direct single pulse analysis, for flux density measurements or for timing measurements. The first case will be discussed in Chapter 5. For the second case, the fluxes of the single pulses we get are from the two total power channels corresponding to left and right hand circular polarisation. Finally, the individual pulse flux densities and the two polarisations are averaged to provide the flux density and its associated error for each individual observation, as described in the previous section. Before averaging, all single pulse sequences are inspected for RFI (radio frequency interference, Figure 2.3) and the ones affected are being skipped. Whenever the average pulse profiles where in calibrated EPN[5] (European Pulsar Network) format, in which all the 4 Stokes parameters are given, the intensity was converted to flux density by equation (2.11) :

$$S_{mean} = S_{peak} \times \delta = S_{peak} \times \frac{W_{eq}}{P} = \sum_{i}^{N} S_{peak_i} \times \frac{W}{P} \qquad (2.11)$$

where S_{mean} is the mean flux density (the integrated intensity under the pulse averaged over the full period), S_{peak} is the peak flux density (the maximum intensity of the profile), δ is the duty cycle, P is the pulsar period, W_{eq} is the equivalent width, the width of a rectangular pulse having the same area as the true profile, W the pulse width and N the number of single pulses (Lorimer & Kramer 2005). This S_{mean} is equivalent with the one finally derived in the previous section.

Apart from when performing a complete timing analysis of a neutron star, there are other cases that we need to know the exact time of arrival (TOA) of the radio pulses. This can be necessary when we are dealing with a variable source (e.g. a magnetar as presented in Chapter 5) where phase alignment of all the observed scans has to be made in order to distinguish between the different components of the profile. Another reason may be that the TOAs of all the individual pulses of a slow neutron are needed. In both the cases the TOA acquirement procedure is exactly the same with the only difference that in the first we get the TOA of the integrated profile of each scan and in the latter the TOAs of all the single pulses of each scan. When we observe with the EPOS the sampling time depends on the period of the pulsar observed. A profile time resolution of P/1024 s, where P is the apparent period of the neutron star, is being used because of hardware constraints. In order to acquire the exact TOA of a single pulse or of the integrated profile of a scan we must find the exact bin of the fiducial point of the profile. In extreme cases that the profile varies this can be the initial peak. The profile or the sequence of single pulses (Figures 2.1 and 2.3 respectively) is constituted of 1024 phase bins. The reason of selecting the bin of the initial peak of the profile is used only in the cases that we

---

[3]Created and developed by W. Sieber, A. Sievers, A. Jessner, J.H. Seiradakis and M. Kramer
[4]Created and developed by A. Jessner and K. Lazaridis
[5]http://www.mpifr-bonn.mpg.de/div/pulsar/ data/browser.html
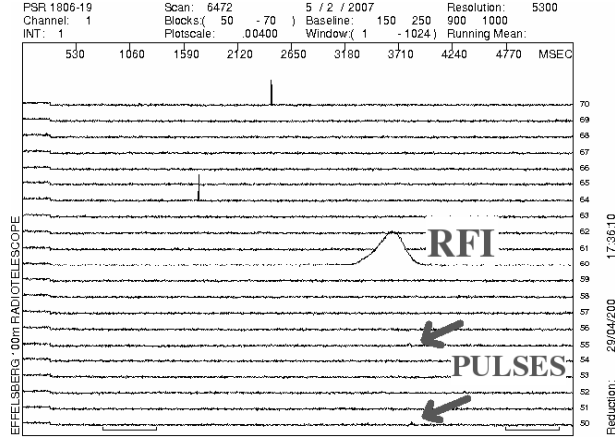
Figure 2.3: **A sequence of 20 pulses of AXP J1810-197 at 4.85 GHz where the extremely strong one is a bump of RFI, possibly from a satellite, in phase with the weak single pulses (pointed with arrows). In addition, two spikes of RFI appear that are however not in phase and too narrow to affect the measurement.**

do not have a template profile to cross-correlate with. After determining the bin position of the peak we multiply it with the time resolution and we add the resulting t_{bin}, to the synchronised time (T_{sync}), which is the reference epoch of the observation. In the case of single pulses one additional step is required because pulse profiles are variable. We use the number of the pulse periods in the sequence N and multiply it with the pulse period P and what we get, lets call it pulstart, we add it to t_{bin} before the summation with T_{sync}. The procedure is summarised in equation (2.12)

$$TOA = T_{sync} + (n_{bin} \times t_{sample} + N \times P)\sec \tag{2.12}$$

where TOA is in seconds, n_{bin} is the number of bin, t_{sample} the time resolution, N the number of pulse and P the period of the pulsar. The final step is to convert the time from seconds to Modified Julian Date (MJD), giving the topocentric TOA of the pulse or profile.

Something that we must finally keep in mind when observing with EPOS is the dispersion delay across a frequency channel (Chapter 1). It is calculated from $t_{DM} \simeq 4.15 \times 10^{-6}\,ms \times (f_{ref}^{-2} - f_{ch}^{-2}) \times DM$, where f_{ref} is a reference frequency in MHz, usually the centre frequency of the band and f_{ch} is a channel frequency relative to the reference one. In Table 2.2 the case of AXP J1810$-$197 (DM=178 cm^{-3}pc) is shown as an example, where it is clear that the interstellar dispersion was not affecting us at all at high frequencies and only very little at the lowest (where pulse broadening was detected), since we were using a time resolution of 5410 μs per phase bin.

The previously described analysis is a lot different from the timing of millisecond pulsars as will be presented in the next subsection.

2.2.3 Millisecond pulsars

In the first part of this subsection a summary of the millisecond pulsar timing process after the data acquisition will be given. A detailed description can be found in Lorimer & Kramer (2005). As mentioned in subsection 2.1.2, when a TOA is calculated for every integrated (from hundreds of single pulses) pulsar profile, the measured profile is cross correlated either with

Table 2.2: **The dispersive delay across the Effelsberg frequency channels.**

Centre Frequency (GHz)	BW (MHz)	t_{DM} (μs)
2.64	100	7387
4.85	500	5171
8.35	1000	1477
14.60	1000	443
32.00	2000	82.4

a high summed S/N profile or a synthetic template, in order to obtain the final TOA from the time offset of each profile. In other words, if the integrated profile is considered as the shifted version of the template, the TOA is obtained by the time shift of the profile from the fiducial point of the template (usually the highest peak or the midpoint of the profile) relative to the reference epoch of the observation (T_{sync} of the previous section). The cross correlation is done by a least- squares fitting of the Fourier-transformed data (Taylor 1992). In the template matching procedure an uncertainty occurs which depends on the noise of the template, when it is constructed by the summation of high S/N profiles. This effect can be avoided or at least reduced when a noise-free template is used, which in this case is the description of the profile as a sum of Gaussian components (Foster et al. 1991; Kramer et al. 1994). Another important reason is that after the creation of such a primary template the same can be used for different frequencies with small adjustments in the amplitudes and widths of its Gaussian components (Kramer et al. 1999a). An example of a template is shown in Figure 2.4 and cases were the use of a Gaussian noise free template improved the timing solution of the pulsar will be presented in Chapter 4.
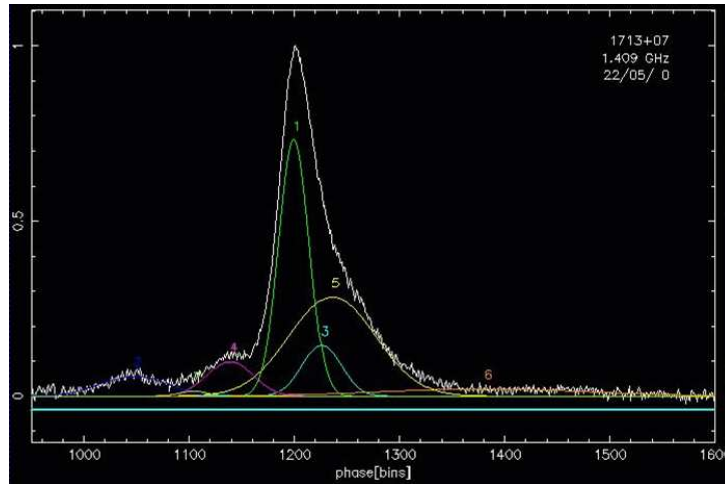
Figure 2.4: **The noise-free template of PSR J1713+0737 from Effelsberg data, consisting of six Gaussian components (provided by M. Purver).**

A vital step in the millisecond pulsar timing procedure is the time correction of the arrival times. The TOAs are determined from the local time at each observatory, which is usually

provided by hydrogen maser clocks. These times differ from those recorded against an ideal uniform clock because observatory clocks are compared and synchronised to UTC, using a GPS receiver, which gives a non-uniform timescale based on the rotation of the Earth. The ultimate aim of the clock correction process is to transform all site arrival times to a chosen realisation of TT (terrestrial time), which in an ideal realisation is a uniform SI (International System of units) clock. By default this is TT(TAI) (International Atomic Time), which differs from UTC by a constant offset plus an integral number of leap seconds due to the non-uniformity of Earths rotation. After applying these time corrections the TOA is topocentric in TT.

Some final corrections have to be applied to the latter TOA in order to convert it to the barycentric TOA. The first one is the Römer delay, which is the light travel time between the phase centre of the telescope and the SSB (Solar System Barycentre). To calculate it, accurate knowledge of the positions of all major masses in the Solar system is required. For that reason a solar system ephemeris is used and in the current work this is DE405 which is published by the Jet Propulsion Laboratory (JPL). For the Römer delay the absolute position of the observatory in the solar system must be known. It depends on the geodetic telescope coordinates, the orientation and non-uniform rotation of the Earth and its orbit. For this the appropriate corrections are used. They are published by IERS (international Earth Rotation Service). The second correction is the Shapiro delay, which corrects for extra delays due to curvature of the space time caused by the presence of masses in the solar system. The final correction that is applied when the pulse arrival times at the observatory are transformed to the arrival time at the SSB is the Einstein delay which describes the combined effect of time dilation and gravitational redshift due to the motion of the Earth and other bodies in the solar system respectively.

The TOAs are being corrected and analysed by TEMPO[6] or TEMPO2 (Hobbs et al. 2006) which are software packages for the analysis of pulsar timing data. The TOAs are being weighted by their individual uncertainties, which are a result of the least squares template fit. The timing model fit is done to determine a number of unknown parameters, such as astrometric, spin and binary parameters that make up a pulsar timing model. Starting with a small set of parameters tempo minimises the sum of weighted squared timing residuals, i.e. the difference between observed and modelled TOAs, yielding a set of improved pulsar parameters and their corresponding post-fit timing residuals as described in equation (2.13) (Lorimer & Kramer 2005)

$$\chi^2 = \sum_i \left(\frac{\Phi_{pred}(t_i) - \Phi_{obs_i}}{\sigma_i} \right)^2 . \tag{2.13}$$

$\Phi_{pred}(t_i)$ is the predicted number of non-integer rotations , Φ_{obs_i} the observed TOAs (phase zero), thus in the numerator are the residuals (phase differences between prediction and observation) and σ_i^2 is the variance (related to the measured TOA uncertainties). Data uncertainties used should yield a uniform reduced $\chi^2 = 1$ for each data set. If not, they are scaled by an appropriate factor to finally achieve it. For a "good" fit the variance of the observed distribution σ_i^2 should agree well with the variance s^2 estimated from the least squares template fit. But, the ratio of s^2/σ^2 can be estimated by the reduced chi square, χ^2/ν, where $\nu = N - p - 1$, N is the number of observations and p is the number of fitting parameters. Thus, for a good fit, where $s^2 \approx \sigma_i^2$ the reduced $\chi^2 = 1$. For a perfect pulsar model with no systematic effects the post-fit residuals show a Gaussian distribution with a mean value of zero and rms (root mean square) comparable to $\sum_i \sigma_i^2/N$. In Chapters 3 and 4 examples and further timing analysis will

---

[6]http://www.atnf.csiro.au/research/pulsar /tempo/

be presented.

Data calibration

As mentioned before here we describe the correction to the Effelsberg data. In particular all the following corrections and techniques were applied in 15 millisecond pulsars were 12 of them are in binary systems and 3 are solitary. All the sources are included to the list of the EPTA and all the corrections made contribute to the improvement of their timing solution. The achieved improvements and all the results from the further analysis will be presented in Chapters 3 and 4.

Jumps　　As it is mentioned in section 2.3.2, between different datasets produced from several telescopes there are constant time offsets deriving from the different templates used in each one. Specifically not only the templates are different (other are from high S/N profiles and other noise free from Gaussian components) but also the fiducial point chosen on the template may vary. Fortunately, tempo and tempo2 can fit for these time offsets or "jumps" between TOA datasets. In addition, due to the geometry of the cone containing the emitting region, the shape of the profile of a pulsar may appear differently at different frequencies (e.g. Thorsett (1991a); Xilouris et al. (1996)). In this case we use a separate template for each frequency and again it is possible that a "jump" has to be fitted for those TOAs. In the current work we had to deal with both cases. The strategy followed was to separate all the frequencies into separate data files, then multiply all the uncertainties by an appropriate factor in order to achieve a reduced $\chi^2 = 1$ for each dataset and finally fit for everything together with "jumps" between the datasets, when needed. This technique is followed for each telescope set of TOAs and at the end everything is fitted together. Those "jumps" between datasets are usually of the order of ms. This is not unexpected. The largest amount of the offset is caused by the different reference (fiducial) point in the template from each telescope. Since we are dealing with ms pulsars, phase offsets are expected to be of that order. Recently, Janssen et al. 2009 (in prep.) presented proof of the origin of those constant offsets. They showed, for the case of PSR J1012+5307, that the common choice of the fiducial point was reducing the offset to zero between Effelsberg and WSRT, even though the templates were generated from different datasets and using different techniques. This was also proving that no other large systematic effects were present.

Apart from the previously mentioned "jumps" one can discover "jumps" in the data of a single observing day, for a single session. This means that all the residuals of all the pulsars observed in that specific session do not fit properly with the rest. This is most of the times caused by an incorrect set up of the EBPP (in Effelsberg case) clock in the beginning of the observation. Tempo is capable of dealing with this problem by applying a "TIME" correction for the specific day the problem was encountered. Usually the time corrections are from 1-60 seconds. The most efficient way to find the exact time correction is a trial and error process. Run tempo multiple times for different time corrections and choose the one resulting in the lowest χ^2 value.

The final category of "jumps" that was found for the first time in Effelsberg data in the current work are the "microsecond jumps", which are of the order of tens or hundreds of μs. These also appear for a certain day for all the pulsars, but in some cases appear even for a whole month and are much smaller than the previous ones. Because of that they can be clearly noticed only when the timing solution for the pulsar is good enough (μs resolution). After discovering these "jumps", tempo can fit with the proper time correction in order to handle

the problem. Their size and duration, in some cases, excludes the possibility of arising from problems in the EBPP clock. The most possible explanation for the "microsecond jumps" is that they are due to a disfunction or time jump, or else glitch, of the telescopes hydrogen maser itself. In the search for the answer, as can be seen in Figure 2.5, the maser offset, from GPS, fluctuations were plotted over time. From this we managed to associate the largest of the visible jumps (MJD ~ 54350) with the longest period "microsecond jump" of our TOAs, of one month during September 2007. Also the second "microsecond jump" (MJD ~ 53890) was associated with a smaller maser glitch. However, the first one (MJD ~ 53750) could not be associated with any maser event. Further investigation is still in progress for the specific origin of these "microsecond jumps", but also for possible similar ones that are minor enough to detect at the current accuracy level. For the moment, we believe that apart from the three discussed epochs, other parts of the data set are not affected.
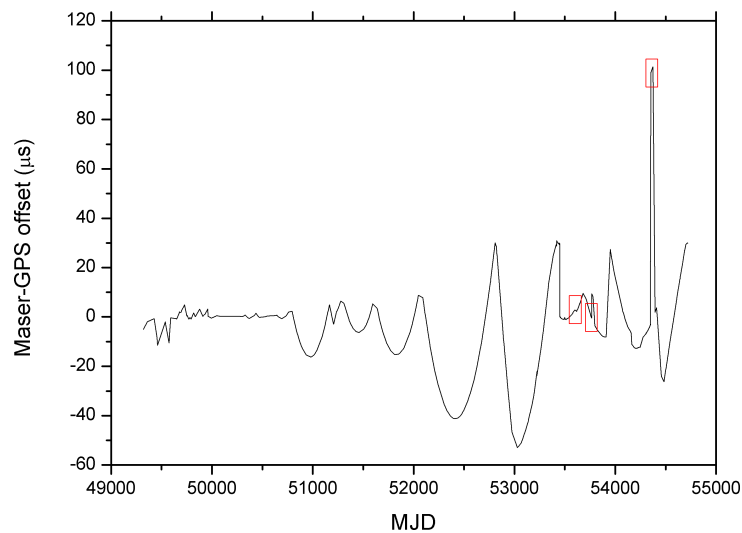
Figure 2.5: **Fluctuations of the maser-GPS time derivation versus time in MJD, for the whole period of Effelsberg timing. In red boxes the three detected μs "jumps". The last two are associated with a maser glitch.**

Fighting RFI   Radio Frequency Interference (RFI) was, is and will be a persistent problem to all kind of radio astronomical studies. RFI from satellites, radars, mobile transmitters and WLAN seems to increase as the technology on these fields develops, which makes the life of a radio astronomer more difficult and the data processing more demanding. In addition to all the external sources, rfi or noise can originate quite often from the telescope and its hardware as well, or from other sources on site. The latter sources of noise contributed quite a lot to the obtained profiles and as a result to the TOA errors in the Effelsberg timing data and some basic examples and ways of correcting for them (instead of throwing away "destroyed" TOAs) will be presented here.

As mentioned in section 2.1.2 the bandwidth for the two polarisation channels was split in 32 digitally sampled channels. In many cases, over the whole time-span of Effelsberg timing, one or more of these channels was unstable and introduced a noise signal that was disturbing

the pulse signal itself. The channels showing this noise were varying from time to time and from one frequency to the other. This kind of interference was not taken into consideration before, however, as it is shown in the example in Figures 2.6, 2.7 and 2.8 it is strong enough to totally disrupt the pulse signal and in continuation the TOA and finally the timing fit. In Figure 2.6 the 32 channels distributed over frequency of EBPP of an observation of PSR J1012+5307 at 2.7 GHz are shown for the two polarisations, with the de-dispersed summed signal of each polarisation channel at the bottom and an indicator of each channel noise on left and right (if the noise level is below five the channels are working perfectly). It is clear in that case that channel 30 of RHC is way above the noise limit of 5, which produces an extremely bad de-dispersed pulse signal where the actual pulse is not visible. In Figure 2.7 on the left side the actual profile of the TOA of the sum of the 2 channels after the cross-correlation with the template is shown, where again due to the initial channel noise the pulse is not visible. Finally, on the left side of Figure 2.8 the actual residual postfit zoomed around the specific day is shown, where the residuals are reaching, again due to the hardware noise, 2 ms. In addition this produces a much worse postfit rms than it should be, although in most of the cases this kind of TOA would be excluded since no pulse signal was visible.
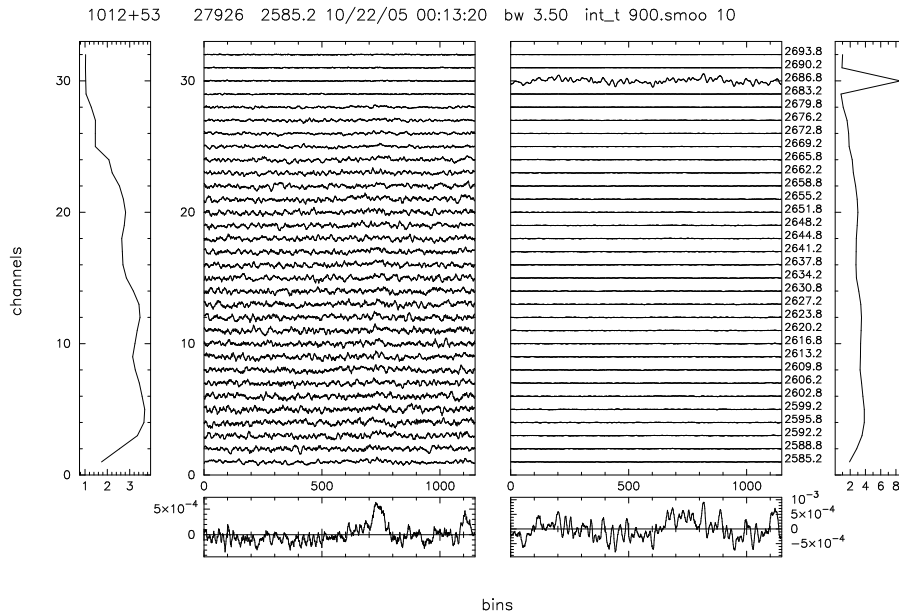
Figure 2.6: **The 32 channels for LHC and RHC polarisation of PSR J1012+5307 at 2.7 GHz. The noise at channel 30 is clearly disturbing the signal.**

Fifteen pulsars with more than 10 years of Effelsberg timing data were inspected and the channels which had a problem, for a specific day and a specific pulsar, where identified and removed. Finally the TOAs were recreated for all the cases. The lack of any periodicity in this noise signal made the work much more difficult since every single data file from these 15 pulsars was being checked visually. However, the vast improvement justified the efforts. An example of the results of this procedure is shown on the right side of Figures 2.7 and 2.8. The left and right part of these figures is exactly the same, with the only difference that channel 30 and its noise are removed in the right one. After the correction in the TOA profile the pulse signal is visible and clear and in addition the residuals in the postfit are below $50\,\mu s$. In conclusion, the
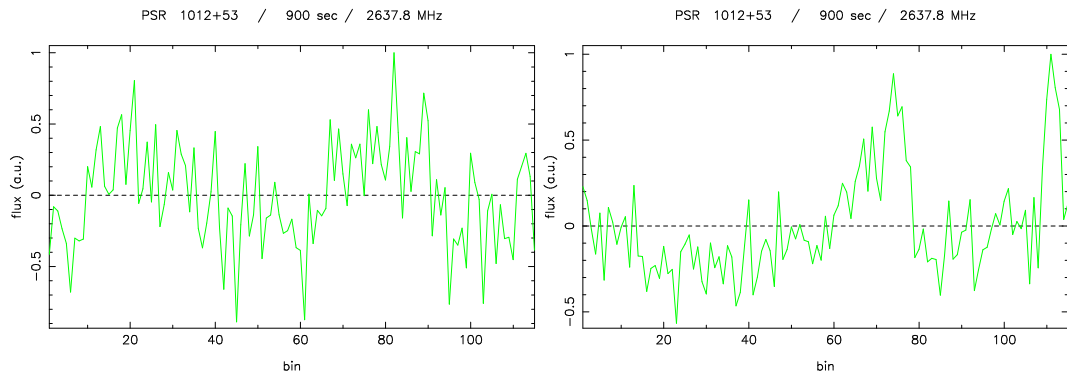
Figure 2.7: **The profile of the produced TOA. On the left with the noise, where the pulse signal is not visible. On the right without channel 30, where the pulse signal is visible and strong.**

importance of this work was not only that it improved the Effelsberg TOAs but also increased the usable number, as many cases were simply considered as "noisy" observations and were excluded.
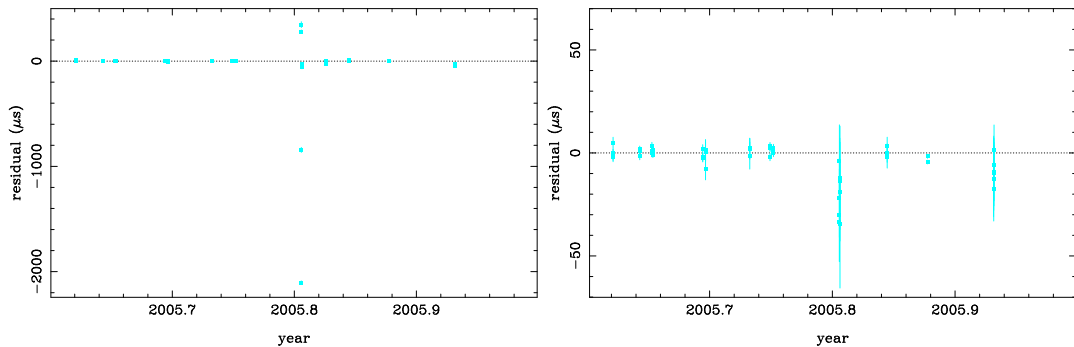
Figure 2.8: **Postfit of the residuals versus time of year. On the left, with the noise the residuals are very big. On the right, without channel 30 the residuals are fitting almost perfectly.**

Another source of interference that we had to deal with was from the telescope itself. As mentioned in section 2.1.1 in October 2006 the new sub-reflector was installed in the Effelsberg radio telescope providing a lot of advantages. Six months later, after noticing a spread in the residuals of some of our pulsars, we inspected the raw data and found an rfi signal that was only visible in the calibration scan that follows each pulsar observation (Figure 2.9). The source of that rfi was the new sub-reflector and more specifically the electronic system of its active panels that was producing a signal at 41.3 Hz. Fortunately the active system is not required for pulsar observations below 5 GHz and from October 2007 it was turned off. However, for six months we were getting the rfi seen in the right side of Figure 2.9. For most of the pulsars this was not a problem, since the rfi is below the noise level, but in one case it was affecting the TOAs and as a result the postfit rms. The best solution for handling this problem was to multiply the uncertainties of the residuals of the rfi period by a specific factor for which we achieve a reduced

$\chi^2 = 1$. Due to this they are weighted less in the fit. That way we did not have to remove any TOAs. Specifically, for PSR J1518+4904 the assumed errors had to be more than doubled for the sub-reflector period to avoid an increase of more than $1\,\mu$s in the postfit rms.
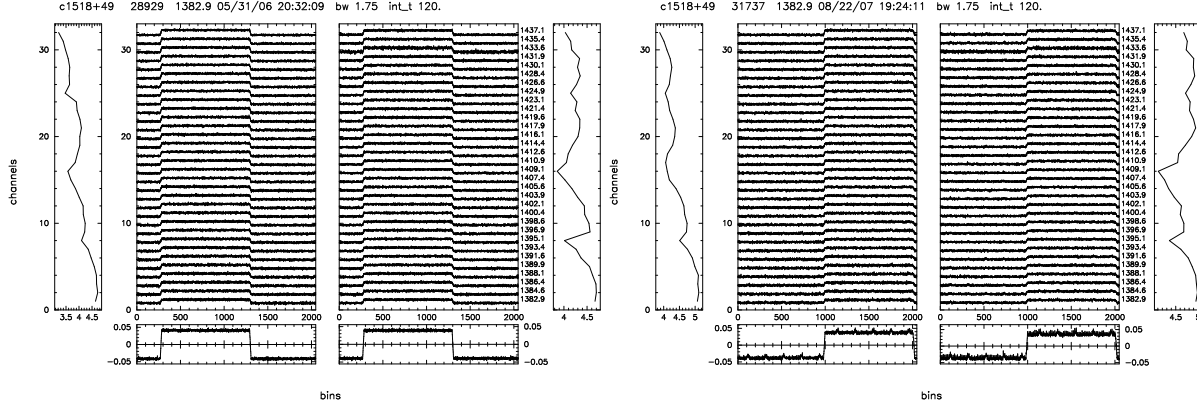
Figure 2.9: **The calibration signal following the pulsar timing observations of PSR J1518+4904. On the left side an observation with the old sub-reflector where everything looks fine. On the right side an observation with the new sub-reflector where periodic bumps of rfi appear at the bottom, at the sum signal.**

TOA alignment   The final part of the Effelsberg data improvement is what we call the TOA alignment. As mentioned already, in Effelsberg when performing timing observations, each pulsar is observed in 3 consequent scans for 10-15 min each plus the calibration scan at the end. The TOA uncertainties σ_{TOA} depend on specific parameters as shown in equation (2.14) (Lorimer & Kramer 2005) where the last part is derived from the radiometer equation of Dicke (1946):

$$\sigma_{TOA} \simeq \frac{W}{S/N} \propto \frac{S_{sys}}{\sqrt{t_{obs}\Delta f}} \times \frac{P\delta^{3/2}}{S_{mean}} \tag{2.14}$$

where S_{sys} is the system equivalent flux density, t_{obs} the integration time, Δf the observing bandwidth, P is the pulsar period, δ the duty cycle and S_{mean} the mean flux density of the pulsar. From that it is clear that short period pulsars, with narrow pulse widths, observed with large bandwidths over very long integration times will have the best timing solutions. Because of that, for a sum of single pulses $\sigma_{TOA} \propto \sqrt{1/N_{pulses}}$, we tried to phase sum (align) all the scans of each pulsar for every day, by cross correlating the profiles, in order to obtain 3 times more pulses integrated and improve the observed profile and hence, to decrease the TOA errorbars. Thus, all the separated integrated profiles of each day of all the 15 millisecond pulsars were first aligned and then a new TOA was produced from those. As we would expect this would decrease (improve) every days σ_{TOA} by $\sqrt{1/3}$ and is demonstrated in the example below for PSR J1744-1134. This is also an example of how TOAs are stored in a file for their use by tempo. In the first column an indicator for the telescope is shown, in the second the name of the pulsar, in the third the observing frequency, in the fourth the time of arrival, in the fifth the TOA uncertainty, in the sixth the date, in the seventh the file name and in the eighth the DM corrections:

Individual TOAs
g 1744-11 1408.250 51239.1914583706853 1.72 990302 c008605 .0
g 1744-11 1408.250 51239.1967362457687 1.35 990302 c008606 .0
g 1744-11 1408.250 51239.2021760498985 1.96 990302 c008607 .0

Aligned TOA
g 1744-11 1408.250 51239.1914583960410 0.92 990302 c000001 .0

In that case we had three scans of PSR J1744-1134 and we applied the technique of TOA alignment to get one single TOA for the day. It is clearly seen in the fifth column that the uncertainty has been decreased by a factor of $\sim \sqrt{1/3}$. In our source list there are some cases that did not show any improvement of the uncertainties from the application of this technique. This is possible when there are certain effects such as mode changing or profile variations involved in the analysed source. For millisecond pulsars it is not usually the case, however there are some observed cases (e.g. PSR J1022+1001, see section 4.6). In some other cases the problem exists only for the old data due to the ill-defined parameter files of the specific sources. All those problems introduce phase shifts of the profile during the observation session which produces deviations of the profile from the template but it might also create problems while we cross correlate the individual scans (during the alignment). After finishing the alignment of the TOAs for each observing session the total post-fit rms is calculated again. Normally, we would expect to get the same number as before the alignment, since the number of our TOAs is reduced to 1/3. However, the post-fit rms is improved in some of the cases because of non-detections that could be observed after the alignment. This effect is increasing the final number of TOAs and thus the accuracy, as will be shown in Chapters 3 and 4.

2.3 Combination of multi-telescope data

The driving force of the current work is the opportunity to use data from different telescopes. In that section the advantages of multi-telescope datasets will be explained (Janssen 2009). Advantages that extend to all the aspects of the scientific work carried out for pulsars. In addition, an initial summary of the techniques applied will be presented, while more details will be given throughout all the following chapters.

2.3.1 Multi-telescope advantages

Possibly the most important advantage of performing multi-telescope observations is the capability of doing simultaneous observations at more than one frequencies. In single pulse mode the need of simultaneity arises when the single pulse properties, like the sub-pulse drifting, of a source need to be studied and the single pulses from the several telescopes are to be correlated (Chapter 5). In addition, it is also important when the flux density and the spectrum of a transient highly variable source is being measured (Chapter 5). In the case of timing the advantage of having simultaneous observations at the same, in that case, frequency is that these observations can be used to check polarisation calibration and overall timing offsets between the telescopes.

Another important factor for having that kind of observations is the important way DM affects pulsar TOAs, which has been discussed already in Chapter 1. Its constant monitoring, by observing at different frequencies, is a vital point for a high precision pulsar timing array.

Especially in pulsar timing, the potential of multi-telescope observations adds to the total time spent on targets, increasing the total number of TOAs and leading to a gap-less coverage at all timescales. In the case of source monitoring it makes it possible to follow the source for a long continuous time and for the long period scheduling it results in an improved yearly orbital coverage.

The final advancement that can be accomplished from this kind of observations is the identification and in continuation correction of telescope based error in instrumentation or software. This can be achieved in a long-term program like timing (Chapters 3, 4) by the comparison of the different telescope datasets and the offsets between them.

2.3.2 Multi-telescope techniques

In single pulse observations the techniques for combining the acquired data from multiple-telescopes vary, due to the exact way one wants to use these data (single pulse or integrated pulse profile studies). In both cases the first steps are of course to obtain and calibrate them.

In the current work, when investigating the properties of the single pulses there are cases where a re-binning was applied to improve the S/N ratio of some observations and to match the time resolution in all the data sets. For pulse energy distributions, whenever there were multiple datasets per telescope per session, they were aligned in longitude and appended together to improve the statistics. Finally for single pulse correlation the data needed to get aligned to avoid interstellar dispersion effects. Some more details are presented in Chapter 5 and the full description of this analysis can be found in Serylak et al. (2009).

Another use of the current multi-telescope single pulse data was the measurements of the TOAs of slowly rotating neutron stars. The technique for doing that has been described in the previous section. The next step after creating each telescopes files containing the topocentric TOAs was to run tempo or tempo2 with all the datasets together to finally have a full coverage of the observed source.

In the case of the integrated pulse studies, currently used for flux density measurements and flux density spectrum analysis, the analysis is simpler. The integrated profile for each telescope per session is obtained, the flux density is measured and finally is used with the measurements from the other telescopes. In case there were more than one observed profile per session per telescope the flux densities and their errors were averaged and then used in the combined data.

In the high precision pulsar timing observations the combination of different data sets by different observatories is not very difficult but needs a careful approach. When combining data from telescopes with different observing and operating systems, it is important to account for all extra corrections needed, apart from the usual ones applied at each individual telescope, as described in the previous section. Observatory related time delays that are not accounted for (i.e. unmodeled cable delays) but also use of different templates, as shown in Figure 2.10, result in a time offset between sets of residuals from different telescopes.

Tempo and tempo2 can fit for these constant time offsets with the so-called jumps. The ideal case would be to use the same template for all the telescopes for each pulsar to get rid of some of those time offsets, work that is still in progress (Purver et al., in prep.). Last but not least, after combining all the datasets with their jumps, the final test is to obtain again the value of the reduced χ^2 which must be equal to one to be certain that no more systematic uncertainties are present.
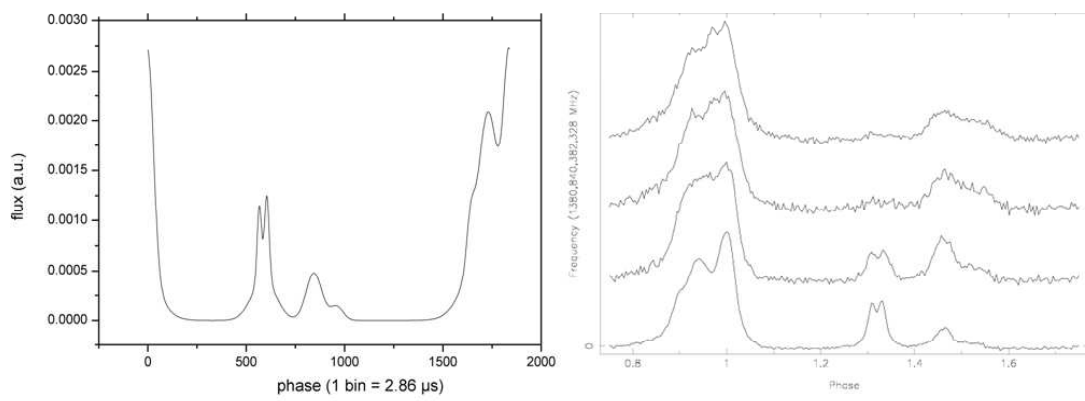
Figure 2.10: **Different templates between telescopes. On the left the PSR J1012+5307 synthetic Gaussian noise free template used for Effelsberg TOAs. On the right the high S/N templates for PSR J1012+5307 used in Westerbork for different frequencies.**

3. Millisecond Pulsar Timing I - PSR J1012+5307. Parallax, orbital orientation and GR tests.

The most merciful thing in the world, I think, is the inability of the human mind to correlate all its contents.

Howard Phillips Lovecraft

In the current chapter we present results from the high precision timing analysis of the pulsar-white dwarf binary PSR J1012+5307 using 15 years of multi-telescope data, which can also be found in Lazaridis et al. (2009). Observations were performed regularly by the European Pulsar Timing Array (EPTA) network, consisting of Effelsberg, Jodrell Bank, Westerbork and Nançay. All the timing parameters have been improved from the previously published values, at least by an order of magnitude. In addition, a parallax measurement of $\pi = 1.2(3)$ mas is obtained for the first time for PSR J1012+5307, being consistent with the optical estimation from the WD companion. Combining improved 3D velocity information and models for the Galactic potential the complete evolutionary Galactic path of the system is obtained. While a new intrinsic eccentricity upper limit of $e < 8.4 \times 10^{-7}$ is acquired, one of the smallest calculated for a binary system, a measurement of the variation of the projected semi-major axis also constrains the systems orbital orientation for the first time. It is shown that PSR J1012+5307 is an ideal laboratory for testing alternative theories of gravity. The measurement, for the first time, of the change of the orbital period of the system of $\dot{P}_b = 5(1) \times 10^{-14}$ is used to set an upper limit on the dipole gravitational wave emission that is valid for a wide class of alternative theories of gravity. Moreover, it is shown that in combination with other binary pulsar PSR J1012+5307 is an ideal system to provide self-consistent, generic limits, based only on millisecond pulsar data, for the dipole radiation and the variation of the gravitational constant.

3.1 Introduction

PSR J1012+5307 is a 5.3 ms pulsar in a binary system with orbital period of 14.5 h and a low mass companion (Nicastro et al. 1995). It was discovered during a survey for short period pulsars with the 76m Lovell radio telescope at Jodrell Bank. Lorimer et al. (1995a) reported

optical observations revealing an optical counterpart within 0.2 ± 0.5 arcsec of the pulsar timing position and being consistent with a helium white dwarf (WD) companion.

The optical observations of the WD companion offer a unique opportunity of information acquisition about the evolution of the binary system and the radio pulsar itself, such us the cooling age of the companion in comparison with the spin-down age of the pulsar (Lorimer et al. 1995a; Driebe et al. 1998; Ergma et al. 2001).

Using the NE2001 model for the Galactic distribution of free electrons (Cordes & Lazio 2002) and the pulsar's dispersion measure (DM) of $9\,\mathrm{cm}^{-3}$ pc (Nicastro et al. 1995) a distance of ~ 410 pc is derived. In contrast, Callanan et al. (1998) compared the measured optical luminosity of the WD to the value expected from WD models and calculated a distance of $d = 840 \pm 90$ pc. In addition they measured, by the Doppler shift of the measured H spectrum of the companion, a radial velocity component of $44 \pm 8\,\mathrm{km\,s}^{-1}$ relative to the SSB. From the radial velocity and the orbital parameters of the system the mass ratio of the pulsar and its companion was measured to be $q = m_p/m_c = 10.5 \pm 0.5$. Finally by fitting the spectrum of the WD to a grid of DA (hydrogen dominated) model atmospheres they derived a companion mass of $m_c = 0.16 \pm 0.02\,M_\odot$, a pulsar mass of $m_p = 1.64 \pm 0.22\,M_\odot$ and an orbital inclination angle of $i = 52° \pm 4°$.

Lange et al. (2001) presented the most complete precision timing analysis of PSR J1012+5307 using 4 years of timing data from the Effelsberg 100m radio telescope and 7 years from the 76m Lovell telescope. Using their low eccentricity binary model ELL1 and combining the timing measurements with the results from the optical observations they derived the full 3D velocity information for the system. Furthermore, after correcting for Doppler effects, they derived the intrinsic spin parameters of the pulsar and a characteristic age of 8.6 ± 1.9 Gyr which is consistent with the WD age from the optical estimates. In addition, after calculating upper limits for an extremely low orbital eccentricity they discussed evolutionary scenarios for the binary system but also presented tests and limits of alternative theories of gravitation. Finally, they discussed the prospects of future measurements of Post-Keplerian parameters (PK) which can contribute to the description of the orientation of the system and the calculation of stringent limits for the effective coupling strength of the scalar field to the pulsar.

In this chapter we revisit PSR J1012+5307 with seven more years of high-precision timing data and combined datasets from the European Pulsar Timing Array (EPTA) telescopes. After a short description of the timing procedure and the technique of combining our multi-telescope data, we present the updated measurements of the astrometric, spin and binary parameters for the system. Specifically we show the improvement in all the timing parameters and in the orbital eccentricity limit and in addition the value for the first time for PSR J1012+5307 of the timing parallax. Furthermore, we obtain a value for the orbital period variation, in agreement with the prediction of (Lange et al. 2001), from which we test different theories of gravitation and give one of the tightest bounds on a Parametrised Post-Newtonian (PPN) parameter. Finally, we present how the timing measurement of the change of the projected semi-major axis can complete the picture of the orientation of the binary system.

3.2 Observations

3.2.1 Effelsberg

PSR J1012+5307 was observed regularly with the Effelsberg 100m radio telescope since October 1996 with typical observing times of 5–15 min in three consecutive scans. Monthly ob-

servations were performed at 1400 MHz using the primary focus cooled HEMT receiver. It has a typical system temperature of 25 K and an antenna gain of $1.5\,\mathrm{KJy^{-1}}$. In order to monitor dispersion measure (DM) variations, it was also observed irregularly until August 2006 and monthly thereafter, at 2700 MHz. At these frequencies a cooled HEMT receiver located at the secondary focus was used which has a system temperature of 25 K. Finally, it was occasionally observed at 860 MHz using an uncooled HEMT receiver, located at the primary focus, with a typical system temperature of 60 K. The Effelsberg-Berkeley Pulsar Processor (EBPP) was used for coherent on-line de-dispersion of the signal from the LHC and RHC polarisations. It has 32 channels for both polarisations spread across bandwidths of 40, 100 and 80 MHz at 860, 1400 and 2700 MHz respectively (Backer et al. 1997). The output signals of each channel were fed into de-disperser boards for coherent on-line de-dispersion and were synchronously folded with the topocentric period.

Each TOA was obtained by cross-correlation of the profile with a synthetic template, which was constructed out of 12 Gaussian components fitted to a high signal-to-noise ratio standard profile (Kramer et al. 1998, 1999a). The TOAs were locally time stamped using a H-maser clock at the observatory. They were converted to UTC using the GPS maser offset values measured at the observatory, and the GPS to UTC corrections were made from the Bureau International des Poids et Measures (BIPM[1]).

3.2.2 Jodrell Bank

PSR J1012+5307 has been observed with the Lovell radio telescope 2–3 times per month since 1993, at three different frequencies. It is continuously observed at 1400 MHz and at 410 and 606 MHz, it was observed until 1997 and 1999, respectively. All the receivers are cryogenically cooled with system temperatures of 25, 50 and 35, respectively and their LHC and RHC polarisation signals are detected and incoherently de-dispersed in a $2\times32\times0.0312$ MHz filter bank at 410 MHz, in a $2\times6\times0.1250$ MHz filter-bank at 606 MHz and in a $2\times32\times1$ MHz filter-bank at 1400 MHz. The signals are synchronously folded at the topocentric pulsar period and finally copied to a disc.

Each TOA was obtained by cross-correlation of the profile with a standard template, generated by the summation of high S/N profiles. The TOAs were transferred to GPS from a H-maser and the time stamp was derived as for Effelsberg.

3.2.3 Westerbork

PSR J1012+5307 was observed monthly using the WSRT with the PuMa-I pulsar machine (Voûte et al. 2002). We used three observing frequencies: observations at centre frequencies of 1380 MHz and 350 MHz were carried out each month from August 1999, and the pulsar was observed occasionally at a centre frequency of 840 MHz from 2000 until 2002. The system temperatures were 27, 120 and 75 K, respectively and most observations were 30 minutes long. The WSRT observations used a bandwidth of 8×10 MHz for observations at 840 MHz and 1380 MHz, and after September 2006 the 8 bands were spread out over a total observing bandwidth of 160 MHz for the 1380 MHz observations. The observations at the low frequency setup used only two bands of 10 MHz, either centred at 328 and 382 MHz or 323 and 367 MHz. For the observations taken at 1380 or 840 MHz we used 64 frequency channels per 10 MHz

---

[1]http://www.bipm.org

band, and the observations at the low frequencies used 256 frequency channels per 10 MHz band.

For each observation, the data were de-dispersed and folded offline. Integration over frequency and time resulted in one single profile for each observation. Each profile was cross-correlated with a standard template, generated by the summation of high S/N profiles, so finally only one TOA was computed for each observation. The TOAs were transferred to GPS from a H-maser clock and the time stamp was derived as for Effelsberg.

3.2.4 Nançay

PSR J1012+5307 was observed roughly every 3 to 4 weeks with the Nançay Radio Telescope (NRT) since late 2004. The Nançay Radio Telescope is equivalent to a 94m dish, with a gain of $1.4 \, \mathrm{K} \, \mathrm{Jy}^{-1}$ and a minimal system temperature of 35 K at 1.4 GHz in the direction of the pulsar. With the BON (Berkeley-Orleans-Nançay) coherent dedispersor, in the period covered by the observations, a 64 MHz band centred on 1398 MHz is split into sixteen 4 MHz channels and coherently dedispersed using a PC-cluster, with typical integration times of one hour. The Nançay data are recorded on a UTC(GPS) time scale marked at the analogue to digital converter by a Thunderbolt receiver (Trimble Inc.). Differences between UTC and UTC(GPS) are less than 10 ns and therefore no laboratory clock corrections are needed. A single TOA was calculated from a cross-correlation with a pulse template for each observation of one hour.

3.2.5 Multi-telescope precision timing

Combing the EPTA multi-telescope datasets is not a trivial process. The general technique for achieving the optimal combination of the data sets is presented by Janssen et al. (2008). In general, using different datasets from different telescopes and obtained at different frequencies requires extra corrections, apart from the usual one of the transformation of all the individual telescope arrival times to arrival times in the TAI at the solar system barycentre (SSB). The extra corrections needed are usually constant time offsets between different datasets of residuals. These offsets derive from differences in the procedure of calculating the TOAs at each observatory, specifically differences in the templates. The timing software package TEMPO[2] can fit for these time offsets or "jumps". In the current work seven of these jumps needed to be fitted corresponding not only to the telescopes but also to the different frequencies used. Normally, three "jumps", one for each telescope, would be sufficient. However, the TOAs at different frequencies are usually calculated by different templates, which not always align optimally. In the current case, this occurs for Effelsberg and Westerbork TOAs. In Table 3.1 the properties of the individual datasets are presented.

The combination of the EPTA datasets has many advantages (Janssen et al. 2008). The need for continuous multi-frequency TOAs for precise measurement of the dispersion measure (DM) and monitoring of DM variations was met in full. The obtained upper limit for DM variations is $\dot{DM} < 2.6 \times 10^{-5} \, \mathrm{cm}^{-3} \mathrm{pc/yr}$. Most important the combination of the high quality data from Effelsberg, Nançay, WSRT with the long time span data of Jodrell (& Effelsberg) provides us with a 15 year dataset of TOAs without significant time gaps. Using all these EPTA datasets we improve and measure all the astrometric, spin and binary parameters of PSR J1012+5307 presented in the first column of Table 3.2. For comparison, in the second column the measured

---

[2]http://www.atnf.csiro.au/research/pulsar/tempo/

Table 3.1: **Properties of the individual telescope datasets.**

Properties	Effelsberg	Jodrell Bank	Westerbork	Nançay
Number of TOAs	1972	600	234	86
Time span (MJD)	50371-54717	49221-54688	51389-54638	53309-54587
Post-fit rms (μs)	2.7	8.6	2.9	1.9
Frequencies (MHz)	860, 1400, 2700	410, 606, 1400	330, 370, 800, 1380	1400

parameters of only the current Effelsberg set is shown and in the third the Effelsberg measurements from Lange et al. (2001). From Table 3.2 it is clear that the EPTA provides the most accurate error estimations and in addition $\sim 3\sigma$ measurements of 2 post-Keplerian parameters.

3.3 Analysis & Results

All the combined TOAs, weighted by their their individual uncertainties, were analysed with Tempo, using the DE405 ephemeris of the Jet Propulsion Laboratory (JPL) (Standish 1998, 2004) and the ELL1 (Lange et al. 2001) binary model. This model is optimal for small orbit eccentricities. In general, for deriving the Keplerian parameters of the orbit the Römer delay (caused by the orbital motion of the pulsar) is used as:

$$\Delta_{RB} = x(\cos E - e)\sin\omega + x\sin E\sqrt{1-e^2}\cos\omega \qquad (3.1)$$

(Blandford & Teukolsky 1976), where x is the projected semi-major axis, E the eccentric anomaly, e the eccentricity and ω the longitude of the periastron. However, in small eccentricity binary pulsars the periastron location cannot be well-defined because of a high correlation between ω and T_0 (epoch of the ascending node) in a χ^2 estimation of these parameters. ELL1 model is overcoming this problem by describing the Keplerian motion in a different way. For first order approximation equation (3.1) can be written as:

$$\Delta_{RB} \simeq x\left(\sin\Phi + \frac{\kappa}{2}\sin 2\Phi - \frac{\eta}{2}\cos 2\Phi\right), \qquad (3.2)$$

where $\Phi = \frac{2\pi}{P_b}(T - T_{asc})$ is measured from the ascending node and terms constant in time are omitted. $T_{asc} = T_0 - \omega\frac{P_b}{2\pi}$ is the time of the ascending node and $\eta = e\sin\omega$ and $\kappa = e\cos\omega$ are the first and second Laplace-Lagrange parameters respectively. For most of the low-eccentricity binary pulsars this model is sufficient.

Tempo minimises the sum of the weighted squared timing residuals, producing a set of improved pulsar parameters and the post-fit timing residuals. The uncertainties on the TOAs from each telescope are scaled by an appropriate factor to achieve a uniform reduced $\chi^2 \simeq 1$ for each data set. The best post-fit timing solution of all the combined residuals is presented in Figure 3.1. In the top panel the post-fit residuals versus time are shown, with arbitrary offsets of the different datasets. It is clear that the uncertainties of most of the data points are comparable. By comparing the parameters we get from different combinations of data sets (i.e. only the 1400 MHz data or all sets but excluding the Jodrell data) we concluded that it is much more efficient to finally use all the available datasets together, as shown in the lower panel of Figure 3.1.

Table 3.2: Timing parameters for PSR J1012+5307. Comparison between the datasets from EPTA, Effelsberg until 2008 and Effelsberg until 2001 (Lange et al. 2001).

Parameters	EPTA	Effelsberg 2008	Effelsberg 2001
RA, α (J2000)	$10^h12^m33^s.4341010(99)$	$10^h12^m33^s.434089(13)$	$10^h12^m33^s.43364(3)$
DEC, δ (J2000)	$53°07'02".60070(13)$	$53°\ 07'\ 02".6001(2)$	$53°07'02".5878(4)$
μ_α (mas yr^{-1})	2.562(14)	2.56(2)	2.62(13)
μ_δ (mas yr^{-1})	-25.61(2)	-25.49(2)	-25.0(2)
Parallax, π (mas)	1.22(26)	0.8(3)	<1.6
ν (Hz)	190.2678376220576(5)	190.2678376220611(8)	190.267837621910(3)
$\dot{\nu}$(s^{-2})	$-6.20063(3)\times10^{-16}$	$-6.20077(5)\times10^{-16}$	$-6.2070(5)\times10^{-16}$
P (ms)	5.255749014115410(15)	5.25574901411531(2)	0.00525574901411947(7)
$\dot{P}$ (s s^{-1})	$1.712794(9)\times10^{-20}$	$1.712833(13)\times10^{-20}$	$1.71456(15)\times10^{-20}$
Epoch (MJD)	50700.0	50700.0	50700.0
DM (cm^{-3} pc)	9.02314(7)	9.0209(3)	9.022(3)
Orbital period, P_b (days)	0.60467271355(3)	0.60467271355(4)	0.6046727133(2)
Projected semi-major axis, x (lt-s)	0.5818172(2)	0.5818175(2)	0.5818174(5)
$\eta\ (\equiv e\sin\omega)$	$1.2(3)\times10^{-6}$	$1.6(3)\times10^{-6}$	$1.1(5)\times10^{-6}$
$\kappa\ (\equiv e\cos\omega)$	$0.06(31)\times10^{-6}$	$0.14(34)\times10^{-6}$	$0.20(50)\times10^{-6}$
Eccentricity, e *	$1.2(3)\times10^{-6}$	$1.6(3)\times10^{-6}$	$1.1(5)\times10^{-6}$
Longitude of periastron, ω* (deg)	93(14)	85(12)	79(24)
T_{ASC} (MJD)	50700.08162891(4)	50700.08162891(5)	50700.08162905(9)
$\dot{P}_b$ (s s^{-1})	$5.0(1.4)\times10^{-14}$	$4(2)\times10^{-14}$	$0.3(3)\times10^{-12}$
$\dot{x}$ (s s^{-1})	$2.3(8)\times10^{-15}$	$<1.8\times10^{-15}$	$<1.8\times10^{-15}$
Solar system ephemeris	DE405	DE405	DE200
No of TOAS	2892	1972	1213
RMS timing residual (μ s)	3.1	2.6	3.1

*: The eccentricity and the longitude of the periastron are calculated from the Laplace-Lagrange parameters η and κ.

Figures in parentheses are the nominal 1σ tempo uncertainties in the least-significant digits quoted
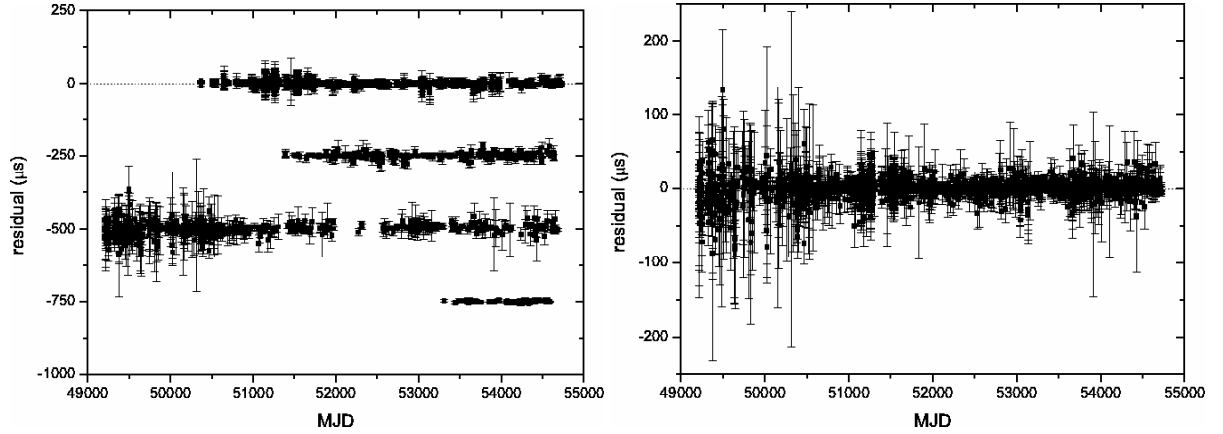
Figure 3.1: **(Top) Post-fit timing residuals for the dataset of each telescope. From top to bottom, Effelsberg, Westerbork, Jodrell and Nançay. (Bottom) Post-fit timing residuals. Best timing solution with all the data sets yields the parameters in Table 3.2.**

3.3.1   Timing parallax & distance

Apart from the common method of DM distance estimation ($\sim 410\,\text{pc}$) and the optical estimate ($d = 840 \pm 90\,\text{pc}$) for PSR J1012+5307, there is yet another way of measuring the distance to a pulsar; with pulsar timing. In general, the timing residuals of nearby pulsars demonstrate an annual variation caused by parallax. This timing parallax is obtained by measuring a time delay of the TOAs caused by the curvature of the emitted wavefronts at different positions of the Earth in its orbit. The time delay has an amplitude of $r_{E\odot}^2 \cos\beta/(2cd)$ (Lorimer & Kramer 2005), where $r_{E\odot}$ is the Earth-Sun distance, β the ecliptic latitude of the pulsar, c the speed of light and d the distance to the pulsar. This effect has been measured for very few pulsars like PSR B1855+09 (Kaspi et al. 1994), PSR J1713+0747 (Splaver et al. 2005), PSR J0437−4715 (Verbiest et al. 2008), PSR J1744−1134 (Toscano et al. 1999b), PSR J2145−0750 (Löhmer et al. 2004) and PSR J0030+0451 (Lommen et al. 2006), that are either close to the solar system or at very low ecliptic latitudes. Here for the first time we measure a parallax $\pi = 1.2 \pm 0.3\,\text{mas}$ for PSR J1012+5307. The parallax corresponds to a distance of $d = 822 \pm 178\,\text{pc}$ which is consistent with the $d = 840 \pm 90$ pc measured from the optical observations. The difference with the DM distance may point to a sparse free electron distribution in this location of the Galaxy (Gaensler et al. 2008; Chatterjee et al. 2009). By combining the optical and timing parallax distance measurements we calculate the weighted mean of the distance:

$$\bar{d} = \frac{\sum_i^n w_i d_i}{\sum_i^n w_i} \tag{3.3}$$

where $w_i = 1/\sigma_i$ are the weights and d_i are the two distances (Wall & Jenkins 2003). We finally get an improved value of $d = 836 \pm 80\,\text{pc}$.

3.3.2   Improved 3D velocity measurement & Galactic motion

Combining the proper motion measured from timing (Table 3.2) and the distance to the system and the radial velocity of $v_r = 44 \pm 8\,\text{km}^{-1}\text{s}$ from the optical observations of the WD, Lange

et al. (2001) managed to determine the full 3D motion of the pulsar relative to the SSB. Our new timing results improve the proper motion measurements by an order of magnitude and using the combined parallax and optical distance we reestimate the 3D motion of the pulsar. We derive transverse velocities of

$$v_\alpha = \mu_\alpha d = 10.2 \pm 1.0 \, \text{km s}^{-1} \tag{3.4}$$

and

$$v_\delta = \mu_\delta d = 101.5 \pm 9.7 \, \text{km s}^{-1}. \tag{3.5}$$

This yields a total transverse velocity of

$$v = \sqrt{v_\alpha^2 + v_\delta^2} = 102.0 \pm 9.8 \, \text{km s}^{-1}. \tag{3.6}$$

Using the radial velocity from the optical measurements ($v_r = 44 \pm 8 \, \text{km}^{-1}\text{s}$) we finally get the space velocity of the system which is

$$v_{space} = \sqrt{v^2 + v_R^2} = 111.4 \pm 9.5 \, \text{km s}^{-1}, \tag{3.7}$$

consistent and almost three times more precise than the previous value. In addition, this value is still consistent with the average space velocity of millisecond pulsars of $130 \, \text{km s}^{-1}$ (Lyne et al. 1998; Toscano et al. 1999b). All the velocity and distance components are presented schematically in Figure 3.2.
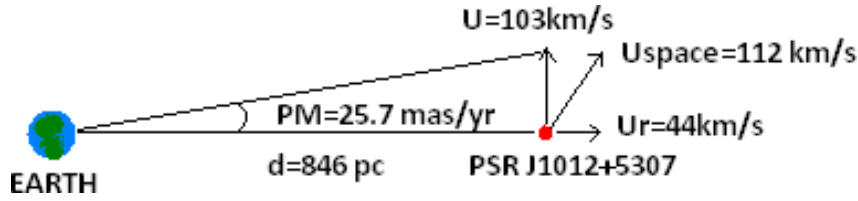
Figure 3.2: **Distance and velocity components of PSR J1012+5307.**

Since we know the 3D velocity of PSR J1012+5307 we can try for the first time to track its Galactic path in time and space. Assuming a characteristic age of $\sim 10 \, \text{Gyr}$ and applying a model for the Galactic potential (Kuijken & Gilmore 1989; Paczyński 1990), we derive the evolutionary path of PSR J1012+5307 in the Galaxy from the point it started emitting as a millisecond pulsar. In the top part of Figure 3.3 and 3.4, the projection of the evolutionary path of the pulsar on the Galactic plane is shown, where the arrow indicates the current position of the pulsar is pointed and the star indicates the position of the Sun, for the Kuijken & Gilmore (1989) and the Paczyński (1990) model respectively. It is obvious that the pulsar is presently at one of its closest approaches to the Sun, which is why we can actually observe it. PSR J1012+5307 reaches maximum distances of $\sim 30 \, \text{kpc}$ and $\sim 25 \, \text{kpc}$, for the first and second model respectively, through its path, spending only a small fraction of its lifetime close to the solar system orbit. In Figures 3.3 and 3.4 (bottom) the movement of PSR J1012+5307 on the z-axis (above and below the Galactic plane) is shown versus time indicating that the pulsar is oscillating with a period of $\sim 0.6 \, \text{Gyr}$ reaching a maximum distance of $\sim 7 \, \text{kpc}$ and $\sim 4 \, \text{kpc}$ (model 1 and 2 respectively) above and below the Galactic plane. The differences in the distances derived from the two models are caused by the different (larger) mass-density distribution assumption of the Paczyński (1990).
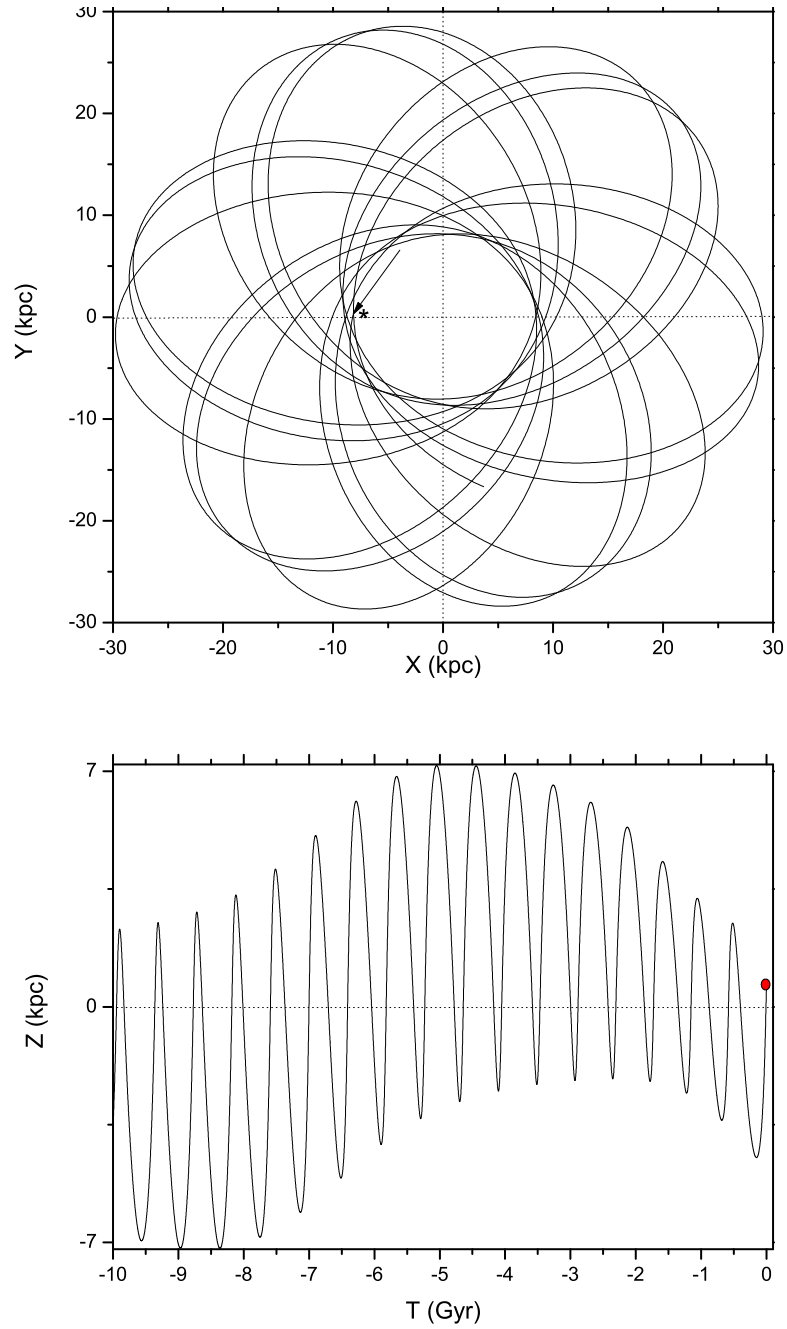
Figure 3.3: **(Top) Evolutionary path of PSR J1012+5307 on the Galactic plane. With arrow the current position of the pulsar and with ∗ the position of the Sun is noted. (Bottom) The oscillations of PSR J1012+5307 above and below the Galactic plane through time. The Galactic potential model of Kuijken & Gilmore (1989) has been used.**

3.3.3   Eccentricity

PSR J1012+5307 is a low eccentricity binary system. In our current timing solution we measure a value for the eccentricity of $1.2 \pm 0.3 \times 10^{-6}$. However, as shown in Lange et al. (2001), the
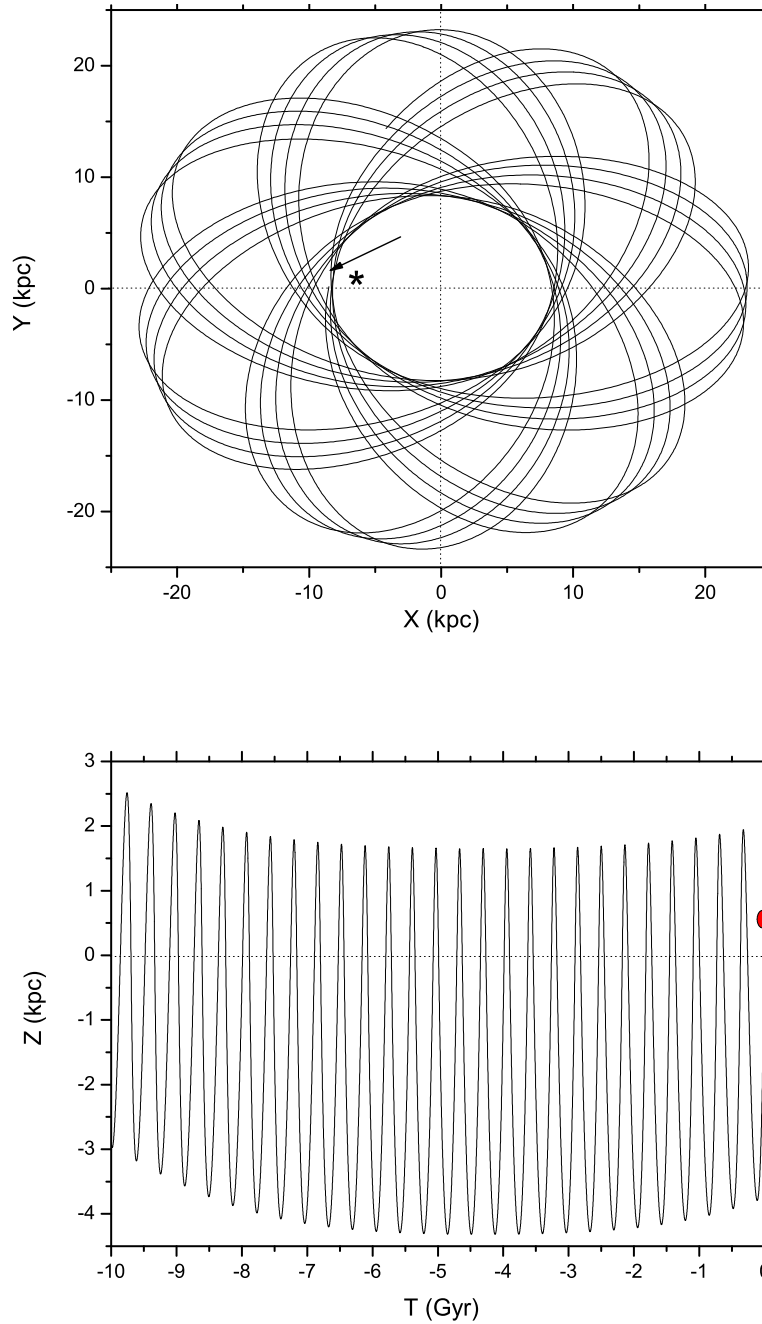
Figure 3.4: **(Top) Evolutionary path of PSR J1012+5307 on the Galactic plane. With arrow the current position of the pulsar and with ∗ the position of the Sun is noted. (Bottom) The oscillations of PSR J1012+5307 above and below the Galactic plane through time. The Galactic potential model of Paczyński (1990) has been used.**

Shapiro delay, caused by the gravitational field of the companion, cannot be separated from the Römer delay for this system, which leads to a small correction to this eccentricity value and specifically to the first Laplace-Lagrange parameter $\eta = e\,sin\omega$. Analytically, for low-

eccentricity pulsars the Shapiro delay can be written as

$$\Delta_S = -2r \ln(1 - s \sin \Phi) \tag{3.8}$$

where r and s is the range and shape of the Shapiro delay respectively. As a Fourier series it takes the form

$$\Delta_S = 2r(\alpha_0 + b_1 \sin \Phi - \alpha_2 \cos 2\Phi + ...), \tag{3.9}$$

where

$$\alpha_0 = -\ln\left(\frac{1 + \sqrt{1 - s^2}}{2}\right), \tag{3.10}$$

$$b_1 = 2\frac{1 - \sqrt{1 - s^2}}{s}, \tag{3.11}$$

$$a_2 = 2\frac{1 - \sqrt{1 - s^2}}{s^2} - 1, \tag{3.12}$$

(Lange et al. 2001). Higher harmonics are significant only for nearly edge-on orbits. Otherwise, as in the current case, the Römer delay cannot be separated from the Shapiro delay and the observed values of x and η are different from their intrinsic values by

$$x_{obs} = x + 2rb_1 \tag{3.13}$$

and

$$\eta_{obs} = \eta + 4r\alpha_2/x. \tag{3.14}$$

For a companion mass of $m_c = 0.16(2)\,M_\odot$, a mass ratio $q=10.5(5)$ and a mass function of $f_m = \frac{(m_c \sin i)^3}{(m_p + m_c)^2} = \frac{4\pi^2}{T_\odot}\frac{x^3}{P_b^2} = 0.000578\,M_\odot$ where the constant $T_\odot = GM_\odot/c^3 = 4.9255\,\mu s$, we derive the range r and shape s of the Shapiro delay according to

$$r[\mu s] = 4.9255(m_c/M_\odot) \tag{3.15}$$

and

$$s = \sin i = \left[\frac{f_m(q + 1)^2}{m_c}\right]^{1/3}. \tag{3.16}$$

The intrinsic value of η, calculated from equation (3.14), due to the contribution of the Shapiro delay, is $\eta = (-1.4 \pm 3.4) \times 10^{-7}$. The true eccentricity of the system is $e = \sqrt{\eta^2 + \kappa^2}$, where $\kappa = e \cos \omega = (0.6 \pm 3.1) \times 10^{-7}$. By solving this equation in a Monte Carlo simulation (Figure 3.5), for datasets of the values and uncertainties of the intrinsic η and κ, we obtain an upper limit for the intrinsic eccentricity:

$$e < 5.2 \times 10^{-7} \qquad \text{(68 per cent C.L.)} \tag{3.17}$$

$$e < 8.4 \times 10^{-7} \qquad \text{(95 per cent C.L.)} \tag{3.18}$$

This limit is better than the previously published value (Lange et al. 2001).

This improved limit has another significant importance. In Chapter 1 we have presented the various evolutionary paths for different kinds of pulsar binary systems. Especially we showed that for the pulsar low-mass white dwarf systems the most popular spin-up mechanism of the pulsar is the mass transfer from the Roche-lobe overflow of the companion while it is in the
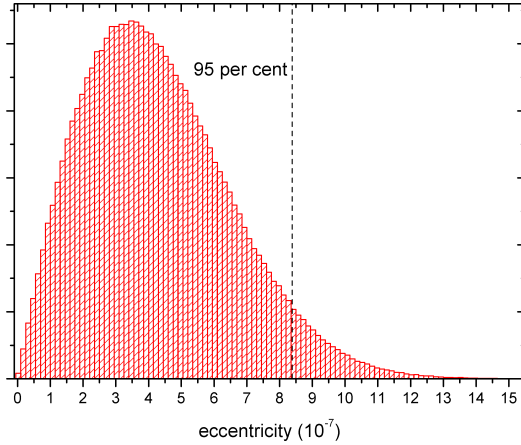
Figure 3.5: **Distribution of values for the intrinsic eccentricity from Monte Carlo simulations.The dashed line cuts the distribution at the 95 per cent of the values.**

red giant phase. In general, after the initial supernova creates the NS in a low mass binary the eccentricity will be high (> 0.1). While the companion is evolving to the red giant phase tidal forces from the NS are being balanced by convective eddy viscosity on a much shorter timescale than the lifetime of the giant. Thus, we would expect to have eccentricities of the order of exp(-1000) (Phinney & Kulkarni 1994). However, this is not what we measure for these systems.

Phinney (1992) showed that tidal dissipation is not the only process acting. Using the fluctuation-dissipation theorem he predicted that the orbital eccentricity, of a pulsar-WD binary system, is correlated with the orbital period. Specifically, there is the theoretical prediction of a relic orbital eccentricity due to convective eddy currents in the mass accretion process of the neutron star from the companion while in the red giant phase.

We plot our new eccentricity limit of PSR J1012+5307 versus the orbital period as shown in Figure 3.6 together with other low-mass binaries ($m_c < 0.9\,\mathrm{M_\odot}$) (their values were taken from Lorimer (2005)) and compare it with the model curves of the Phinney & Kulkarni (1994) model. Our current eccentricity limit is much lower than the one in Lange et al. (2001), but still in good agreement with the predictions from this model. Combined with the agreement of the characteristic age of the pulsar with the cooling age of the WD (Lange et al. 2001) we are confident that the evolutionary scenario of spin-up through mass transfer from the companion is valid for PSR J1012+5307.

3.3.4 Changes in projected semi-major axis

A change in the projected semi-major axis has been measured in the current analysis, for the first time, for PSR 1012+5307. Initially, in order to inspect the variation of x through time we made a plot of it versus the MJD for the largest part of our observations (similar to the stridefit plug-in of tempo2). Specifically, each x value is calculated for one year of TOAs while all the other parameters apart from spin and orbital period are being held fixed. It is clear from the linear fit in Figure 3.7 that there is an increase in the value of x over time. The observed value of $\dot{x}_{obs} = 2.3(8) \times 10^{-15}\,\mathrm{s\,s^{-1}}$ can be the result of the various effects shown in equation (3.19)
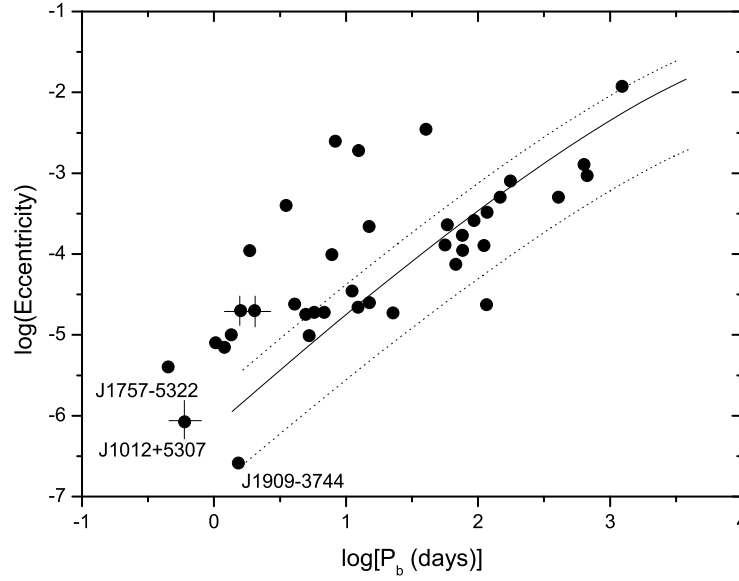
Figure 3.6: **Eccentricity versus orbital period of 39 pulsar-low-mass-WD systems. The points with the crosses are upper limits. The solid line is the model curve of Phinney & Kulkarni (1994) and the dotted lines show the 95% confidence limit of this relationship.**

(Lorimer & Kramer 2005):

$$\dot{x}_{obs} = \dot{x}^D + \dot{x}^{GW} + \frac{d\epsilon_A}{dt} + \dot{x}^{\dot{m}} + \dot{x}^{SO} + \dot{x}^{planet} + \dot{x}^{PM}. \tag{3.19}$$

The first term, $\dot{x}^D$, is the Doppler correction, which is the combined effect of the proper motion of the system (Shklovskii 1970) and a correction term for the Galactic acceleration. The former effect was introduced by Shklovskii and it is an increase in the projected distance of the pulsar to the SSB, thus to the pulsar period, caused by the transverse velocity of the pulsar. The latter effect, is arising from an actual change in the distance of the pulsar to the SSB which can be caused by differential rotation of the Galaxy, by a third massive body close to the binary system or by acceleration in the gravitational field of the Galaxy (or a globular cluster). The contribution for the Galactic acceleration, $(\dot{x}/x)^{Gal}$ is of order 6×10^{-20}. Furthermore, we calculate the contribution of the Shklovskii effect to be $\dot{x}^{Shk} = x(\mu_\alpha^2 + \mu_\delta^2)d/c \sim 8 \times 10^{-19}$. Both the contributions are very small compared to the observed value, thus, this term can be neglected.

The second term, $\dot{x}^{GW}$ is arising from the shrinking of the orbit due to gravitational-wave damping

$$\dot{x}^{GW} = -x\frac{64}{5}\left(\frac{2\pi}{P_b}\right)^{8/3}\frac{(T_\odot m_c)^{5/3}q}{(q+1)^{1/3}} = (-8.2 \pm 1.7) \times 10^{-20} \tag{3.20}$$

(Peters 1964), where $T_\odot = GM_\odot/c^3 = 4.9255\,\mu s$ and m_c is expressed in units of solar masses,
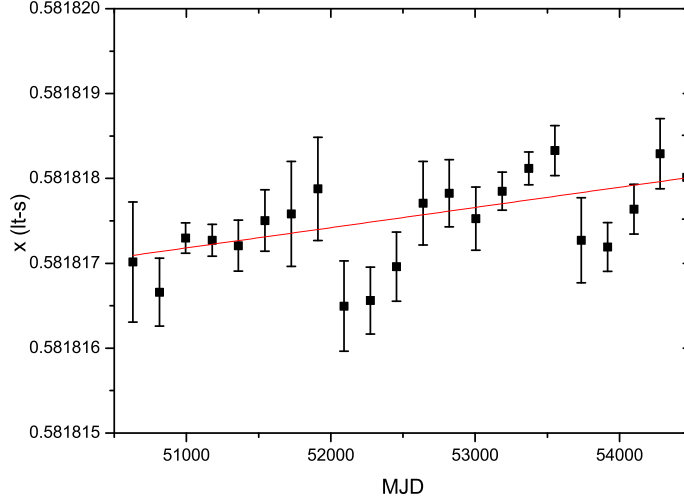
Figure 3.7: **Projected semi-major axis versus time. Clear indication of a variation.**

x is the projected semi-major axis and P_b the orbital period. This contribution again is much smaller than the current measurement precision.

The third term, $\frac{d\epsilon_A}{dt}$, is the contribution of the varying aberration caused by geodetic precession of the pulsar spin axis, and is typically of order $\Omega^{geod} P/P_b \approx 2 \times 10^{-18}$ (Damour & Taylor 1992). For a recycled pulsar, like PSR J1012+5307, the spin is expected to be close to parallel to the orbital angular momentum, which further suppresses this effect. Hence, the contribution is at least three orders of magnitude smaller than the observed.

The fourth term, $\dot{x}^{\dot{m}}$, is representing a change in the size of the orbit caused by mass loss from the binary system. We investigate the mass loss due to the loss of rotation energy by the pulsar, which we consider as the dominant mass-loss effect. We initially calculate the change in the orbital period from that same contribution as follows:

$$\dot{P}_b^{\dot{m}} = 8\pi^2 \frac{I_p}{c^2 M} \frac{\dot{P}}{P^3} P_b \sim 10^{-16}, \tag{3.21}$$

where $M = m_p + m_c$ and the moment of inertia of the pulsar $I_p \sim 10^{45}$ g cm^2. Subsequently, by Kepler's third law we calculate the change in the projected semi-major axis of the orbit to be $\sim 10^{-17}$. Thus, we can also neglect this contribution.

The fifth and the sixth terms, $\dot{x}^{SO}$ and $\dot{x}^{planet}$, are the contributions due to the classical spin-orbit coupling caused by a spin-induced quadrupole moment of the companion and the existence of an additional planetary companion respectively. They can both be neglected. For the first one to be significant, a main-sequence star or a rapidly rotating white dwarf companion (Wex et al. 1998; Kaspi et al. 2000) would be necessary. The second is not being considered because there is no evidence for another companion to the pulsar.

Since all the other contributions are much smaller than the observed variation of the projected semi-major axis, we conclude that the measured value is arising from the last term of equation (3.19), $\dot{x}^{PM}$. This is a variation of x caused by a change of the orbital inclination while the binary system is moving relatively to the SSB (Arzoumanian et al. 1996; Kopeikin

1996; Sandhu et al. 1997). The measurement of the effect is presented in the following equation:

$$\dot{x}^{PM} = 1.54 \times 10^{-16} \, x \, \cot i (-\mu_\alpha \sin \Omega + \mu_\delta \cos \Omega), \tag{3.22}$$

where Ω is the position angle of the ascending node. The quantities x, μ_α and μ_δ are expressed in seconds and milliarcseconds per year, respectively. The proper motions and the inclination angle have been measured and since we measure the value of $\dot{x}^{PM} = \dot{x}_{obs}$, we can, for the first time, restrict the orbital orientation Ω of PSR J1012+5307. In Figure 3.8 the $\dot{x}^{PM}$ versus the position angle of the ascending node is presented. Unfortunately, our measured value cannot fully restrict the orientation, however from the lower limits of $\dot{x}_{obs}$ we derive significant limits for the position angle. For an inclination angle of $i = 52°$ we get:

$$151° < \Omega < 220° \quad \text{(68 per cent C.L.)} \tag{3.23}$$

and

$$117° < \Omega < 255° \quad \text{(95 per cent C.L.),} \tag{3.24}$$

while for $i = 128°$

$$\Omega < 40° \quad \& \quad \Omega > 331° \qquad \text{(68 per cent C.L.)} \tag{3.25}$$

and

$$\Omega < 74° \quad \& \quad \Omega > 297° \qquad \text{(95 per cent C.L.).} \tag{3.26}$$
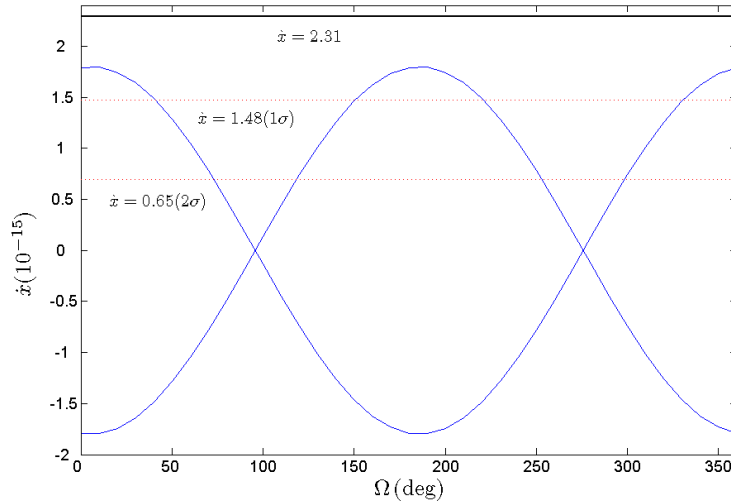
Figure 3.8: **Change of the projected semi-major axis versus position angle of the ascending node. The two curves have been produced for** $i = 52°$ **(peak at** $180°$**) and** $i = 128°$ **(peak at** $0°$**). The solid line represents the measured value of** $\dot{x}$ **and the dashed lines the** 1σ **and** 2σ **limits of** $\dot{x}$**, from top to bottom. The latter constrains the orientation** Ω**.**

3.3.5 Orbital period variations

In order to inspect the variation of P_b through time we also made a plot of it versus the MJD for the largest part of our observations, as in the previous section. It is again clear from the linear fit in Figure 3.9 that there is an increase in the value of P_b over time. There are several effects that can contribute to changes in the observed orbital period of a binary system that can be either intrinsic to the orbit or just kinematic effects. The most important terms are :

$$\dot{P}_b = \dot{P}_b^{\dot{m}} + \dot{P}_b^{T} + \dot{P}_b^{D} + \dot{P}_b^{GW} + \dot{P}_b^{\dot{G}}. \tag{3.27}$$

$\dot{P}_b$ is the observable rate of change of the orbital period, that is for the first time measured here for PSR J1012+5307 to be $\dot{P}_b = 5.0(1.4) \times 10^{-14} s\ s^{-1}$.
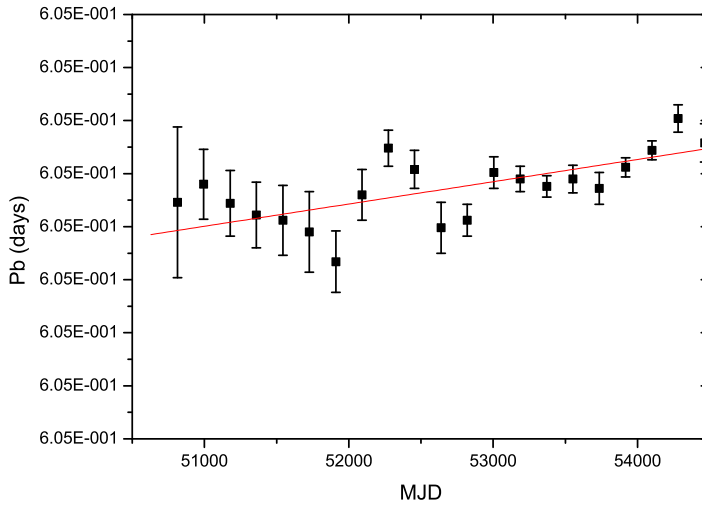
Figure 3.9: **Orbital period versus time. Clear indication of a variation.**

The first and second terms, $\dot{P}_b^{\dot{m}}$, $\dot{P}_b^{T}$, are the contributions from the mass loss from the binary and from tidal torques respectively. They can both be neglected in the case of PSR J1012+5307 because the first one is very small, as shown before ($\sim 10^{-16}$), and the second is also small due to the lack of interaction between the pulsar and the companion.

The third term, $\dot{P}_b^{D}$, is identical to the first term of equation (3.19). In order to account for the galactic acceleration we have extended the Damour & Taylor (1991) expression (for a flat rotation curve) to high Galactic latitudes

$$\left(\frac{\dot{P}_b}{P_b}\right)^{Gal} = -\frac{K_z|\sin b|}{c} \\ -\frac{\Omega_\odot^2 R_\odot}{c}\left(\cos l + \frac{\beta}{\beta^2 + \sin^2 l}\right)\cos b, \tag{3.28}$$

where $\beta \equiv (d/R_\odot)\cos b - \cos l$. K_z is the vertical component of Galactic acceleration taken from Holmberg & Flynn (2004), which for Galactic heights $z \equiv |d\sin b| \leq 1.5$ kpc can be

approximated with sufficient accuracy by

$$K_z(10^{-9}\,\mathrm{cm\,s^{-2}}) \simeq 2.27\,z_{\mathrm{kpc}} + 3.68\left(1 - e^{-4.31\,z_{\mathrm{kpc}}}\right)\,,\tag{3.29}$$

where $z_{\mathrm{kpc}} \equiv z(\mathrm{kpc})$. K_z was derived by analysing a sample of K giant stars from Hipparhos satellite and by determining the gravitational potential of the local Galactic disc, by comparing the number of giant stars observed in the cone (sample extending 1 kpc vertical to the Galactic plane) with the number expected for various models of the matter distribution in the disc. $R_\odot = 8.0 \pm 0.4$ (Eisenhauer et al. 2003), deduced from the orbit of the star S2 around the massive black hole in the Galactic centre, and $\Omega_\odot = 27.2 \pm 0.9$ km/s/kpc (Feast & Whitelock 1997), derived from Hipparchos proper motions of Galactic Cepheids and ground-based photometry, are the Sun's Galactocentric distance and galactic angular velocity (= Oort's $A - B$). For the pulsar's galactic coordinates of $l = 160.3°$ and $b = 50.9°$ we find

$$\dot{P}_b^{\mathrm{Gal}} = (-5.6 \pm 0.2) \times 10^{-15}\,.\tag{3.30}$$

We also calculate the contribution due to the Shklovskii effect according to the following:

$$\dot{P}_b^{Shk} = \frac{(\mu_\alpha^2 + \mu_\delta^2)d}{c}P_b = (7.0 \pm 0.7) \times 10^{-14}\tag{3.31}$$

where we used the measured proper motion and the weighted mean of the distance discussed earlier, d. So, by summing we yield the Doppler correction:

$$\dot{P}_b^D = \dot{P}_b^{Gal} + \dot{P}_b^{Shk} = (6.4 \pm 0.7) \times 10^{-14}.\tag{3.32}$$

The fourth term, $\dot{P}_b^{GW}$, is the contribution due to gravitational wave emission. In general relativity, for circular orbits it is given by:

$$\dot{P}_b^{GW} = \dot{P}_b^{GR} = -\frac{192\,\pi}{5}\left(\frac{2\pi}{P_b}\right)^{5/3}\frac{(T_\odot\,m_c)^{5/3}q}{(q+1)^{1/3}}.\tag{3.33}$$

For PSR J1012+5307 we find $\dot{P}_b^{GW} = (-1.1 \pm 0.2) \times 10^{-14}$.

3.3.6   Testing general relativity and alternative theories of gravity

Equivalence principles are fundamental to gravitational theory. The earliest of all, the Weak Equivalence Principle (WEP), affirms that in an external gravitational field, different objects (in mass and composition) experience the same acceleration. The Einstein Equivalence Principle (EEP) combines the WEP with the local Lorentz invariance (independency of the velocity of the freely falling reference frame) and the positional invariance (no preferred locations) for non-gravitational experiments. Finally, the Strong Equivalence Principle (SEP) is actually expanding EEP by including experiments on objects with strong self-gravitation. General Relativity (GR) embodies SEP completely.

All the calculated terms in the previous section are the ones that are expected to contribute by using GR as our theory of gravity. However, there are alternative theories of gravity, like the tensor scalar theories (in addition to the tensor field, a scalar field exists coupled to matter with gravitational strength), that violate the SEP (the fact that all bodies fall with the same acceleration in an external gravitational field independently of the strength of their self-gravity)

and predict an extra contribution to the observed orbital period variation, via dipole radiation[3] (see Will (1993, 2001) and references therein). This dipolar gravitational radiation results from the difference in gravitational binding energy of the two bodies of a binary system, and is expected to be much larger than the quadrupolar contribution, especially if the binding energies of the two bodies of the binary system differ significantly. Thus, the case of PSR J1012+5307, where there is a pulsar-WD system, is ideal for testing the strength of such emission. One finds

$$\dot{P}_b^{dipole} = -\kappa_D S^2 \frac{(2\pi)^2 T_\odot \mu}{P_b}(1 + \frac{1}{2}e^2)(1 - e^2)^{-5/2} , \qquad (3.34)$$

where m_c is expressed in units of solar masses. κ_D refers to the dipole self-gravitational contribution, which takes different values for different theories of gravity (zero for GR) and $\mathcal{S} = s_p - s_c$ is the difference in the "sensitivities" of the two bodies (see Will (1993)), and μ is the reduced mass, $m_p m_c/M$, of the system. The sensitivity of a body is related to its gravitational self-energy ε. In the post-Newtonian limit $s \simeq \varepsilon/mc^2$, which gives $\sim 10^{-4}$ for a white dwarf (Will 2001). Hence, we can neglect s_c in equation (3.34) since $s_p \sim 0.2$. Using the mass ratio q and $e \simeq 0$, equation (3.34) can be written as

$$\dot{P}_b^{dipole} = -4\pi^2 \frac{T_\odot m_c}{P_b} \frac{q}{q+1} \kappa_D s_p^2 . \qquad (3.35)$$

For a specific theory of gravity κ_D is known and s_p can be calculated as a function of the equation-of-state of neutron star-matter.

Finally, there are theories that predict that the locally measured gravitational constant G changes with time as the universe expands. A changing gravitational constant would cause a change in the orbital period, which for neutron star-WD systems was first considered by Damour et al. (1988) to be:

$$\dot{P}_b^{\dot{G}} \simeq -2\frac{\dot{G}}{G}P_b. \qquad (3.36)$$

Nordtvedt (1990) expanded the previous by taking into account the effects of this variation to the neutron star structure and by introducing an extra sensitivity factor (sensitivity to changes of the gravitational constant) s_p:

$$\dot{P}_b^{\dot{G}} = -2\frac{\dot{G}}{G}\left[1 - \left(1 + \frac{m_c}{2M}\right)s_p\right]P_b , \qquad (3.37)$$

where M is the total mass of the two bodies.

The intrinsic change of the orbital period is the observed value minus the Doppler correction term from equation (3.32):

$$\dot{P}_b^{intr} = \dot{P}_b - \dot{P}_b^D = (-1.5 \pm 1.5) \times 10^{-14} , \qquad (3.38)$$

which agrees well with the GR prediction given above as

$$\dot{P}_b^{exc} = \dot{P}_b^{intr} - \dot{P}_b^{GR} = (-0.4 \pm 1.6) \times 10^{-14} , \qquad (3.39)$$

Hence, there is no need for a $\dot{P}_b^{dipole}$ or $\dot{P}_b^{\dot{G}}$ to explain the observed variation of the orbital period. On the other hand, this can be used to set limits for a wide class of alternative theories of gravity, which we will show in the following sections.

---

[3]In some cases also monopole radiation is considered, however for low eccentricity systems it is negligible.

A generic limit for dipole radiation

A tight system comprising a strongly self-gravitating neutron star and a weakly self-gravitating white dwarf should be a very efficient emitter of gravitational dipole radiation, if there is any deviation from general relativity that leads to a non-vanishing κ_D in equation (3.34). Hence, observations of such systems are ideal to constrain deviations of that kind. PSR J1012+5307 turns out to be a particularly useful system to conduct such a test, since: (1) the white-dwarf nature of the companion is affirmed optically, (2) the mass estimates in this double-line system are free of any explicit strong-field effects[4], which are a priori unknown, if we do not want to restrict our analysis to specific theories of gravity, (3) the estimated mass of the pulsar seems to be rather high, which is important in the case of strong field effects that occur only above a certain critical mass, like the spontaneous scalarisation (Damour & Esposito-Farese 1993).

In the previous section we have shown that the change in the orbital period is in full agreement with the prediction by general relativity, once the kinematic contributions are accounted for. Hence, any deviations from general relativity leading to a different $\dot{P}_b^{GW}$ is either small or compensated for a potential $\dot{P}_b^{\dot{G}}$. However, we can already limit the variation of the gravitational constant by using the published limit of $\dot{G}/G = (4 \pm 9) \times 10^{-13}\,\mathrm{yr}^{-1}$ from the Lunar Laser Ranging (LLR) (Williams et al. 2004). In combination with equation (3.37) it gives $\dot{P}_b^{\dot{G}} = (-1 \pm 3) \times 10^{-15}$, for the most conservative assumption $s_p = 0$. Hence, $\dot{P}_b^{dipole} = (-0.2 \pm 1.6) \times 10^{-14}$, which with the help of equation (3.35) converts into

$$\kappa_D s_p^2 = (0.5 \pm 6.0) \times 10^{-5} \qquad \text{(95 per cent C.L.)}. \qquad (3.40)$$

Furthermore, if we assume $s_p = 0.1(m_p/M_\odot)$ (c.f. Damour & Esposito-Farèse (1992)) we find

$$\kappa_D = (0.2 \pm 2.4) \times 10^{-3} \qquad \text{(95 per cent C.L.)}. \qquad (3.41)$$

This number improves upon the previously published limit for PSR J1012+5307 (Lange et al. 2001) by more than an order of magnitude.

For the tensor-scalar theories of Damour & Esposito-Farese (1996) $\kappa_D \mathcal{S}^2 \simeq (\alpha_p - \alpha_c)^2 \simeq (\alpha_p - \alpha_0)^2 < 6 \times 10^{-5}$, assuming that the effective coupling strength of the companion WD to the scalar field, α_c, is much smaller than the pulsars and is approximately α_0, where α_0 is a reference value of the coupling at infinity. This value is consistent with and improves slightly on the previously published limit of 7×10^{-5} (Nice et al. 2005), obtained from PSR J0751+1807. If the non-linear coupling parameter β_0 is of order 10 or larger, then neutron stars are much more weakly coupled to the scalar field than white dwarfs (Esposito-Farese 2005). In this case, for PSR J1012+5307, $(\alpha_p - \alpha_c)^2 \approx \alpha_0 < 6 \times 10^{-5}$, which is an order of magnitude weaker than the limit 3.4×10^{-6} from PSR J1141−6545 (Bhat et al. 2008). Actually, in tensor-scalar theories of gravity the latter is possibly the most constraining pulsar binary system. However, since there has been no optical identification of the companion, that could establish its WD nature without mass determination based on a specific gravity theory, it is not yet possible to derive a general theory independent limit for dipole radiation from PSR J1141−6545, as done here with PSR J1012+5307.

In the future, more accurate determination of the distance and improvement of our $\dot{P}_b$ value (the uncertainty of $\dot{P}_b$ decreases with time, $t^{-2.5}$ (Lorimer & Kramer 2005)), could further increase the precision of the PSR J1012+5307 limit.

---

[4]The mass estimation for the weakly self gravitating white dwarf companion is done with Newtonian gravity (Callanan et al. 1998), and in any Lorentz-invariant theory of gravity the theoretical prediction for the mass ratio does not contain any explicit strong-field-gravity effects (Damour 2007).

Combined limits on $\dot{G}$ and the dipole radiation with millisecond pulsars

In the previous section we have used the LLR limit for $\dot{G}$ in order to provide a test for dipole radiation with a single binary pulsar system. On the other hand, a generic test for $\dot{G}$ cannot be done with a single binary pulsar, since in general theories that predict a variation of the gravitational constant typically also predict the existence of dipole radiation (Will 1993).[5] From equations (3.34) and (3.37) we can see that $\dot{P}_b^{\dot{G}} \propto P_b$ whereas $\dot{P}_b^{\rm dipole} \propto P_b^{-1}$. Hence, one can combine any two binary pulsars, with tight limits for $\dot{P}_b$ and different orbital periods, in a joint analysis to break this degeneracy, and to provide a test for $\dot{G}$ and the dipole radiation that is based purely on pulsar data. A formally consistent way of doing this with white-dwarf binary pulsars is the application of equation

$$\frac{\dot{P}_b^{exc}}{P_b} = -2\frac{\dot{G}}{G}\left[1 - \left(1 + \frac{m_c}{2M}\right)s_p\right] - 4\pi^2 \frac{T_\odot \mu}{P_b^2}\kappa_{\rm D}s_p^2$$

(3.42)

(see equations (3.37) and (3.34)) to both binary pulsars, and solving in a Monte-Carlo simulation (Figure 3.10) this set of two equations for $\dot{G}/G$ and $\kappa_{\rm D}$. This procedure properly accounts for the correlations due to this mutual dependence, and thus provides a self consistent test for $\dot{G}$ and the dipole radiation, that does not rely on LLR limits or theory specific assumptions. There remains the problem of getting a good estimate for s_p in a general theory independent test. As before, we will use $s_p = 0.1\,(m_p/M_\odot)$ keeping in mind that the limits given below are subject to certain changes, if a different assumption for s_p is made.

With its short orbital period and its fairly well determined masses PSR J1012+5307 is an ideal candidate for such a combined analysis. Presently, the best binary pulsar limit for $\dot{G}$ comes from PSR J0437$-$4715 (Verbiest et al. 2008; Deller et al. 2008), where $\dot{P}_b^{\rm dipole} = 0$ has been used in the analysis to obtain the limit for $\dot{G}$. Using this pulsar in combination with PSR J1012+5307 in a joint analysis as introduced above gives, with a 95 per cent C.L.,

$$\frac{\dot{G}}{G} = (-0.7 \pm 3.3) \times 10^{-12}\,{\rm yr}^{-1} = (-0.009 \pm 0.045)\,H_0$$

(3.43)

and

$$\kappa_{\rm D} = (0.3 \pm 2.5) \times 10^{-3}$$

(3.44)

where $H_0 = 74\,{\rm km\,s}^{-1}\,{\rm Mpc}^{-1}$ has been used as a value for the Hubble constant (Riess et al. 2009). Our pulsar test therefore restricts $\dot{G}/G$ to less than a 20th of the expansion rate of the Universe.

The limit for $\dot{G}$ given here is clearly weaker than the one given in Deller et al. (2008). The main reason for this is that the equation for $\dot{P}_b^{\dot{G}}$ used by Deller et al. (2008) does not account for the sensitivity of the pulsar as in equation (3.37). Furthermore, the combined analysis still allows for a certain range for $\dot{P}_b^{\rm dipole}$ in PSR J0437$-$4715, leading to a somewhat weaker limit compared with an analysis that uses $\dot{P}_b^{\rm dipole} = 0$, as can be seen in Fig. 3.10. Although this limit for $\dot{G}$ is weaker than the LLR limit, it still provides a useful independent addition to the LLR result, as has been argued in Verbiest et al. (2008).

The limit for the dipole radiation is slightly weaker than the one given in the previous section. However, in contrast to the limit of the previous section, the limit here does not rely on the

---

[5]It is interesting to point out, that in the Jordan-Fierz-Brans-Dicke theory $\dot{P}_b^{dipole} + \dot{P}_b^{\dot{G}} = 0$ for binary pulsars with white-dwarf companions that have orbital periods $\sim$10 days.
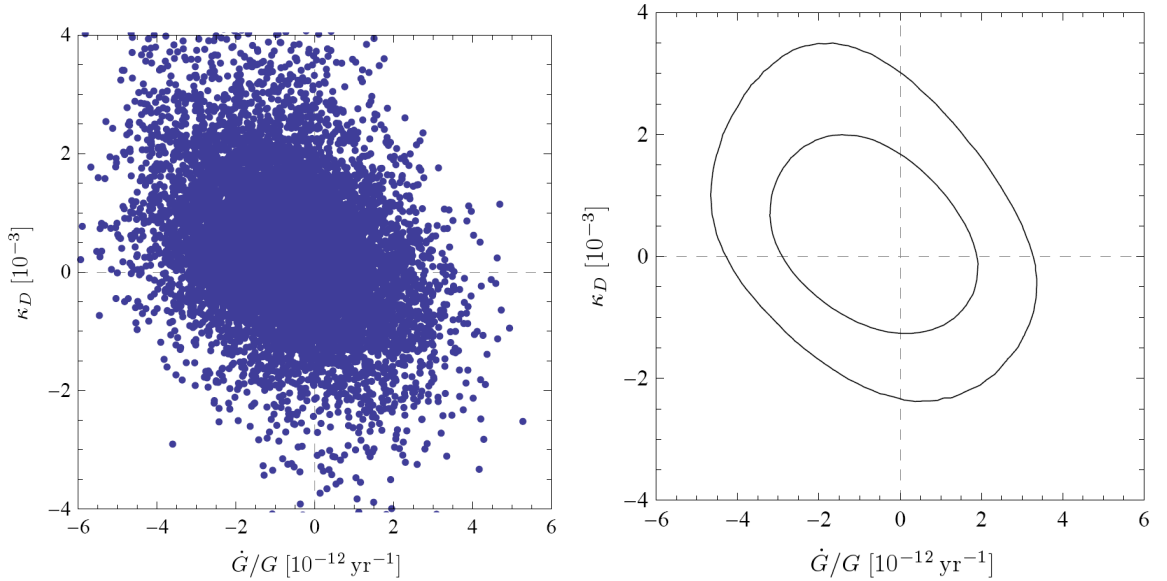
Figure 3.10: (Left) The dipole radiation contribution versus the $\dot{G}/G$ for each of the 10000 iterations of the Monte Carlo simulation for PSR J1012+5307 and PSR J0437-4715. (Right) Contour plots of the one and two σ confidence regions on $\dot{G}/G$ and κ_D jointly. The elongation of the regions reflects the correlation due to the mutual dependence of the two systems, PSR J1012+5307 and PSR J0437$-$4715, in this combined test.

LLR result for $\dot{G}$, and therefore constitutes an independent test based solely on binary pulsar observations.

We would like to stress two facts about the advantage of combining specifically these two binary pulsars. Firstly, in both cases the companion white dwarf is identified optically, and its non-compact nature is ascertained independently of the underlying theory of gravity. Secondly, the two pulsars seem to be rather heavy and similar in mass ($\sim 1.7 M_\odot$)[6], which is important in case we have effects like spontaneous scalarisation above a critical neutron star mass, where the neutron star can develop strong scalar charges even in the absence of external scalar force, i.e. even if $\alpha_0 = 0$ (similar with the spontaneous magnetisation of ferromagnets)(Damour & Esposito-Farese 1993). In the future, more accurate measurements of $\dot{P}_b$ and distance of the two pulsars could constrain even more our derived limits.

In addition, we performed the same analysis using PSR J1012+5307 and PSR J1713+0747 (Splaver et al. 2005), a long-orbit, low-eccentricity binary pulsar-white dwarf system that have been used succesfully to set limits on violations of the SEP. The derived limits with a 95 per cent C.L. are,

$$\frac{\dot{G}}{G} = (-1.5 \pm 3.9) \times 10^{-12} \ \mathrm{yr}^{-1} = (-0.022 \pm 0.053) \, H_0 \tag{3.45}$$

---

[6]In general, PSR J0437$-$4715 does not allow the determination of the pulsar mass, since this requires the mass function, which contains explicit strong-field contributions. Within the generic class of conservative gravity theories (Will (1993); Damour & Taylor (1992)), for instance, only the effective gravitational mass, $\mathcal{G}m_p$, of PSR J0437$-$4715 can be determined. However, if one assumes that $\mathcal{G}$ deviates less than 20 per cent from G, the pulsar mass is in the range of 1.5 to 2.0 solar masses.

and

$$\kappa_{\mathrm{D}} = (0.6 \pm 2.6) \times 10^{-3}. \tag{3.46}$$

The κ_D limit does not differ much, as expected, but the $\dot{G}/G$ limit is 20 per cent weaker than before. In the future, application of our combined analysis to better candidate sources could constrain even more those limits.

3.4 Conclusions

We have presented results from the high precision timing analysis of 15 yr of EPTA data for PSR J1012+5307. A first ever measurement of the timing parallax $\pi = 1.2(3)$ and distance has been obtained for this pulsar. Combined with information from optical observations of the WD companion an improved 3D velocity has been derived for the system. This information enables the derivation of the complete orbital motion of the pulsar in the Galaxy, showing that it spent most of its lifetime far away from the solar system orbit. In addition, an improved limit on the extremely low intrinsic eccentricity, $e < 8.4 \times 10^{-7}$ (95 per cent C.L.), has been acquired, which agrees well with the theoretical eccentricity-orbital period relation (Phinney & Kulkarni 1994).

Of particular interest is the measurement of the variation of the projected semi-major axis, $\dot{x} = 2.3(8) \times 10^{-15}$ which is caused by a change in the orbital inclination as the system moves relative to the SSB. This measurement allowed us to set limits on the positional angle of the ascending node, for the first time, the last unknown parameter in fully describing the orientation of this binary system.

As a result of the significant measurement of the change in the orbital period of the system, $5.0(1.4) \times 10^{-14}$, and the identified nature of the two bodies in this binary system, tests for alternative gravity theories could be performed. Firstly, a stringent, generic limit for the dipole radiation has been obtained from PSR J1012+5307, $\kappa_D s_p^2 = 0.5 \pm 6.0 \times 10^{-5}$ (95 per cent C.L.), with the use of the $\dot{G}$ limit from LLR. Secondly, in a self consistent analysis we have used PSR J1012+5307 together with PSR J0437$-$4715 to derive a combined limit on the dipole radiation and the variation of the gravitational constant, $\kappa_D = (0.4 \pm 2.6) \times 10^{-3}$ and $\dot{G}/G = (-0.7 \pm 3.3) \times 10^{-12}$ yr^{-1} (95 per cent C.L.) respectively. These limits have been derived just with the use of millisecond pulsar-WD binaries and are valid for a wide class of alternative theories of gravity.

4. Millisecond Pulsar Timing II - EPTA Pulsars

Keeping time, time, time,
In a sort of Runic rhyme,
To the tintinnabulation that so musically wells,
From the bells, bells, bells.

Edgar Allan Poe

In this chapter the calibration of the Effelsberg archival data and analysis, described in section 2.2.3, of the rest of the Effelsberg and EPTA candidate millisecond pulsars is presented. In addition, some details and properties of the sources are given together with future prospects of their EPTA high precision timing analysis. In total fourteen sources, observed monthly with Effelsberg radio telescope at at least two different frequencies, have been chosen. From those, three are solitary pulsars, one is in a double neutron star binary system (NS-NS) and ten are in neutron star-white dwarf (NS-WD) binary systems. In Table 4.1 the selected sources are shown with the current post-fit rms achieved in comparison with the post-fit rms without the improved calibration procedures. In all the cases the improvement is vast, varying from two times to two orders of magnitude. Finally, for consistency check, all TOAs were analysed with both tempo and tempo2 and in most cases extremely small differences occur between them only at the level of the second or even third decimal digit. In the last column the post-fit rms with the use of only the 1.4 GHz data is shown.

4.1 PSR J0030+0451

PSR J0030+0451 is a nearby 4.9 ms solitary pulsar (one of the 13 known isolated pulsars). It was independently discovered by the Arecibo Drift Scan Search (Somer 2000) and the Bologna sub-millisecond pulsar survey (D'Amico 2000). With a DM$\sim$4.33 pc/cm^3, the Taylor & Cordes (1993) electron distribution model gave the first estimation for a distance of $d =$230 pc. Lommen et al. (2000) using timing observations with Arecibo radiotelescope derived a value for the change of the orbital period derivative of $\dot{P} \sim (1 \pm 0.2) \times 10^{-20}$ s s^{-1} and a proper motion of $\mu \leq 60 \pm 70$ mas/yr. Nicastro et al. (2001) using scintillation measurements of PSR J0030+0451 calculated its transverse velocity of $\upsilon_t = 9 \pm 6$ km/s, one of the slowest measured for any pulsar.

Recently, Abdo et al. (2009) reported the discovery of γ-ray pulsations from PSR J0030+0451 with the Large Area Telescope (LAT) of the Fermi Gamma-ray Telescope, making it the second

Table 4.1: **The fourteen analysed millisecond pulsars with the post-fit rms with and without calibration. The TOAs are until September 2008 (MJD 54720) and all the available Effelsberg frequencies have been used. On the last column only the 1.4 GHz TOAs have been used.**

Source	Post-fit rms before (μs)	Post-fit rms after (tempo) (μs)	Post-fit rms tempo2 (μs)	Post-fit rms 1.4 GHz (μs)
PSR J0030+0451	—— [a]	5.685	5.677	3.769
PSR J0218+4232	51.538	9.639	9.613	9.087
PSR J0613−0200	28.060	2.661	2.662	2.657
PSR J0621+1002	23.802	6.827	6.880	6.506
PSR J0751+1807	15.527	4.938	4.935	4.275
PSR J1022+1001	16.169	3.740	3.645	3.117
PSR J1024−0719	∼1500	13.418	12.390	2.739
PSR J1518+4904	23.529	18.909	18.965	19.032
PSR J1623−2631	∼2100	3.900	3.897	3.914
PSR J1640+2224	15.241	1.673	1.673	1.474
PSR J1643−1224	34.425	3.922	4.010	3.849
PSR J1744−1134	1.708	0.620	0.618	0.619
PSR J2051−0827	49.867	48.744	48.734	48.873
PSR J2145−0750	4.138	2.565	—— [b]	2.489

[a]: The source was regularly observed from 2008.

[b]: Because of a software bug of tempo2 we cannot yet achieve a full solution for this pulsar.

ms pulsar to be detected in γ-rays. Together with further ms pulsar detections of Fermi they provide a significant new tool for studying the magnetospheres of energetic pulsars.

The highest precision timing analysis to date was achieved by Lommen et al. (2006) reaching a post-fit rms of $\sim 1\,\mu$s by using 6 years of monthly data from the 305m Arecibo telescope at 430 and 1410 MHz. They measured a parallax for the first time of $\pi = 3.3 \pm 0.9$ mas which corresponds to a distance of $d = 300 \pm 90$ pc, agreeing with the dispersion measure derived distance of 317 pc from the Cordes & Lazio (2001) model of Galactic electron distribution. They also confirmed the measurement of Nicastro et al. (2001) of the pulsar's transverse velocity over a range of 8-17 km/s. They calculate a proper motion of -5.74 ± 0.09 mas/yr in the plane of the ecliptic. The proper motion out of the ecliptic plane is difficult to measure due to its low ecliptic latitude. Finally, they performed a statistical analysis of the velocity data of isolated versus binary millisecond pulsars, similar to Hobbs et al. (2005), confirming that there is a similarity between the average velocities of the two populations. However, by also finding a significant difference of the populations in the heights above or below the Galactic plane z (isolated heights are half from the binaries), they concluded that luminosity differences of the two populations accounted for these findings.

PSR J0030+0451 has been observed with Effelsberg radiotelescope for two months during 1999 at 1.4 GHz. Because of that, we did not have enough TOAs to use, until now, for an improvement of the initial ephemeris (containing only position, period and period derivative). Thus, our initial consideration was to include again this source in our monthly timing schedule. PSR J0030+0451 is being observed regularly with Effelsberg at two different frequencies (1.4 and 2.7 GHz) from March 2008.

The second problem, when starting observing it again, was caused by of the lack of an efficient number of high S/N integrated profiles in order to create a template, thus we could not get the accurate TOAs. After six months of monthly observations, we gathered enough high S/N profiles which we summed with the ones from the 1999 observations at 1.4 GHz. After getting the summed profile we used the Gaussian fitting package bfit (Kramer et al. 1994) in order to create a synthetic template for the pulsar and cross correlate it with the individual integrated profiles of each day in order to obtain TOAs. The usual procedure followed for the synthetic template creation has some specific steps. The summed profile is loaded in bfit, scaled (usually to one) and shifted, then smoothed in order to eliminate confusing noise and has its baseline removed. The determination of the Gaussian components best describing the profile is then done by choosing their centre, width and height. To describe a Gaussian function $f(x) = \alpha \, e^{-\frac{(x-b)^2}{2c^2}}$ one needs three parameters, α the height of the peak, b the centre of the peak and c the full width at half maximum (FWHM) of the peak. Finally, after checking for unwanted differences between the Gaussian summed profile with the real profile we use a Downhill-simplex-algorithm[1] to improve the initial values of the parameters (e.g. Kramer et al. (1994)). After fixing everything together we produce the synthetic template. In Figure 4.1 the six Gaussian components that were used for creating the synthetic template, also in the same figure, of PSR J0030+0451 are presented.
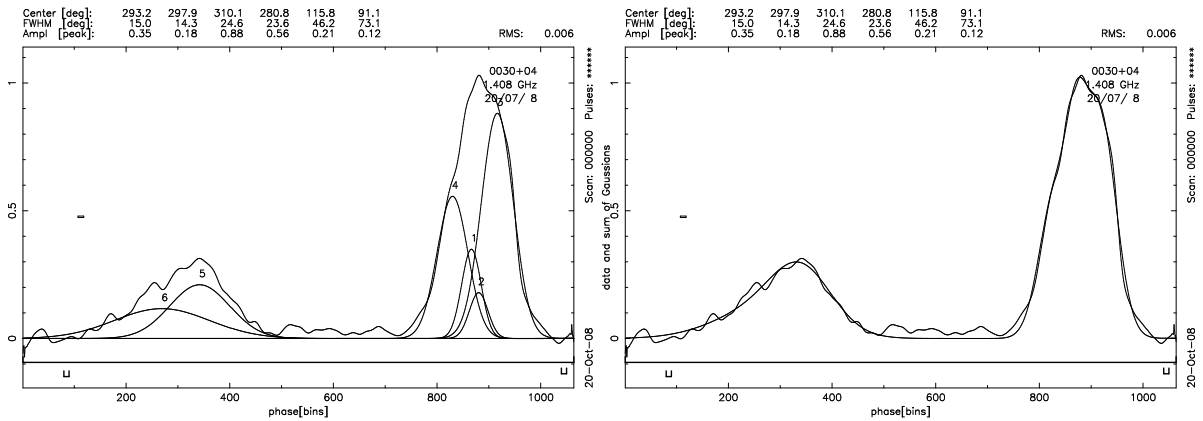
Figure 4.1: **On the left, the six Gaussian components used for the template of PSR J0030+0451 over the integrated profile. On the right, the synthetic template with the real integrated profile.**

After creating the synthetic template the TOAs of all the observations were calculated. As for all the pulsars in the current work the data of PSR J0030+0451 were calibrated in order to be improved. In addition to the rfi cleaning and the microsecond "jumps" inserted for specific days, the individual integrated profiles of each days observation (3 in each session) were added together by cross correlation in order to finally get an "aligned" TOA. After a total of eight months of observations we have six TOAs at 1.4 GHz and three at 2.7 GHz resulting in a post-fit rms of 5.7 μs. The post-fit residuals versus time are shown in Figure 4.2.

Since there were so few Effelsberg TOAs no more results could be acquired from this pulsar. By continuation of Effelsberg timing of PSR J0030+0451 and combination with the rest

---

[1]Nonlinear optimisation numerical method
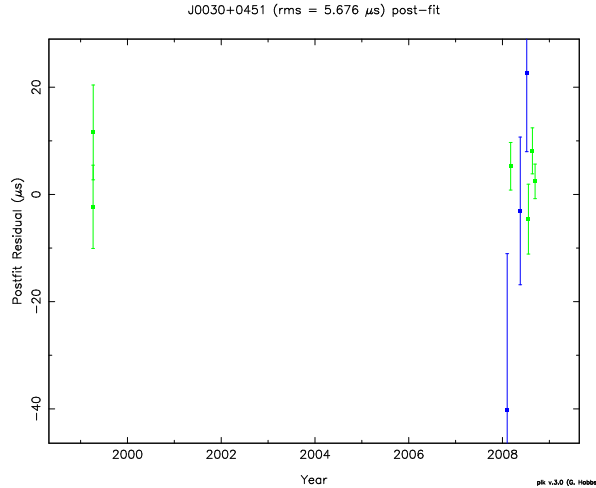
Figure 4.2: **The post-fit residuals in μs versus time in years for PSR J0030+0451, as produced by tempo2. With green are the 1.4 GHz TOAs and with blue the 2.7 GHz.**

of the EPTA telescopes, which have observed it for a longer period, we expect to reach an rms comparable to the 1 μs reported from Lommen et al. (2006). This will enable us to improve the timing solution of this pulsar and measure its astrometric and spin parameters in high accuracy. In addition, its low rms and its large angular separation from other very stable millisecond pulsars is making it an ideal candidate for the ultimate goal of the EPTA of the direct gravitational radiation detection (see Chapter 1).

4.2   PSR J0218+4232

PSR J0218+4232 is a 2.3 ms pulsar in a two day orbit around a low-mass ($\sim$0.2 M$_\odot$) white dwarf companion (Navarro et al. 1995). It was discovered in 1990 as a radio source (Dwarakanath & Shankar 1990; Hales et al. 1993) but it was not until 1993 when Lovell observations by Navarro et al. (1995) confirmed it to be a millisecond pulsar. From the dispersion measure, a lower limit (because it is lying outside the electron layer of the model) on the distance of 5.7 kpc for this luminous pulsar ($L_{400} > 2700$ mJy kpc^2) was derived.

Verbunt et al. (1996) showed evidence of emission from PSR J0218+4232 at high energies, both at X-rays using the High Resolution Imager of ROSAT and at γ-rays using EGRET data. Kuiper et al. (1998, 2000) presented further evidence of pulsation in both energy domains using again EGRET data for the γ-ray and ROSAT for the X-ray. The X-ray pulsations were found with a period identical to the radio pulse period. Recently, the γ-ray detection was confirmed by the Fermi-LAT, making it the first ms pulsar detected by the new γ-ray telescope. The most remarkable fact for PSR J0218+4232 is that it is the only millisecond pulsar similar to the Crab pulsar with a large un-pulsed fraction ($63\% \pm 13\%$ in the ROSAT band below 2.4 kev (Kuiper et al. 1998), and $\sim 50\%$ in radio (Navarro et al. 1995)). Since there was no identification of a nebula around the pulsar the best explanation for this is that it is an aligned rotator. The latter was further supported by Stairs et al. (1999) using polarimetric radio observations who showed that the line-of-sight inclination maybe around 90 degrees with a very broad pulsar

beam. This leads to the intriguing conclusion that with the timing proper accuracy, a Shapiro delay measurement can be acquired for this binary system.

PSR J0218+4232 has been observed with Effelsberg radiotelescope regularly at at least two frequencies from 1999. Its low S/N ratio and its unusually broad profile (Figure 4.3) making it very difficult to measure its TOAs with high precision, especially at 2.7 GHz. For that reason instead of the normal integration time used for the rest of the millisecond pulsars in our schedule (three scans of $\sim$ 5-10 min each) we increased the integration time of each scan for this pulsar in order to increase the S/N and the timing accuracy (equation 2.14). After calibrating the data of this pulsar (removing rfi and adding "jumps") and updating the solar system ephemeris to DE405, its separate scans per day were added ("aligned") in order to increase the S/N ratio. This procedure improved the timing accuracy even further, because of many previous non-detections that could be observed after the alignment, giving us finally 137 TOAs.

The template used in Effelsberg until now was created some years ago. Since this pulsar cannot provide in short timescale a high S/N sum of integrated profiles we decided to construct another Gaussian synthetic template at 1.4 GHz (Figure 4.3) . The new template is much better and detailed than the previous one increasing our timing accuracy by an order of magnitude, reaching for the first time a post-fit rms of 9.6 μs. In the future we will be able to make even more accurate templates (distinguish more features of the complicated profile) at more than one frequencies.
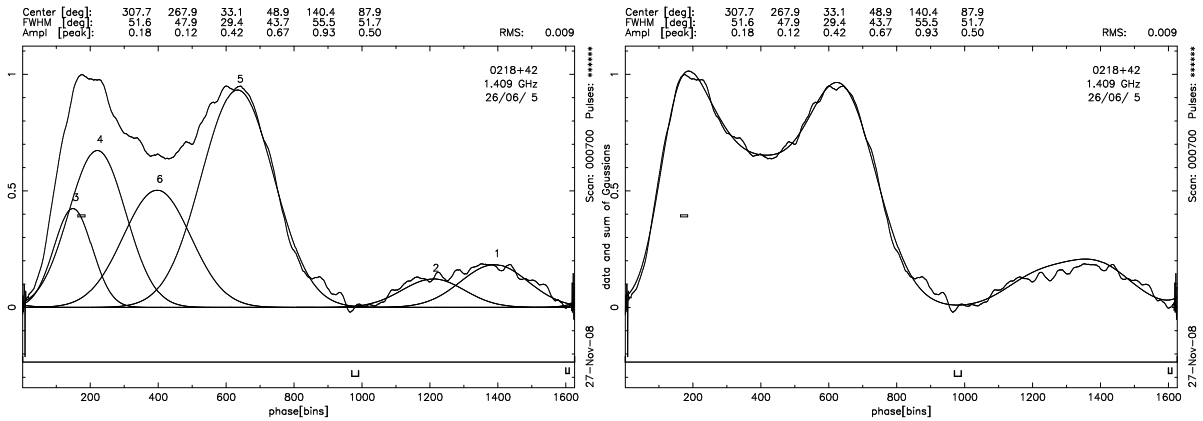
Figure 4.3: **On the left, the six Gaussian components used for the template of PSR J0218+4232 over the integrated profile. On the right, the synthetic template with the real integrated profile.**

By fitting our nine years of TOAs, mostly at 1.4 GHz and few at 800 MHz we get get the post-fit residuals versus time as shown in Figure 4.4. All the TOAs were analysed by tempo2 using the ELL1 (Lange et al. 2001) binary model for small eccentricity binary systems. In Table 4.2 all the improved astrometric, spin and binary parameters produced by tempo2 are presented. The uncertainties of the TOAs are scaled by a factor of 1.5 and 1.6 at 1400 and 800 MHz respectively, to achieve a uniform reduced $\chi^2 \approx 1$. As shown, we measure most of these parameters with high accuracy, deriving also a significant total proper motion of $\mu = 5.6 \pm 0.3$ mas/yr.

The final part of the preliminary analysis made in the current work for PSR J0218+4232 was to search for signatures of a Shapiro delay caused by the gravitational field of the companion
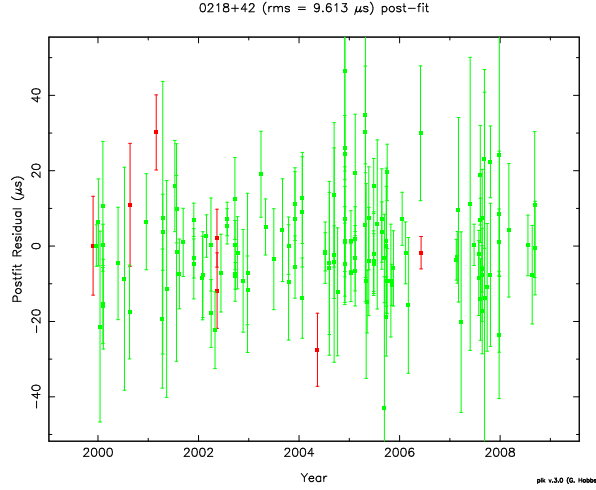
Figure 4.4: **The post-fit residuals in** μs **versus time in years for PSR J0218+4232, as produced by tempo2.
With green are the 1.4 GHz TOAs and with red the 800 MHz.**

Table 4.2: **The spin, astrometric and binary parameters of PSR J0218**+**4232.**

Parameters	Effelsberg
α (J2000)	02:18:06.35291(18)
δ (J2000)	+42:32:17.413(4)
ν (s^{-1})	430.46105900638(3)
$\dot{\nu}$ (s^{-2})	-1.434071$\times 10^{-14}$(16)
PEPOCH (MJD)	51400.000128011
POSEPOCH (MJD)	51400.000128011
DMEPOCH (MJD)	51400
DM (cm^{-3} pc)	37(9)
μ_α (mas/yr)	5.1(3)
μ_δ (mas/yr)	-2.3(7)
P$_b$ (d)	2.0288461157(5)
x (lt-s)	1.9844369(13)
T$_{ASC}$ (MJD)	51398.5704136(5)
η	0.0000033(14)
κ	0.0000032(13)
No of TOAs	137
Post-fit rms (μs)	9.6

Figures in parentheses are the nominal 1σ TEMPO2 uncertainties in the list-significant digits quoted

WD in our data (equation 4.1). For small eccentricity pulsars we have;

$$\Delta_{SB} = -2r \ln[1 - s \sin \Phi], \qquad (4.1)$$

where $r = T_\odot m_c$ and $s = \sin i$ are are the two post-keplerian parameters range and shape
and Φ is the orbital phase measured from the ascending node (Lange et al. 2001). A Shapiro
delay is only measurable in binary systems where the orbit is seen nearly edge-on ($i \sim 90^o$),

which is probably the case here (Stairs et al. 1999). By setting the value of the companion mass to $m_c = 0.2\,\mathrm{M_\odot}$ (Navarro et al. 1995) and using the mass function we measure, $f_p = (m_c \sin i)^3/(m_p + m_c)^2 = (203843.3 \pm 0.4) \times 10^{-8}$, were i is the inclination angle of the system, we try to constrain i by checking the minimum value of χ^2. As seen in Figure 4.5 we cannot successfully constrain the inclination angle. By knowing that the maximum of the effect would be expected for superior conjuction ($\Phi = \pi/2$) when the pulsar is behind the companion, by setting $m_c = 0.2\,\mathrm{M_\odot}$ and the inclination angle at $\sin i \approx 0.9$ we would expect that the effect would have a magnitude of $\sim 0.3\,\mu$s in our post-fit residuals. It is clear that with the current accuracy we cannot detect the Shapiro delay.

In the future, improvements of our timing solution, mostly resulting from the combination of Effelsberg with the rest of the EPTA TOAs, could increase our timing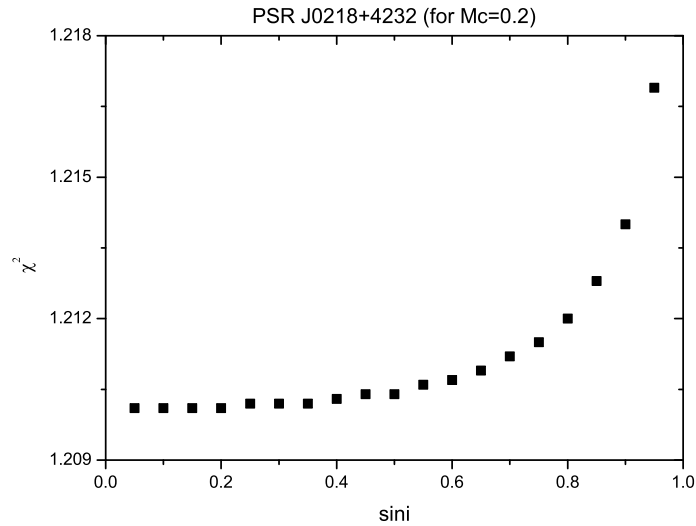 accuracy enough to measure the Shapiro delay. This would enable us to measure the two PK parameters r and s and significantly constrain the masses and the inclination angle of the binary system.

Figure 4.5: **The curve represents the χ^2 values for fixed $m_c = 0.2\,\mathrm{M_\odot}$, where no constrains can be derived for the inclination angle i.**

4.3 PSR J0613−0200

PSR J0613−0200 is a millisecond pulsar with 3.06 ms period in a roughly circular orbit with period of 1.20 days around a low mass ($\sim 0.13\,\mathrm{M_\odot}$) companion (possibly a white dwarf). It was discovered in 1994 in a survey of the Southern Hemisphere with the Parkes 64m radio telescope by Lorimer et al. (1995b) providing a DM distance of 2 kpc by using the Taylor & Cordes (1993) electron distribution model. Toscano et al. (1999b) report for the first time measurements of the proper motion for the pulsar after 5 years of timing with Parkes.

Hotan et al. (2006) give the latest high precision timing results for that pulsar using mostly three years data at 685 MHz with the Caltech Parkes Swinburne Recorder coherent de-dispersion

system at Parkes. One peculiarity of PSR J0613−0200 is that at low frequencies its profile is changing by evolving a narrow spike. This feature makes higher precision timing possible at low frequencies and this is why they achieve an rms of 2.1 μs. After combination with the 1.4 GHz data they measure for the first time a parallax of 2.1 ± 6 mas deriving a distance of 480 pc, three times smaller than the DM one from the Galactic electron density distribution model NE2001 (Cordes & Lazio 2002). They also confirm the proper motion value of Toscano et al. (1999b) in right ascension while the difference of the same value in declination is attributed in the different solar system ephemeris. Finally by managing to constrain the inclination angle of the system between 59-68 degrees they constrain the mass of the companion to 0.13-0.15 M$_\odot$, showing that it is one of the most asymmetric systems, suitable for tests of general relativity.

PSR J0613−0200 has been observed with the Effelsberg radiotelescope regularly at 1.4 GHz from 1996 and in at least two frequencies from 1999. Unfortunately the low frequency data at 800 MHz were not good enough to use in our timing analysis, which means that we actually have only two years of multi-frequency data (1.4 and 2.7 GHz). Although it has a broad complicated profile (Figure 4.6, taken from the European Pulsar Network (EPN[2])) it is strong enough, enabling us to perform high precision timing analysis. After the usual calibration of the data and after updating the solar system ephemeris to DE405, we added the separate scans per day in order to increase more the S/N ratio. This procedure increased our timing accuracy, providing finally 217 TOAs with an rms of 2.7 μs.
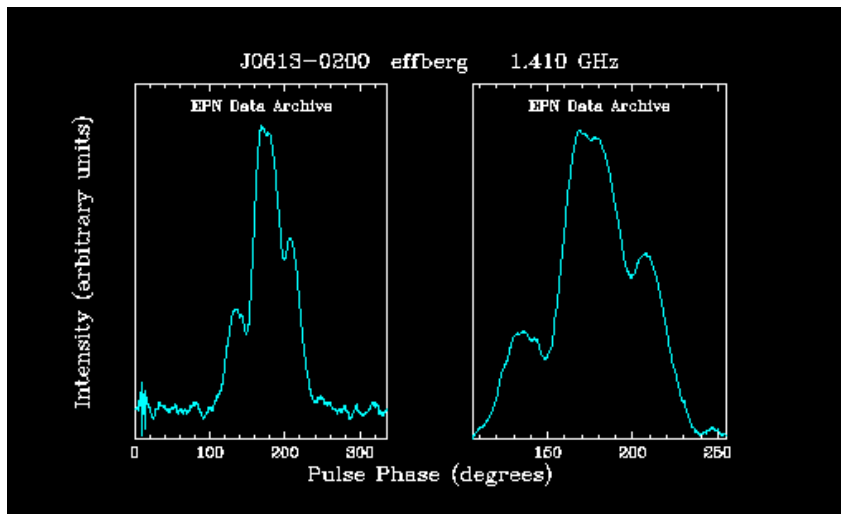
Figure 4.6: **The integrated profile of PSR J0613−0200 at 1.4 GHz taken from the EPN.**

By fitting nine years of TOAs, mostly 1.4 GHz and less 2.7 GHz we get get the post-fit residuals versus time as shown in Figure 4.7. All the TOAs were analysed by tempo2 using the ELL1 (Lange et al. 2001) binary model for small eccentricity binary systems. In Table 4.3 all the improved astrometric, spin and binary parameters produced by tempo2 are presented. The uncertainties of the TOAs are scaled by a factor of 1.9 and 3.5 at 1.4 and 2.7 GHz respectively, to achieve a uniform reduced $\chi^2 \approx 1$. As shown, we measure all the parameters with high accuracy. When comparing our results with the previously published ones we see that they

---

[2]http://www.mpifr-bonn.mpg.de/div/pulsar/data/browser.html

are totally consistent with Hotan et al. (2006). This includes also our proper motion in right ascension and declination, which confirms that the difference in the declination to Toscano et al. (1999b) is the results of their use of the DE200 solar system ephemeris. Along with the other binary parameters we derive a value for the eccentricity of $e = (4.9 \pm 0.4) \times 10^{-6}$ which is also consistent with Hotan et al. (2006), and it is one of the smallest eccentricities ever measured. We did not derive a timing parallax but for the first time we have a significant measurement of the change of the projected semi-major axis of the orbit $\dot{x} = (1.9 \pm 0.3) \times 10^{-14}\,\mathrm{s\,s^{-1}}$. This phenomenon can result from gravitational wave damping that shrinks the orbit, or from proper motion effects or other various effects mentioned in Chapter 3. If we could also measure the change in the orbital period ($\dot{P}_b$) we could check if the two values follow the third law of Kepler confirming that they emerge from loses of gravitational radiation.
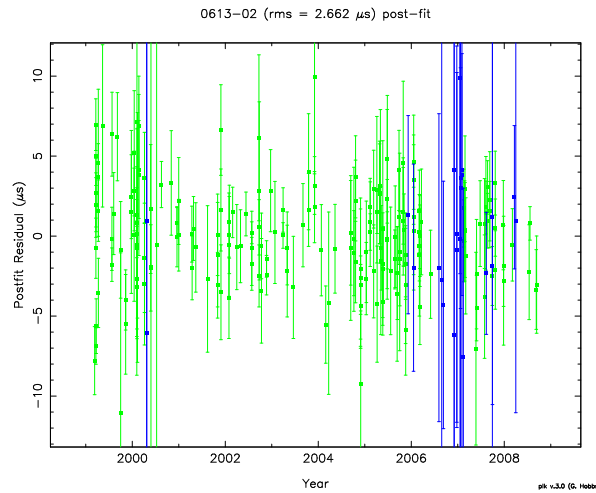
Figure 4.7: **The post-fit residuals in μs versus time in years for PSR J0613−0200, as produced by tempo2. With green are the 1.4 GHz TOAs and with blue the 2.7 GHz.**

With the Effelsberg data set we get only an 1σ measurement of the $\dot{P}_b$. This possibly means that adding all the EPTA TOAs could result in a 3σ improvement, since the $\dot{P}_b$ uncertainty scales with time, $\sim t^{-2.5}$, (Lorimer & Kramer 2005).By knowing this value, using the Hotan et al. (2006) mass and inclination estimations and by taking advantage of the asymmetry of the system, we could test GR and set stringent limits for alternative theories of gravity like in the case of PSR J1012+5307 (Chapter 3). In addition, by investigating all the contributions of the $\dot{x}$ we could measure orientation parameters like the position angle of the ascending node. Last but not least with all EPTA datasets combined we can possibly reach or even improve the rms of Hotan et al. (2006). This means that we can have another millisecond pulsar close to the nanosecond regime, a perfect candidate for a gravitational wave detection with a PTA.

4.4 PSR J0621+1002

PSR J0621+1002 is a 28.9 ms pulsar in an 8.32 day orbit with eccentricity $\sim$0.0025 around a massive ($\sim$0.97 $M_\odot$ Splaver et al. (2002)) white dwarf companion. It was discovered in data taken on 1994 (Camilo et al. 1996) by a survey using the Arecibo 305m radio telescope at

Table 4.3: **The spin, astrometric and binary parameters of PSR J0613−0200.**

Parameters	Effelsberg
α (J2000)	06:13:43.974506(13)
δ (J2000)	-02:00:47.1200(5)
ν (s^{-1})	326.600562354928(3)
$\dot{\nu}$ (s^{-2})	-1.022982×10^{-15}(18)
PEPOCH (MJD)	51250.000125685
POSEPOCH (MJD)	51250.000125685
DMEPOCH (MJD)	51250
DM (cm^{-3} pc)	38.7708(12)
μ_α (mas/yr)	1.81(4)
μ_δ (mas/yr)	-10.29(10)
P$_b$ (d)	1.19851257501(6)
x (lt-s)	1.0914428(3)
T$_{ASC}$ (MJD)	51250.10930007(9)
η	0.0000037(5)
κ	0.0000032(5)
No of TOAs	217
Post-fit rms (μs)	2.7

Figures in parentheses are the nominal 1σ TEMPO2 uncertainties in the list-significant digits quoted

430 MHz. It lies near the galactic plane and close to the anticenter direction (l=200°, b=-2°). Its distance estimation from its DM= 36.6 cm^{-3}pc with NE2001 (Cordes & Lazio 2002) is d=1.35 kpc.

PSR J0621+1002 is the prototype of the class of "intermediate mass" binary, mildly spun-up pulsars whose companions are C-O or O-Ne-Mg white dwarfs. The fist effort for precise timing was made by Splaver et al. (2002) with 6 years of data from the Green Bank,Jodrell Bank and Arecibo radio telescopes, reaching an rms of 3.2 μs. Initially, they presented estimates of the characteristic age ($\tau = 1.1 \times 10^{10}$ yr) and the surface magnetic field strength ($B_0 = 1.2 \times 10^9$ G) by calculating the intrinsic period derivative of the pulsar. They detected the relativistic advance of the periastron which is $\dot{\omega} = 0.0116 \pm 0.0008$ yr^{-1} which implies a total mass of $m_c + m_p = 2.81 \pm 0.3$ M$_\odot$. A Shapiro delay was not detected in this system, ruling out high inclination angles. The estimate for the pulsar mass was $m_p = 1.70 \pm 0.6$ M$_\odot$ (95% confidence).

The mass and precession of the periastron measurement uncertainties were improved by Nice et al. (2008), when they used in addition to the previous, nine more consecutive days of observations of the source with Arecibo. Thus, the latest values acquired are $\dot{\omega} = 0.0105 \pm 0.0002$ yr^{-1}, $m_p + m_c = 2.37 \pm 0.12$ M$_\odot$ and $m_p = 1.7^{+0.10}_{-0.17}$ M$_\odot$.

PSR J0621+1002 has been observed regularly with Effelsberg at 1.4 GHz since 1997 and in at least two frequencies from 1999 (first 800 MHz and from 2006 2.7 GHz). Its profile is consisted from narrow features (peaks) which makes it easier to time in high accuracy (Figure 4.8, taken from the EPN). After the usual calibration of the data and the updated solar system ephemeris we were still getting a somehow unexplained high post-fit rms value at 1.4 GHz. This was of course creating problems in the overall fit. Usually, the post-fit is not good enough either because of some specific points (if they are affected by rfi, or if the S/N ratio of the specific profile is too low) either because of some model parameters which are not estimated correctly

(or even not used at all). In the specific case though, the reason was neither of the previous. When we "aligned" the individual scans the solution we were getting at 1.4 GHz worsened by an order of magnitude. This could only mean that there were either profile changes of the pulsar (no evidence of that) or drifting behaviour (phase shifts) of the profile during the observation session. After checking thoroughly, we detected that the latter was happening until 2002, confirming that possibly until that period we were using a not well defined parameter file for observing the specific source. Specifically, that measured drift is ~ 0.08 ns from pulse to pulse ($\sim 10\,\mu$s per minute). When fitting only the TOAs after 2002 the timing solution was improving a lot. Thus, by using only these data sets we obtain a post-fit rms of 6.8 μs from 94 TOAs.
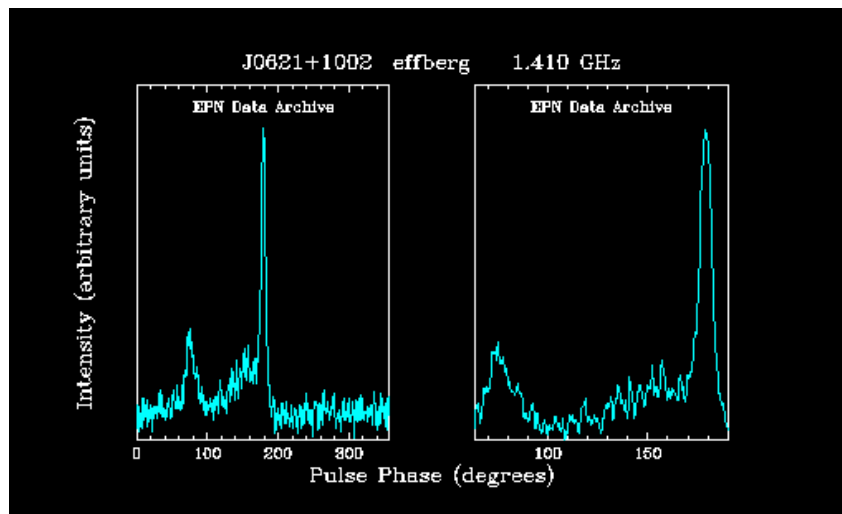
Figure 4.8: **The integrated profile of PSR J0621+1002 at 1.4 GHz taken from the EPN.**

By fitting those six years of TOAs, consisting of 3 frequencies, we get the post-fit residuals versus time presented in Figure 4.9. All the toas were analysed by tempo2 using the DD (Damour & Deruelle 1985) theory-independent relativistic model. In Table 4.4 all the improved astrometric, spin and binary parameters produced by tempo2 are presented. The uncertainties of the TOAs are scaled by a factor of 1.6 at all frequencies to achieve a uniform reduced $\chi^2 \approx 1$. As presented, we measure most of the parameters with high accuracy. When comparing them with Splaver et al. (2002) everything develops smoothly, even the periastron rate of change, in some cases even at the same accuracy, apart from the proper motion in declination. We get also a 2σ detection of the DM variation of PSR J0621+1002. We know that for most of the pulsars the DM can be accurately characterised as a single number that holds steady over years of observation. This however, is not true for PSR J0621+1002 (Splaver et al. 2002) and we get a measurement of this variation ($\dot{DM} = 0.006 \pm 0.003\,\text{cm}^{-3}$ pc yr^{-1}).

Relying only on the Effelsberg TOAs, especially when we have only very few multi-frequency observations, a big improvement in our timing solution cannot be expected. By using the long-term multi-frequency EPTA datasets we could immediately look for a precise value of the DM variation. Keeping continuous track of DM will give us high precision timing. In addition, combination of all datasets it will make PSR J0621+1002 a candidate source for the EPTA effort in detecting gravitational waves, since it will push our timing accuracy close to 1 μs. Splaver
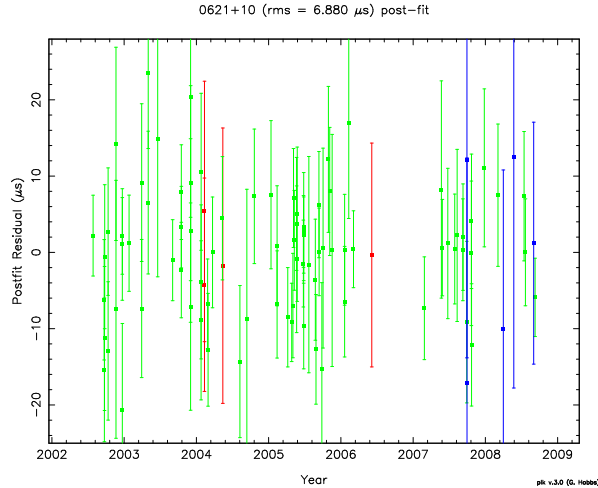
Figure 4.9: The post-fit residuals in μs versus time in years for PSR J0621+1002, as produced by tempo2. With green are the 1.4 GHz TOAs, with red the 800 MHz and with blue the 2.7 GHz.

Table 4.4: The spin, astrometric and binary parameters of PSR J0621+1002.

Parameters	Effelsberg
α (J2000)	06:21:22.11174(18)
δ (J2000)	+10:02:38.721(12)
ν (s^{-1})	34.657406641377(8)
$\dot{\nu}$ (s^{-2})	-5.682$\times 10^{-17}$(3)
PEPOCH (MJD)	50944.000120941
POSEPOCH (MJD)	50944.000120941
DMEPOCH (MJD)	50944
DM (cm^{-3}pc)	36.45(3)
$\dot{\text{DM}}$ (cm^{-3} pc yr^{-1})	0.006(3)
μ_α (mas/yr)	3.6(4)
μ_δ (mas/yr)	2.0(17)
P$_b$ (d)	8.3186823(20)
T$_0$ (MJD)	50944.7567(6)
x (lt-s)	12.0320722(13)
ω (deg)	188.81(3)
e	0.00245757(20)
$\dot{\omega}$ (deg/yr)	0.013(4)
No of TOAs	94
Post-fit rms (μs)	6.8

Figures in parentheses are the nominal 1σ TEMPO2 uncertainties in the list-significant digits quoted

et al. (2002) obtained limits for the change of the orbital period for this pulsar. If we achieve a significant detection of $\dot{P}_b$ (possible if we improve our combined EPTA timing solution) we will have one of the few NS-WD binary systems with two post-Keplerian parameters measured. Thus, the opportunity arises in testing general relativity in yet another system.

4.5   PSR J0751+1807

PSR J0751+1807 is a 3.48 ms pulsar in a circular 6.32 hour orbit with a light white dwarf companion (Bassa et al. 2006) at a distance of 1.15 kpc (Nice et al. 2005) derived from DM using the NE2001 galactic electron density model (Cordes & Lazio 2002). It was first detected in an EGRET source error box, in September 1993 (Lundgren et al. 1995b) using the radio telescope at Arecibo. Its mass function, small orbit, low eccentricity and large timing age implied that the WD companion is most likely $0.12 < m_c < 0.6 \, \mathrm{M_\odot}$. This WD companion was optically identified by Bassa et al. (2006) with the Keck telescope. It was found that it has the reddest colours of all known millisecond pulsar companions and white dwarfs. The colours indicate that it has a very low (ultra-cool) temperature of Teff$\sim 3500 - 4300$ K. It has a pure helium atmosphere with perhaps some hydrogen, something that is inconsistent with evolutionary models, from which one would expect a pure hydrogen atmosphere.

It was also detected in X-rays with XMM-Newton and showed pulsations, in particular a single pulse (Webb et al. 2004). From spectral analysis it was found that its spectrum is fitted best by a power law model.

Nice et al. (2005) did the most complete precision timing analysis (rms of $7 \, \mu$s) of the PSR J0751+1807 binary system with Arecibo and Effelsberg data and managed to detect the decay of its orbit due to emission of gravitational radiation. This was the first detection of the relativistic orbital decay of a low mass circular binary pulsar system with a $\dot{P}_b = (-6.4 \pm 0.9) \times 10^{-14} \, \mathrm{s \, s^{-1}}$. Combined with the measurement of a Shapiro delay they were implying a mass of $2.1 \pm 0.2 \, \mathrm{M_\odot}$, the largest ever measured for a pulsar. After measuring the three PK parameters (r, s and $\dot{P}_b$) they checked for violations of the SEP by obtaining tight limits of the coupling strength of the pulsar to the scalar field, according to scalar-tensor theories (Damour & Esposito-Farese 1996). Nice et al. (2008) improved the previous measurements giving $\dot{P}_b = (-3.1 \pm 0.5) \times 10^{-14} \, \mathrm{s \, s^{-1}}$ and $m_p = 1.26 \pm 0.28 \, \mathrm{M_\odot}$ (95% confidence).

PSR J0751+1807 has been regularly observed with Effelsberg at 1.4 GHz since 1997 and in at least two frequencies from 1999 (first 800 MHz and from 2006 2.7 GHz). Its a very strong pulsar with a profile consisting of 2 narrow components, making it easy to time in high accuracy (Figure 4.10, taken from the EPN). After the usual calibration of the data and the updated solar system ephemeris which improved our post-fit rms by three times we "aligned" the individual scans. Unfortunately, a small decrease in the accuracy was observed, possibly because of small phase shifts during observations, caused by a not-well fitting older parameter file, however big enough, to influence the "individual" TOAs (much smaller than the case of PSR J0621+1002). This means that we used our in total 944 "individual" integrated profiles ($\sim$5 minutes each), TOAs, to derive an rms of $4.4 \, \mu$s, much better than that achieved from Nice et al. (2005).

By fitting all these 12 years of multi-frequency TOAs we get the post-fit residuals versus time presented in Figure 4.11. All the toas were analysed by tempo2 using the ELL1 (Lange et al. 2001) binary model. In Table 4.5 all the improved astrometric, spin and binary parameters produced by tempo2 are presented. The uncertainties of the TOAs are scaled by a factor of 1.8 at all frequencies to achieve a uniform reduced $\chi^2 \approx 1$. As presented, we measure with high accuracy all the fitted parameters. Everything is consistent with the values of Nice et al. (2005) and almost at the same uncertainty level. When checking for the Shapiro delay, as described in section 4.2, we detect for our measured mass function, $f_p = (m_c \sin i)^3/(m_p + m_c)^2 = (96739.8299 \pm 0.1679) \times 10^{-8}$ and by setting $m_c = 0.19 \, \mathrm{M_\odot}$, a minimum of the χ^2 when the $\sin i$ was getting the value 0.9, which implies an inclination angle of $\sim 65^o$, consistent with the previously estimated value. In addition, we derive a value for the orbital period variation
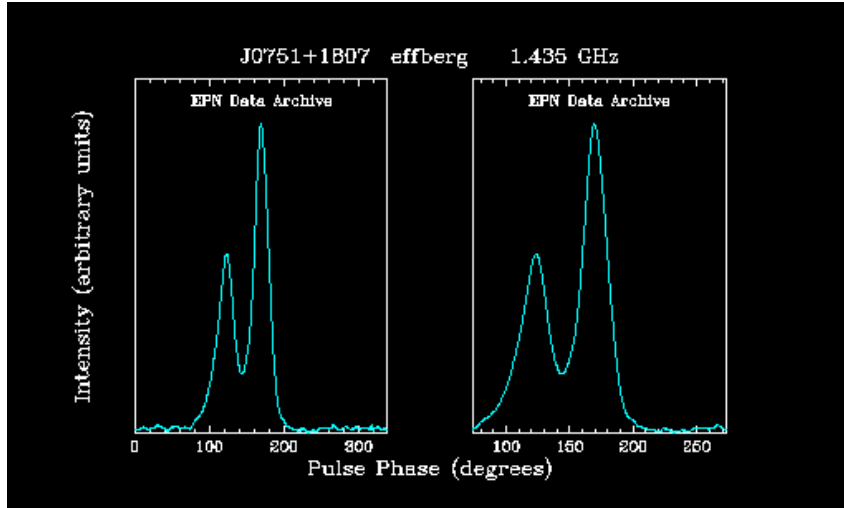
Figure 4.10: **The integrated profile of PSR J0751+1807 at 1.4 GHz taken from the EPN.**

($\dot{P_b} = (-2.9 \pm 1.3) \times 10^{-14}$ s s^{-1}) consistent with Nice et al. (2008) but with higher uncertainty. Last but not least, we get a significant detection of the variation of the projected semi-major axis of $\dot{x} = (-1.3 \pm 0.3) \times 10^{-14}$ s s^{-1}.
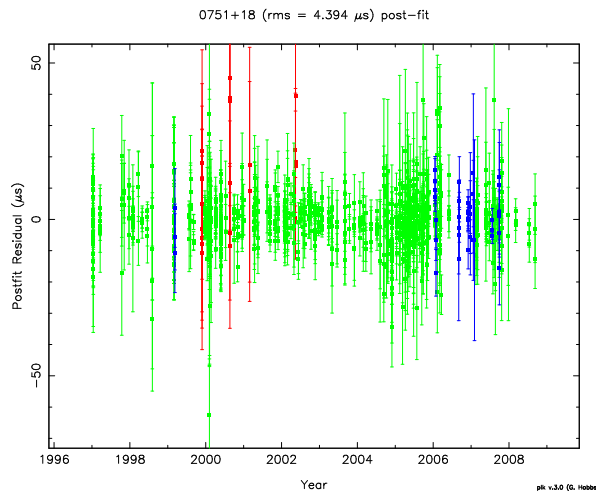
Figure 4.11: **The post-fit residuals in μs versus time in years for PSR J0751+1807, as produced by tempo2. With green are the 1.4 GHz TOAs, with red the 800 MHz and with blue the 2.7 GHz.**

Starting from the latter, a combination of this value, with an improved future value of $\dot{P_b}$ (by combination of the EPTA with the Arecibo and Effelsberg data) we could first constrain the orientation of the binary system and secondly provide the exact contribution of gravitational radiation dumping to $\dot{x}$. In addition, by better constraining $\dot{\omega}$ a better mass estimation of the two bodies could be achieved. This can provide important information about the evolution of this extremely short orbital period system. Finally, as in most of the pulsars analysed in the current

Table 4.5: **The spin, astrometric and binary parameters of PSR J0751+1802.**

Parameters	Effelsberg
α (J2000)	07:51:09.15714(4)
δ (J2000)	+18:07:38.609(3)
ν (s^{-1})	287.4578541850310(14)
$\dot{\nu}$ (s^{-2})	-6.43485$\times 10^{-16}$(13)
PEPOCH (MJD)	51584.000130864
POSEPOCH (MJD)	51584.000130864
DMEPOCH (MJD)	51584
DM (cm^{-3} pc)	30.2439(7)
μ_α (mas/yr)	-2.56(15)
μ_δ (mas/yr)	-12.1(8)
P$_b$ (d)	0.263144270751(7)
x (lt-s)	0.3966159(3)
T$_{ASC}$ (MJD)	51584.17442202(4)
η	0.0000034(11)
κ	-6.1E-8(1200)
No of TOAs	944
Post-fit rms (μs)	4.4

Figures in parentheses are the nominal 1σ TEMPO2 uncertainties in the list-significant digits quoted

work, PSR J0751+1807 is very close to the ns accuracy regime, being a candidate for the EPTA effort in direct detections of gravitational waves.
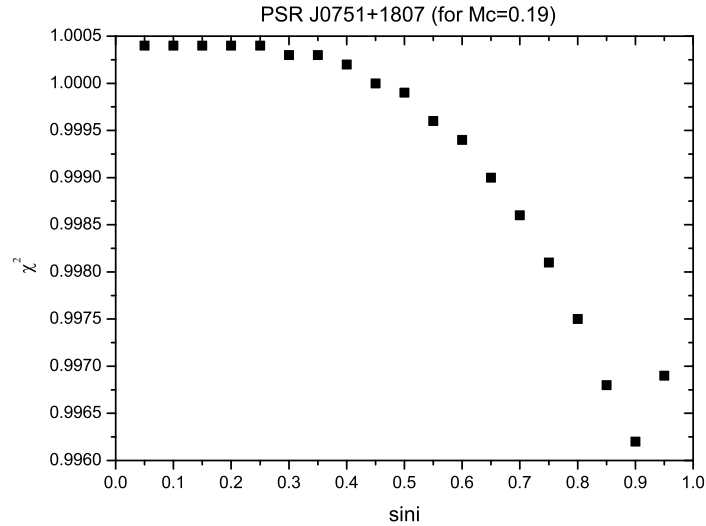
Figure 4.12: **The curve represents the χ^2 values for fixed $m_c = 0.19\,M_\odot$, where the most probable (minimum χ^2) inclination value is for $\sin i$=0.9.**

4.6   PSR J1022+1001

PSR J1022+1001 is a 16.5 ms pulsar in a 7.8 day orbit with eccentricity 10^{-4} with a heavy WD (Hotan et al. 2006). It was discovered in data taken on 1994 (Camilo et al. 1996) by a survey using the Arecibo radio telescope at 430 MHz. It is located in the ecliptic (longitude λ=153.17, latitude β=-0.06) but well away from the Galactic plane (l=232°, b=+51°). Soon after its discovery it also became part of the Effelsberg timing program. Kramer et al. (1999b) with the use of Effelsberg, Arecibo, Jodrell Bank and Green Bank data, presented that the integrated profile of PSR J1022+1001, specifically parts of it, is changing, a phenomenon appearing mostly in slow pulsars. They presented evidence that this profile changes are not due to instrumental or interstellar effects but intrinsic to the pulsar. In addition, they showed that the profile changes affect the timing precision and introduced a new method of determining pulse times of arrival. With the use of it they measured the proper motion in ecliptic longitude to be -17$\pm$ 2 mas/yr.

Hotan et al. (2004) managed to obtain a much more precise timing solution for PSR J1022+1001 with the Parkes radio telescope. From a mass function measurement they gave an estimation of the companion mass (for a 1.35 $M_\odot$ pulsar) and from their initial parallax measurement they find a distance of $d = 300$ pc to the object, much smaller than the 600 pc derived from the model of Taylor & Cordes (1993). The change of the projected semi-major axis, caused by proper motion changes of our line of sight to the plane of the orbit, $\dot{x} = 0.8 \pm 0.3 \mu$s/yr was also measured. The most precise (1.5 μs) and latest timing solution for this pulsar was presented by Hotan et al. (2006), achieved from 3 years of Parkes observations. The value of the proper motion in ecliptic longitude (Kramer et al. 1999b) is confirmed and a lower limit of 7 mas/yr is calculated for the composite proper motion. The parallax now is given as $\pi = 2.5 \pm 0.8$ mas resulting in a distance of 400 pc, which is consistent with the NE2001 distance of 405 pc. Finally, from a Shapiro delay measurement they obtained an estimate of the inclination angle of the system ($41^o < i < 53^o$).

PSR J1022+1001 has been observed regularly with Effelsberg at 1.4 GHz since 1997 and in at least two frequencies from 1999 (first 800 MHz and from 2006 2.7 GHz). Its a strong pulsar with a profile consisting of double peaked narrow component, making it easy to time in high accuracy (Figure 4.13, taken from the EPN), however, as mentioned before, it shows profile changes that affect the timing accuracy. After the usual calibration of the data and the updated solar system ephemeris which improved our post-fit rms by more than three times we "aligned" the individual scans of every session. Despite the mode changing effect we had an improvement from the procedure, giving evidence that the changes are not so extreme on short-timescales. We finally used a total of 166 "aligned" TOAs, to derive an rms of 3.6 μs.

By fitting nine years of multi-frequency TOAs we get the post-fit residuals versus time presented in Figure 4.14. All the toas were analysed by tempo2 using the DD (Damour & Deruelle 1985) binary model. In Table 4.6 all the improved astrometric, spin and binary parameters produced by tempo2 are presented. The uncertainties of the TOAs are scaled by a factor of 1.8 at 1.4 GHz and 3.4 at 800 and 2700 MHz to achieve a uniform reduced $\chi^2 \approx 1$. As presented, we measure with high accuracy all the fitted parameters apart from the proper motion in declination, because the pulsar lies close to the ecliptic plane. When comparing our results with the values from Hotan et al. (2006) everything is consistent and almost at the same uncertainty level or better. Apart from the rest of the astrometric parameters a more precise value of the timing parallax was also obtained, $\pi = 2.3 \pm 0.5$ mas providing a distance of $d = 442 \pm 109$ pc, consistent with the published value. In addition, a significant variation of the projected semi-major axis of $\dot{x} = (1.5 \pm 0.4) \times 10^{-14}$ s s^{-1} was detected with an improved uncertainty (almost a 3σ
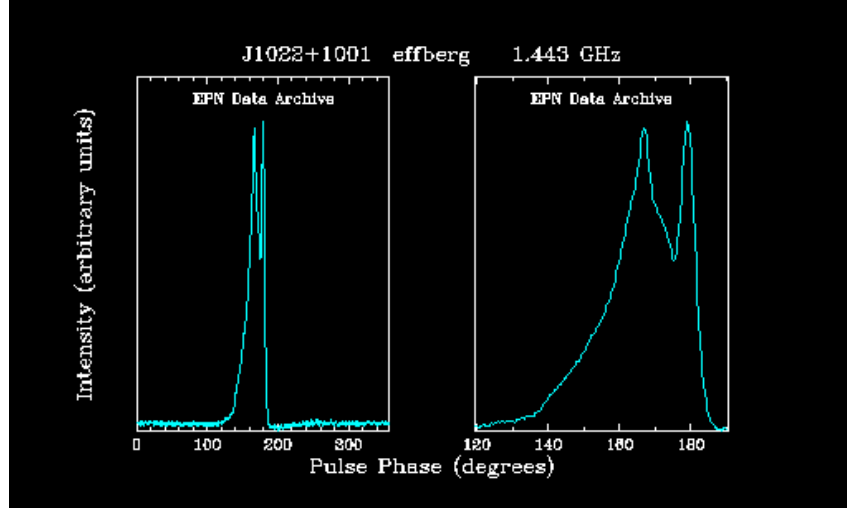
Figure 4.13: **The integrated profile of PSR J1022+1001 at 1.4 GHz taken from the EPN.**

detection). This variation is probably caused by the proper motion of the system which alters our line of sight as shown in equation (4.2),

$$\dot{x} = x \cot i (-\mu_\alpha \sin \Omega + \mu_\delta \cos \Omega) \, \text{s s}^{-1}, \tag{4.2}$$

(Sandhu et al. 1997), where Ω is the position angle of the ascending node.
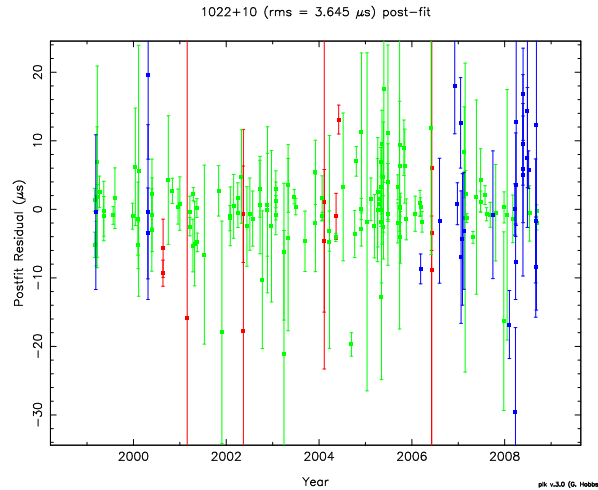
Figure 4.14: **The post-fit residuals in μs versus time in years for PSR J1022+1001, as produced by tempo2. With green are the 1.4 GHz TOAs, with red the 800 MHz and with blue the 2.7 GHz.**

In the latter equation, the proper motion in declination and the Ω are unknown. In the future, VLBI measurements of the μ_δ could lead to a calculation of the angle Ω, constraining the three dimensional orientation of the orbit on the sky. In addition, this measurement could lead to further improvement of the parallax and the distance and determination of the intrinsic $\dot{P}$. All

Table 4.6: **The spin, astrometric and binary parameters of PSR J1022+1001.**

Parameters	Effelsberg
α (J2000)	10:22:58.002(3)
δ (J2000)	+10:01:52.55(11)
ν (s^{-1})	60.7794479954291(3)
$\dot{\nu}$ (s^{-2})	-1.60106$\times 10^{-16}$(4)
PEPOCH (MJD)	52200.000140415
POSEPOCH (MJD)	52200.000140415
DMEPOCH (MJD)	52200
DM (cm^{-3} pc)	10.2547(4)
μ_{α} (mas/yr)	-17.05(7)
P$_b$ (d)	7.80513028257(15)
T$_0$ (MJD)	52190.1964(5)
x (lt-s)	16.7654138(4)
ω (deg)	97.79(3)
e	0.00009708(5)
No of TOAs	166
Post-fit rms (μs)	3.6

Figures in parentheses are the nominal 1σ TEMPO2 uncertainties in the list-significant digits quoted

the achieved measurements can of course be determined more accurately with the addition of the rest of the EPTA TOAs, i.e. $\dot{x}$. Finally, although PSR J1022+1001 has a long spin period, we time it accurately enough to include it in the EPTA sources for gravitational wave detection. An important step would be to model its profile variations in order to increase the timing accuracy, which is actually work in progress within the EPTA (Purver et al. in prep).

4.7   PSR J1024−0719

PSR J1024−0719 is a solitary pulsar with a spin period $P = 5.2$ ms, characteristic age $t \sim 4.4$ Gyr and rotational energy loss $\dot{E} \sim 5.3 \times 10^{33}$ erg/s. It was discovered in the Parkes 436 MHz survey of the southern sky (Bailes et al. 1997). Hotan et al. (2006) measure a value DM=6.49 cm^{-3}pc, which implies a distance of $d \sim 390$ pc from the Galactic distribution of free electrons NE2001 (Cordes & Lazio 2003).

Zavlin (2006) presented an analysis of the XMM-Newton observations of PSR J1024−0719 and the first firm detection of the pulsar X-ray emission. He revealed strong evidence of the presence of a thermal component in its X-ray emission, interpreted as radiation emitted from heated polar caps around magnetic poles on the neutron star surface. In addition, X-ray pulsations were identified and especially a single broad pulse per rotational period.

The most precise (1.1 μs) and latest timing solution for this pulsar was presented by Hotan et al. (2006), achieved from 3 yrs of Parkes observations. The measured composite proper motion (59± mas/yr) differ from the same measurement of Toscano et al. (1999b) (81±4 mas/yr), but is also made with much more TOAs and better rms timing residual. Finally the parallax of 1.9±0.8 mas is measured for the first time which is consistent with the Shklovskii limit (Shklovskii 1970) and constrains the distance to the system.

PSR J1024−0719 has been observed with Effelsberg from 1999. However, regular monthly

observations at 1.4 and 2.7 GHz have been performed only from 2006. This pulsars compli-cated, multicomponent mean profile contains sharp $\sim 50\,\mu s$ wide features (Figure 4.15, taken from the EPN) that allow TOAs to be precisely determined. After calibrating the data and updating the solar system ephemeris we had an improvement of more than two orders of mag-nitude. This is mostly because in the previous solution the few "jumps" that were missing were affecting the fit much more, since it was consisting of only a few data points. After aligning the individual scan of the sessions we managed to reduce the post-fit rms by a factor of three, due to the vast increase in TOAs from previous non-detections. Finally the 37 "aligned" TOAs we use are at two frequencies, producing an rms of 12.4 μs. It is worth noticing that using only the 1.4 GHz data, after fixing the DM value from the multi-frequency fit, we reach an rms of 2.7 μs.
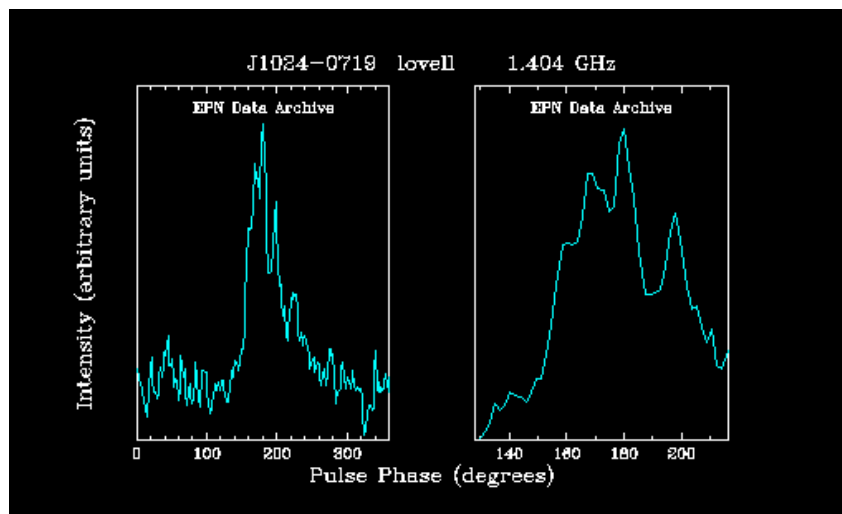
Figure 4.15: **The integrated profile of PSR J1024−0719 at 1.4 GHz taken from the EPN.**

By fitting the ∼3 years of multi-frequency TOAs we get the post-fit residuals versus time presented in Figure 4.16. All the toas were analysed by tempo2. In Table 4.7 all the improved astrometric and spin parameters produced by tempo2 are presented. The uncertainties of the TOAs are scaled by a factor of 2.5 at 1.4 GHz and 2 at 2.7 GHz to achieve the lowest possible uniform reduced χ^2. As presented, even with the few points we have we managed to measure parameters consistent with the ones from Hotan et al. (2006). The only value we do not obtain from our fit is the parallax, which was taken from the aforementioned paper.

It is quite clear that we do not have enough data points yet with Effelsberg to reach accu-racies in our measurements comparable with the published ones. However, if we combine our data set with the rest of the EPTA ones this situation can change dramatically. Proper motions and parallax, which need time coverage through the year, will be obtained easily and long-term multi-frequency TOAs will help us acquire a better DM estimation. As a result, the overall timing accuracy of PSR J1024−0719 can reach the 1 μs or get even lower, making this source a perfect candidate for the EPTA searches.
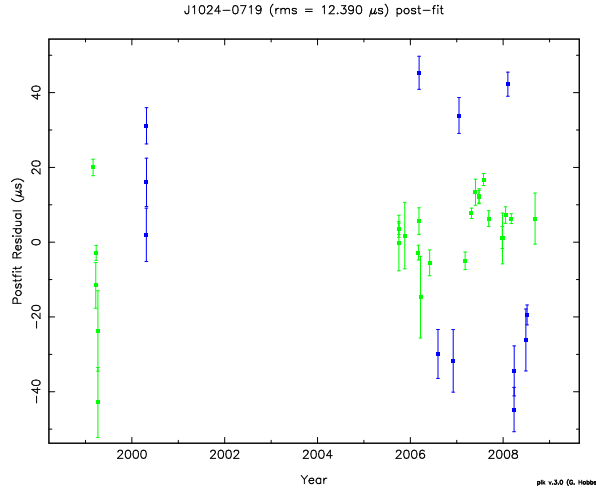
Figure 4.16: **The post-fit residuals in** μ**s versus time in years for PSR J1024−0719, as produced by tempo2. With green are the 1.4 GHz TOAs and with blue the 2.7 GHz.**

Table 4.7: **The spin and astrometric parameters of PSR J1024−0719.**

Parameters	Effelsberg
α (J2000)	10:24:38.68816(4)
δ (J2000)	-07:19:19.1664(10)
ν (s^{-1})	193.7156835687373(12)
$\dot{\nu}$ (s^{-2})	-6.9509$\times 10^{-16}$(4)
PEPOCH (MJD)	53000.000152819
POSEPOCH (MJD)	53000.000152819
DMEPOCH (MJD)	53000
DM (cm^{-3} pc)	6.425(17)
μ_α (mas/yr)	-33.8(6)
μ_δ (mas/yr)	-51(1)
π (mas)	1.9^a
No of TOAs	37
Post-fit rms (μs)	12.4

^{a}: The value was taken from Hotan et al. (2006).

Figures in parentheses are the nominal 1σ TEMPO2 uncertainties in the list-significant digits quoted

4.8 PSR J1518+4904

PSR J1518+4904 is a 40.9 ms pulsar in a 8.6 day moderately eccentric orbit (Nice et al. 1996). It was discovered in the Green Bank Northern Sky Survey (Sayer et al. 1997) and is the one of the 9 double neutron star systems known. Nice et al. (1996) by using 1.4 yrs of measured pulse arrival times derived high-precision parameters for the pulsar and the system. Among those they report an upper limit for the $\dot{P} < 4 \times 10^{-20}$, which gives a lower limit for the characteristic age $\tau > 1.6 \times 10^{10}$ yrs. Of significance is also the measurement of the precession of the orbit of $\dot{\omega} = 0.0111 \pm 0.0002\,\mathrm{yr}^{-1}$, which provides a total system mass of 2.62±0.07 M$_\odot$. Finally from

the derived distance of 700 pc and an upper limit for the proper motion of 30 mas/yr they obtain an upper limit for the space velocity of 100 km/s.

Janssen et al (2008) with 10 years of timing data by the European Pulsar Timing Array network using Westerbork, Jodrell Bank, Effelsberg and Nançay radiotelescopes at 5 different frequencies added to the original GBT data, presents the most accurate timing analysis for the NS-NS system up to date (6 μs rms). They describe the techniques of using data from multiple telescopes for pulsar timing and they clearly show the advantages (e.g. longer time span and multiple frequencies). They report a significant measurement of the proper motion of the system of μ_α=-0.67(4) and μ_δ=-8.53(4) mas/yr. This provides the total proper motion of μ=8.55(7) mas/yr which in combination with the DM distance of 625 pc corresponds to a transverse velocity of υ_t=25(4) km/s. Equally important is the precise measurement of the periastron advance of the orbit of $\dot{\omega}$=0.0113725(19) deg/yr which results in, when compared with the mass function, the most precise value of the total mass of the system of 2.7183(7) $M_\odot$. Finally by also combining the absence of the Shapiro delay detection, they provide an upper limit for the inclination angle of 47 degrees.

The work of Janssen et al. (2008) is one of the first examples of the capabilities of the EPTA. Our main purpose is to improve the Effelsberg datasets of PSR J1518+4909 for future uses, especially the new 2.7 GHz ones (that were not used in Janssen et al. (2008)). In the aforementioned work only a part of the 1.4 GHz dataset was used (the best which is after 2002), to achieve better accuracy. This is another of the many advantages of using multiple data-sets.

PSR J1518+4904 has been observed with Effelsberg from 1997. Until, 1999 only at 1.4 GHz, until 2006 at 1.4 GHz and 800 MHz and from 2005 at 1.4 and 2.7 GHz. The profile of this pulsar is presented in Figure 4.17 (taken from the EPN). After calibrating the data and updating the solar system ephemeris we had an improvement of 4 μs over the previous timing solution. The "alignment" of the TOAs decreased the accuracy by a factor of two. This results from phase drifting in many of the old data (until 2002), caused by an inaccurate parameter file. Specifically, the measured drift is $\sim$ 0.043 ns from pulse to pulse ($\sim$ 3.8 μs per minute). This is the reason why Janssen et al. (2008) did not use the older Effelsberg datasets. Here we try to use everything, without the alignment. We use 809 "individual" TOAs at three frequencies producing an rms of 19 μs.

By fitting the $\sim$10 years of multi-frequency TOAs form Effelsberg we get the post-fit residuals versus time presented in Figure 4.18. All the toas were analysed by tempo2 with the binary DD model. In Table 4.8 all the improved astrometric, spin and binary parameters produced by tempo2 are presented. The uncertainties of the TOAs are scaled by a factor of 4.5 at all frequencies (very high caused by the profile drifting) to achieve a uniform reduced χ^2=1. Most of the parameters can be derived with the Effelsberg datasets with quite good accuracy. However, when comparing to the EPTA values (Janssen et al. 2008) the differences are significant. All the EPTA measurements have at least one order of magnitude better uncertainties. In, addition PK values such as variation of the projected semi-major axis $\dot{x}$ cannot be obtained without the full use of the EPTA TOAs.

PSR J1518+4904 is not an ideal case for use in the EPTA for gravitational wave detections because of its long rotational period. Nevertheless, being one of the few NS-NS system observed with such a high accuracy it is giving us the opportunity to measure and constrain PK parameters, as done in Janssen et al. (2008). Further addition of TOAs, new or old re-calibrated ones and an increase of the S/N ratio, will improve our timing accuracy and lead to better results and new measurements (i.e. of the orbital period decay $\dot{P}_b$). This will enable us to test General
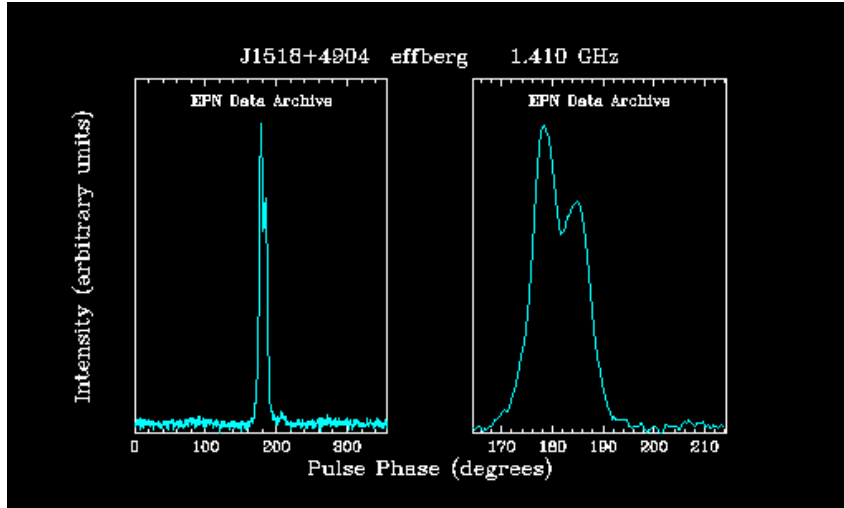
Figure 4.17: **The integrated profile of PSR J1518+4904 at 1.4 GHz taken from the EPN.**
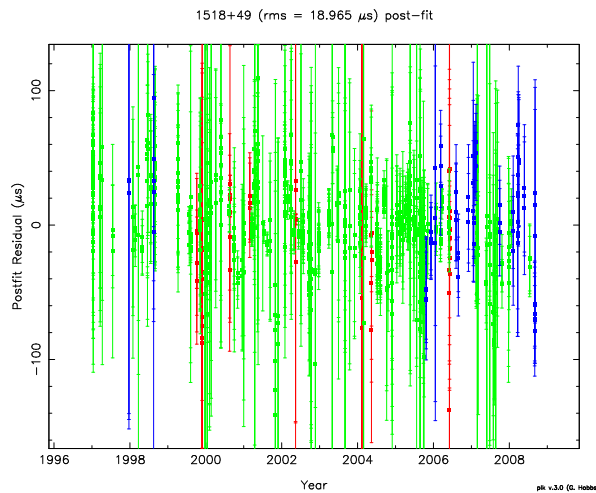
Figure 4.18: **The post-fit residuals in μs versus time in years for PSR J1518+4904, as produced by tempo2. With green are the 1.4 GHz TOAs, with red the 800 MHz and with blue the 2.7 GHz.**

Relativity and constrain even more the masses of the two neutron stars, getting one step closer to the truth about the history of evolution of this system.

4.9   PSR J1623−2631

PSR J1623−2631 (B1620-26) is an 11 ms pulsar in a 191 day low eccentricity orbit with a ∼0.3 M$_{\odot}$ white dwarf companion (Lyne et al. 1988; McKenna & Lyne 1988). It was discovered (Lyne et al. 1988) with Lovell radio telescope in a search for pulsars in globular clusters and the first distance estimation was 2.2±0.8 kpc, using the observed value of DM=63 cm^{-3} pc and the Lyne et al. (1985) electron density distribution model. It is the second millisecond pulsar found

Table 4.8: **The spin and astrometric parameters of PSR J1518+4904.**

Parameters	Effelsberg
α (J2000)	15:18:16.79930(11)
δ (J2000)	+49:04:34.2664(17)
ν (s^{-1})	24.4289793825394(14)
$\dot{\nu}$ (s^{-2})	-1.6251×10^{-17}(7)
PEPOCH (MJD)	50850.000119483
POSEPOCH (MJD)	50850.000119483
DMEPOCH (MJD)	50850
DM (cm^{-3} pc)	11.6208(11)
μ_α (mas/yr)	-1.82(19)
μ_δ (mas/yr)	-8.4(3)
P$_b$ (d)	8.634005094(7)
T$_0$ (MJD)	50845.9876518(16)
x (lt-s)	20.043954(4)
ω (deg)	342.49169(7)
e	0.24948268(16)
$\dot{\omega}$ (deg/yr)	0.011358(13)
No of TOAs	809
Post-fit rms (μs)	19

Figures in parentheses are the nominal 1σ TEMPO2 uncertainties in the list-significant digits quoted

in a globular cluster, M4, and the first in a low-mass binary system. From the early timing it was found that the data could not be well described by a simple Keplerian model (Thorsett 1991b). It is now confirmed that there is a second companion (Backer et al. 1993) in a low eccentricity, wide circumbinary orbit ($\sim$35 AU) around the pulsar WD system, with a mass of 1-3 M$_j$ (planet or sub-stellar object) (Rasio 1994; Sigurdsson 1995; Arzoumanian et al. 1996; Joshi & Rasio 1997) and orbital period of the order of 100 yr (Thorsett et al. 1999).

The most precise timing analysis was presented by Thorsett et al. (1999) (postfit rms 31 μs) where for the first time a significant measurement of the pulsar proper motion has been made (μ_α=-11.6 mas/yr and μ_δ=-15.7 mas/yr) but is not in agreement with the cluster proper motion measured from optical observations (μ_α=-1.8±1.2 mas/yr and μ_δ=-9.3±5 mas/yr) (Cudworth & Hanson 1993). Another important measurement is a secular change in the projected semi-major axis of the inner binary, which actually confirms the triple nature of the system ($\dot{x} = -6.7 \times 10^{-13}$).

Optical observations with HST and photometry on the Canada-France-Hawaii Telescope (CFHT) of M4 by Richer et al. (2003), determined the position of the WD to be coincident to the pulsar within 0".12±0".13 and revealed that the proper motion of the white dwarf companion of PSR J1623−2631 with respect to the cluster is about 0.9±1.1 mas/yr, value that is physically acceptable.

PSR J1623−2631 has been observed at irregular intervals with Effelsberg at 1.4 GHz since 1999 and sometimes at 800 MHz (which were not used because of no significant detection of the pulse) and 2.7 GHz. Its not a very strong pulsar with a profile consisting of three components (Figure 4.19, taken from the EPN). After the usual calibration of the data and the updated solar system ephemeris we "aligned" the individual scans of every session. Although the S/N ratio

of all the profiles was improving as expected, the fit was still far from optimal. The problem was that apparently after a point the TOAs for the specific source were being produced with a different template. This fact was introducing inconsistencies between the two datasets, resulting in huge postfit rms values. Thus, we reproduced all the TOAs with the latest created template finally using a total of 47 "aligned" TOAs (46 at 1.4 and 1 at 2.7 GHz), deriving an rms of 3.9 μs.
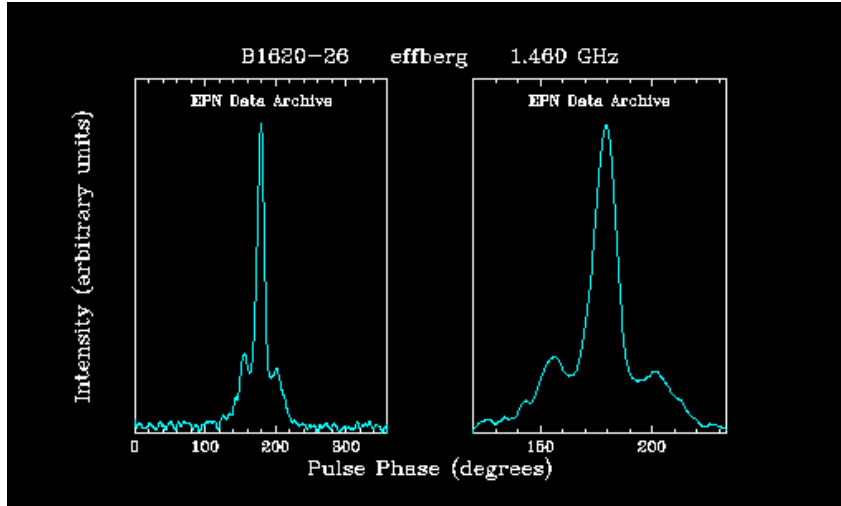
Figure 4.19: **The integrated profile of PSR J1623$-$2631 at 1.4 GHz taken from the EPN.**

By fitting the $\sim$8 years of Effelsberg TOAs we get the post-fit residuals versus time presented in Figure 4.20. All the toas were analysed by tempo2 using the DD binary model. In Table 4.9 all the improved astrometric, spin and binary parameters produced by tempo2 are presented. The uncertainties of the TOAs are scaled by a factor of 1.7 at all frequencies to achieve a uniform reduced $\chi^2 \simeq 1$. By keeping the DM value fixed we measure all the parameters, getting values consistent with the ones from Thorsett et al. (1999). Although the frequency derivatives are not measured in such a high accuracy (caused by the lack of many TOAs), all the orbital parameters are. In addition, we manage for the first time to get a significant (3σ) measurement of the change in the orbital period of the system. Finally, we must mention that the post-fit rms is reduced almost by an order of magnitude.

PSR J1623$-$2631 is the only triple system with a pulsar ever discovered. Thus, complete determination of its properties offers a unique opportunity in understanding creation and evolution of such systems. Currently, Effelsberg cannot provide efficient timing data for a complete accurate timing analysis. However, combination with the rest of the EPTA ones would expand our dataset, resulting in better estimations of the frequency derivatives and would also provide multi-frequency data for proper DM corrections. Finally, the low rms of 3.9 could be improved even more making the pulsar a part of the gravity wave detection effort of the EPTA.

4.10   PSR J1640+2224

PSR J1640+2224 is a 3.2 ms pulsar (Foster et al. 1995) in a high eccentricity 175 day orbit (e$\sim$ 0.0008 Wolszczan et al. (2000)) with a low mass helium WD (Lundgren et al. 1996). It was
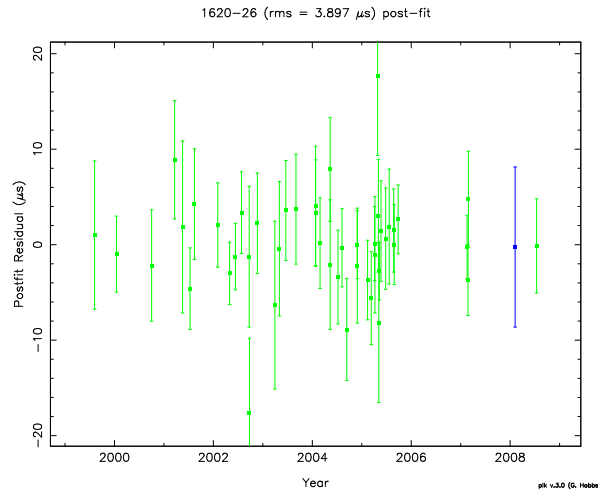
Figure 4.20: The post-fit residuals in μs versus time in years for PSR J1623$-$2631, as produced by tempo2. With green are the 1.4 GHz TOAs and with blue the 2.7 GHz.

discovered by (Foster et al. 1995) in a high Galactic latitude survey conducted at 430 MHz with the Arecibo radio telescope from 1990-1995.

The WD companion was observed in optical with the Palomar 5.1 m telescope by Lundgren et al. (1996). From the inferred luminosity, the temperature T=3700$\pm$300 K and the estimated distance d=1.2 kpc from the dispersion measure and the Taylor & Cordes (1993) electron distribution model, the object was identified as a $(2 \pm 1) \times 10^9$ yr old helium white dwarf. The age is much smaller from the spin-down age of the pulsar. From the same photometric analysis the median mass of the HWD is estimated to be m_c=0.3 M$_\odot$.

Wolszczan et al. (2000) presented a timing analysis of combined Arecibo and Effelsberg data at 430 and 1400 MHz of PSR J1640+2224 reaching a best-fit rms residual of 8.6 μs. The proper motion was measured (μ_α=0.1, μ_δ=13.3) for the first time. Since the kinematic effects cause variable Doppler shifts of the pulsar period (Shklovskii 1970) the kinematic correction to the observed $\dot{P}$ was calculated to infer the intrinsic spin down rate of the pulsar. Especially in this case, that the spin down rate is exceptionally low, the intrinsic spin down rate should be much lower than the observed one. The initial period estimation of $P_0 \geq$2.7 ms indicated very little period evolution.

The most precise timing analysis of PSR J1640+2224 to date is made by Löhmer et al. (2005) (rms 2 μs). Using long period timing gap-less data of Arecibo and Effelsberg they show that a Shapiro delay is detected to their TOAs. By estimating the r and s of the Shapiro delay they manage to restrict the companion mass to m_c=0.15 M$_\odot$, which is consistent with the optical observations of Lundgren et al. (1996), and the orbital inclination of the system to 78$\leq i \leq$88.

PSR J1640+2224 has been observed regularly with Effelsberg at 1.4 GHz since 1997 and in at least two frequencies from 1999 (irregularly at 800 MHz and from 2006 regular at 2.7 GHz). Its a very strong pulsar with a profile consisting of 1 narrow component, making it easy to time in high accuracy (Figure 4.21, taken from the EPN). After the usual calibration of the data and the updated solar system ephemeris which improved our post-fit rms almost an order of magnitude, we "aligned" the individual scans. In total we used 159 aligned" TOAs to derive an

Table 4.9: The spin and astrometric parameters of PSR J1623−2631.

Parameters	Effelsberg
α (J2000)	16:23:38.21502(10)
δ (J2000)	-26:31:53.747(7)
ν (s^{-1})	90.28733054(3)
$\dot{\nu}$ (s^{-2})	-4.8×10^{-15}(4)
$\ddot{\nu}$ (s^{-3})	1.7×10^{-23}(5)
$\nu^{(3)}$ (s^{-4})	-3.3×10^{-32}(34)
$\nu^{(4)}$ (s^{-5})	3.7×10^{-40}(19)
$\nu^{(5)}$ (s^{-6})	-1.5×10^{-48}(6)
PEPOCH (MJD)	48725.000086535
POSEPOCH (MJD)	48725.000086535
DMEPOCH (MJD)	48725
DM (cm^{-3} pc)	553.31882573795
μ_α (mas/yr)	-12.1(8)
μ_δ (mas/yr)	-20(5)
P$_b$ (d)	191.442836(3)
T$_0$ (MJD)	48728.26204(5)
x (lt-s)	64.809452(12)
ω (deg)	117.12840(9)
e	0.02531546(4)
$\dot{P}_b$	-2.0×10^{-9}(6)
$\dot{x}$	-5.8×10^{-13}(4)
No of TOAs	47
Post-fit rms (μs)	3.9

Figures in parentheses are the nominal 1σ TEMPO2 uncertainties in the list-significant digits quoted

rms of 1.7 μs, a somewhat better than that one achieved by Löhmer et al. (2005).

By fitting all these 10 years of multi-frequency TOAs we get the post-fit residuals versus time presented in Figure 4.22. All the toas were analysed by tempo2 using the DD binary model. In Table 4.10 all the improved astrometric, spin and binary parameters produced by tempo2 are presented. The uncertainties of the TOAs are scaled by a factor of 1.55 at all frequencies to achieve a uniform reduced $\chi^2 \approx 1$. As presented, we measure all the fitted parameters with high accuracy. Everything is consistent with the values of Löhmer et al. (2005) and almost at the same uncertainty level. When checking for the Shapiro delay reported previously, as described in section 4.2, we detect for our measured mass function, $f_p = (m_c \sin i)^3/(m_p + m_c)^2 = (797479.4312 \pm 0.4484) \times 10^{-8}$ and by setting $m_c = 0.15\,\mathrm{M}_\odot$, a minimum of the χ^2 when the $\sin i$ was getting the value 0.85 (Figure 4.23), which implies an inclination angle of $\sim 60^o$, a bit lower the previously estimated lower limit.

The combination of the EPTA with the Arecibo and Effelsberg data could immediately provide better estimation errors of the companion mass and the inclination angle of the system. This would provide more information about the evolution of the low and intermediate mass binary systems. In addition, a possible measurement of another PK parameter (apart from the range and shape of the Shapiro delay) would set the ground to test general relativity. Finally, PSR J1640+2224 is also likely to become a valuable member of the EPTA sample to detect
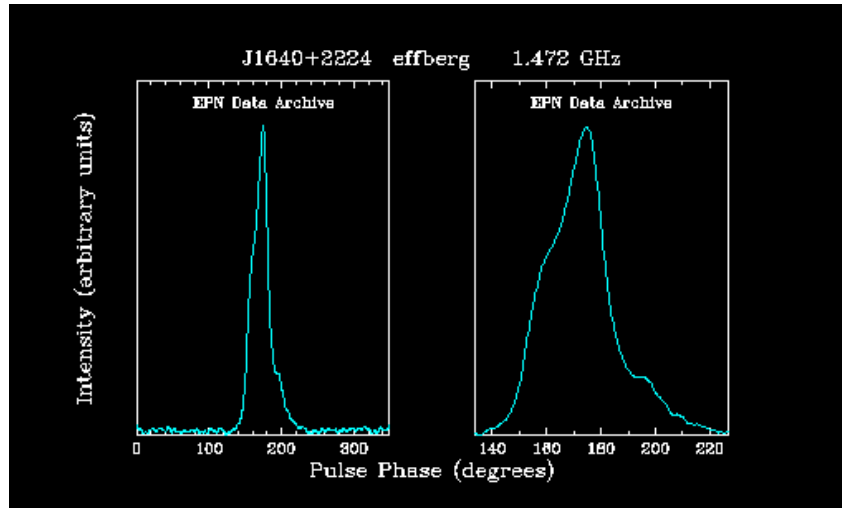
Figure 4.21: **The integrated profile of PSR J1640+2224 at 1.4 GHz taken from the EPN.**
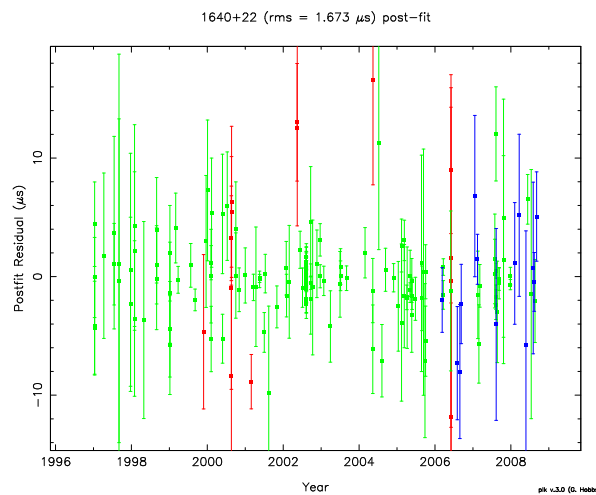
Figure 4.22: **The post-fit residuals in μs versus time in years for PSR J1640+2224, as produced by tempo2. With green are the 1.4 GHz TOAs, with red the 800 MHz and with blue the 2.7 GHz.**

the low-frequency background of gravitational radiation, since it is one of the most accurately timed pulsars.

4.11 PSR J1643−1224

PSR J1643−1224 is the second most luminous millisecond pulsar after PSR B1937+21, with 4.622 ms period in a roughly circular orbit with period of 147 days around a low mass (∼0.13 M$_\odot$) companion (possibly white dwarf). It was discovered in 1994 in a survey of the Southern Hemisphere with the Parkes radio telescope by Lorimer et al. (1995b) at Galactic longitude b=5.67 and latitude l=21.22 degrees. The DM=62.4 pc cm^{-3} (Lorimer et al. 1995b) together with

Table 4.10: **The spin and astrometric parameters of PSR J1640+2224.**

Parameters	Effelsberg
α (J2000)	16:40:16.743547(11)
δ (J2000)	+22:24:08.9454(3)
ν (s^{-1})	316.1239794121206(16)
$\dot{\nu}$ (s^{-2})	-2.81521$\times10^{-16}$(14)
PEPOCH (MJD)	51700.000132662
POSEPOCH (MJD)	51700.000132662
DMEPOCH (MJD)	51700
DM (cm^{-3} pc)	18.4292(8)
μ_α (mas/yr)	2.01(4)
μ_δ (mas/yr)	-11.47(6)
P$_b$ (d)	175.46066457(3)
T$_0$ (MJD)	51626.1804(3)
x (lt-s)	55.3297238(3)
ω (deg)	50.7343(6)
e	0.000797258(11)
No of TOAs	159
Post-fit rms (μs)	1.7

Figures in parentheses are the nominal 1σ TEMPO2 uncertainties in the list-significant digits quoted
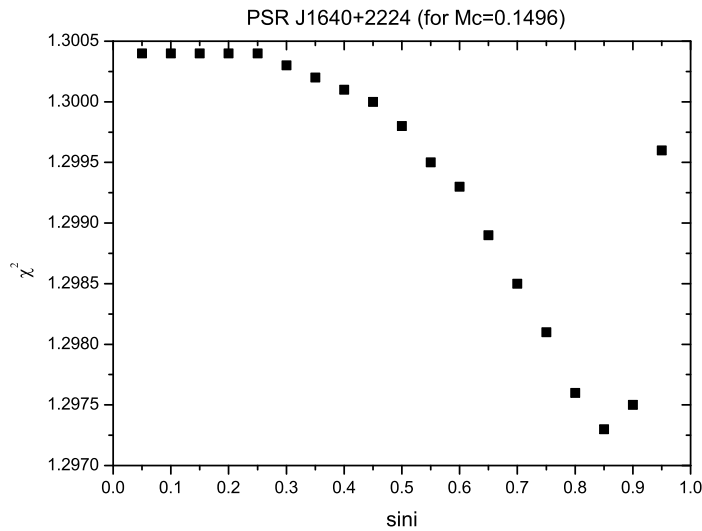
Figure 4.23: **The curve represents the χ^2 values for fixed $m_c = 0.15\,M_\odot$, where the most probable (minimum χ^2) inclination value is for** $\sin i$**=0.85.**

the Taylor & Cordes (1993) electron density model results in a distance estimate of 0.49 kpc (Toscano et al. 1999b). Bell et al. (1997) using Jodrell Bank data observed variations of the DM

of PSR J1643−1224 equal to $\dot{DM}$=0.0010.

Toscano et al. (1999b) present the most accurate timing analysis of PSR J1643−1224 using TOAs from Parkes, managing to measure its proper motion of 8±5 mas/yr and the velocity of 159 km/s. They also deduced a magnetic field strength of ∼2.2×10^8 G and a characteristic age of ∼7.5 Gyr.

Maitia et al. (2003) report the detection of an extreme scattering event (ESE) in the direction of PSR J1643−1224 with the use of the Nançay radiotelescope. Its duration was 3 years, from 1996 to 1999, and it is the longest ESE ever recorded. One of the explanations, from the models they applied for the scattering screen to their radio light curve, is a fully ionised cloud crossing the line of sight. Its transverse size is 56 AU (much bigger that the typical ones ∼1 AU) and it has extremely short lifetime (29 yr).

PSR J1643−1224 has been observed with Effelsberg regularly from 1997 at 1.4 GHz and from 2007 also at 2.7 GHz and irregularly at 800 MHz from 1999. Its a very strong pulsar with a profile consisting of 1 narrow component, making it easy to time in high accuracy (Figure 4.24, taken from the EPN). After the usual calibration of the data and the updated solar system ephemeris which improved our post-fit rms by almost 7 times, we "aligned" the individual scans. In total we used 95 aligned" TOAs from 1999 to derive an rms of 4 μs, ∼2 μs better than the one achieved by Toscano et al. (1999b).
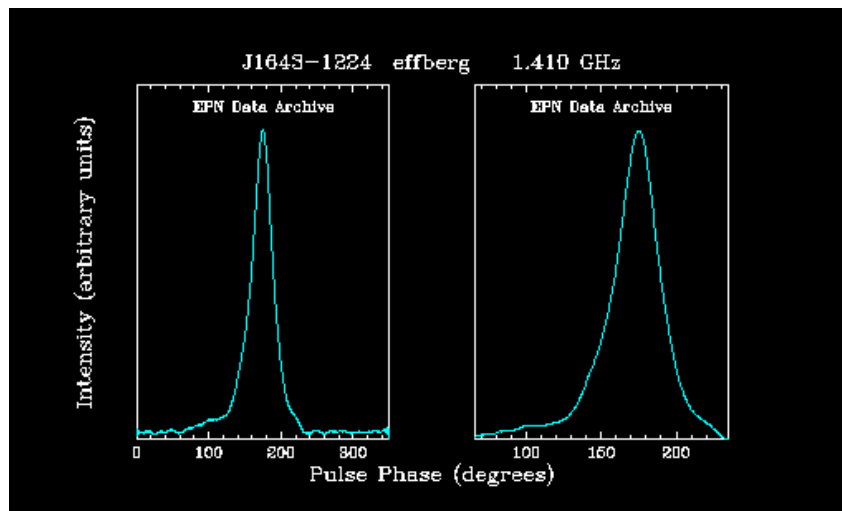
Figure 4.24: **The integrated profile of PSR J1643−1224 at 1.4 GHz taken from the EPN.**

By fitting our 10 years of TOAs we get the post-fit residuals versus time presented in Figure 4.25. All the toas were analysed by tempo2 using the DD binary model. In Table 4.11 all the improved astrometric, spin and binary parameters produced by tempo2 are presented. The uncertainties of the TOAs are scaled by a factor of 1.9 at 1.4 GHz and 1.6 at 800 and 2700 MHz to achieve a uniform reduced $\chi^2 \approx 1$. As shown, we measure all the fitted parameters with high accuracy. Everything is consistent with the values of Toscano et al. (1999b) and in addition all the uncertainties are now by an order of magnitude better. In addition we managed for the first time to get a measurement of the timing parallax $\pi = 2.4 \pm 1.0$ mas, which although is not yet significant enough it provides a distance estimation of ∼ 416 pc, consistent with the DM

distance. Finally, for the first time we obtain a value for the change of the projected semi-major axis of $\dot{x} = (-5.2 \pm 0.5) \times 10^{-14}$.
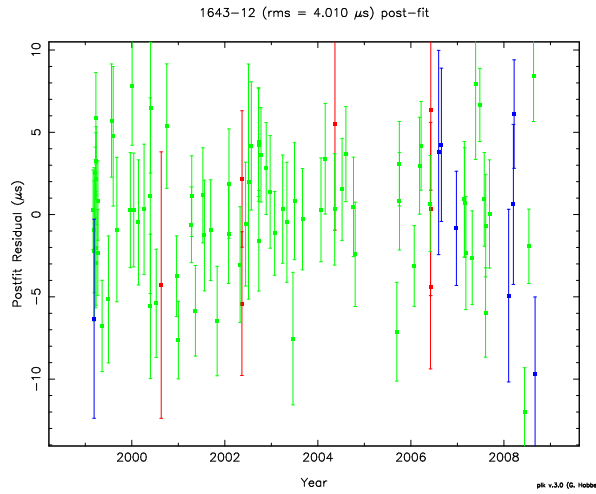
Figure 4.25: **The post-fit residuals in μs versus time in years for PSR J1643$-$1224, as produced by tempo2. With green are the 1.4 GHz TOAs, with red the 800 MHz and with blue the 2.7 GHz.**

Table 4.11: **The spin and astrometric parameters of PSR J1643$-$1224.**

Parameters	Effelsberg
α (J2000)	16:43:38.15637(6)
δ (J2000)	-12:24:58.717(4)
ν (s^{-1})	216.373337494510(6)
$\dot{\nu}$ (s^{-2})	-8.6424$\times 10^{-16}$(3)
PEPOCH (MJD)	50288.000110769
POSEPOCH (MJD)	50288.000110769
DMEPOCH (MJD)	50288
DM (cm^{-3} pc)	62.4175(14)
μ_α (mas/yr)	5.90(11)
μ_δ (mas/yr)	3.6(6)
P$_b$ (d)	147.01739768(7)
T$_0$ (MJD)	50313.0597(19)
x (lt-s)	25.0726009(6)
ω (deg)	321.859(5)
e	0.00050572(5)
$\dot{x}$	-5.2(5)$\times 10^{-14}$
No of TOAs	95
Post-fit rms (μs)	4.0

Figures in parentheses are the nominal 1σ TEMPO2 uncertainties in the list-significant digits quoted

In the case of PSR J1643$-$1224, combination of the multi-frequency EPTA TOAs is of great importance, in order to be able to constantly monitor and model the DM and its variations. Just

to remind that DM monitoring has to be done for all the PTA sources to avoid extra noise factors in our data. In addition, we might be able to get a significant value for the parallax and the distance to the pulsar. Finally, the measurement of $\dot{x}$ (after identifying the contribution from the proper motion and from the actual shrinkage of the orbit) in combination with the proper motion in right ascension and declination can lead to constrains of the inclination angle (equation (4.2)) of the system and hence the mass of the companion.

4.12   PSR J1744−1134

PSR J1744−1134 is a solitary pulsar with a spin period of 4 ms, characteristic age >7 Gyr and magnetic field strength <1.9× 10^8 Gauss (Bailes et al. 1997). It was discovered in the Parkes 436 MHz survey of the southern sky (Bailes et al. 1997) and its narrow pulse profile make it an ideal source for precision timing.

Toscano et al. (1999a,b) reach an rms of 300 ns and measure the proper motion and a parallax of 2.8±0.34 mas for the pulsar. The distance of 357 pc derived from the parallax measurement is much bigger than the 166 pc from the DM=3.14cm^{-3} and the Taylor & Cordes (1993) Galactic electron density model. The improved distance measurement yields a mean electron density in the path to the pulsar of $n_e = (8.8 \pm 0.9) \times 10^{-3}$ cm^{-3} and a pulsar X-ray luminosity of L$_X < 1 \times 10^{29}$ d^2 erg s^{-1}.

The most recent timing solution for PSR J1744−1134 was presented by Hotan et al. (2006), achieved from 3 yrs of Parkes observations. This measured proper motions (μ_α=19.6 and μ_δ=-7 mas/yr) differ from those of Toscano et al. (1999b) (μ_α=18.72 and μ_δ=-9.5 mas/yr) (about 3σ in both coordinates). Also their parallax measurement of 2.1±0.4 mas is smaller than the one published by Toscano et al. (1999b) (within 2σ) and effectively the derived distance of 470 pc is larger. Important to notice is the detection of an apparent long period timing noise with an amplitude of $\sim 2\mu$s, which may deteriorate the extremely high timing precision of the pulsar.

PSR J1744−1134 has been observed regularly with Effelsberg from 1998 at 1.4 GHz and from 2007 also at 2.7 GHz and irregularly at 800 MHz from 1999. Its a strong pulsar with a profile consisting of 1 very narrow component, making it ideal to time with high precision (Figure 4.26, taken from the EPN). After the usual calibration of the data and the updated solar system ephemeris which doubled our timing accuracy, we "aligned" the individual scans. In total we used 85 aligned" TOAs from 1999 to derive an rms of 618 ns, almost twice the value of Hotan et al. (2006), but with three times longer time span.

By fitting our 10 years of TOAs we get the post-fit residuals versus time presented in Figure 4.27. All the TOAs were analysed by tempo2. In Table 4.11 all the improved astrometric and spin parameters produced by tempo2 are presented. The uncertainties of the TOAs are scaled by a factor of 1.8 at 1.4 GHz and 800 MHz and 1.4 at 2.7 GHz to achieve a uniform reduced $\chi^2 \approx 1$. As shown, we measure all the fitted parameters with high accuracy. When we compare our values, such as the proper motion and parallax, with the previously published ones we are more consistent with the ones from Toscano et al. (1999a) and not with Hotan et al. (2006). In addition, our error uncertainties are better by an order of magnitude from the previously published ones. Since, we are also using much longer time span of TOAs, we are confident that our measurements are the best at the moment. We finally derive a total proper motion of $\mu_t = 21.02 \pm 0.03$ mas/yr and a parallax distance of $d = 373 \pm 63$ pc.

It is clear that this extremely close millisecond pulsar can be timed with nanosecond accuracy. It is an ideal candidate already for the EPTA gravitational wave search and in the top
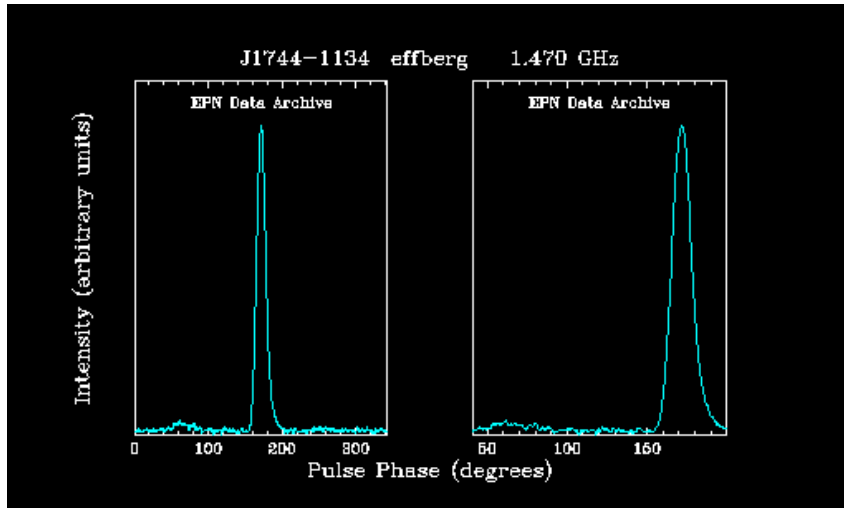
Figure 4.26: **The integrated profile of PSR J1744−1134 at 1.4 GHz taken from the EPN.**
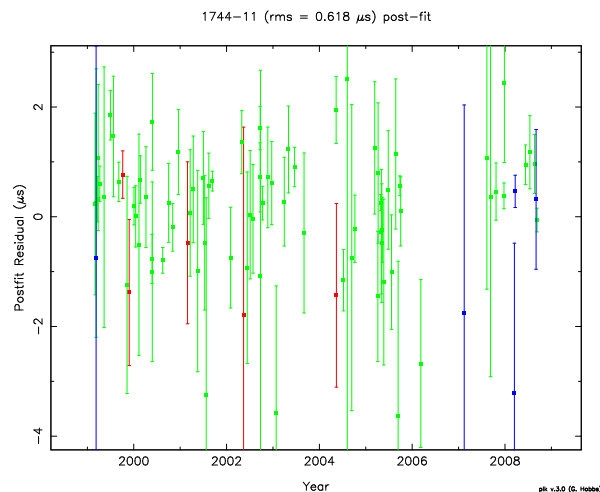
Figure 4.27: **The post-fit residuals in μs versus time in years for PSR J1744−1134, as produced by tempo2. With green are the 1.4 GHz TOAs, with red the 800 MHz and with blue the 2.7 GHz.**

five pulsars we regularly time. At the moment the EPTA is working in improving its timing solution even further by combining the data from all the telescopes (Desvignes et al. in prep.). It is important to mention that in the current analysis we detected for the first time traces of DM variations of the order of $(14 \pm 8) \times 10^{-5}$ cm^{-3} pc yr^{-1}. Use of all the telescopes multi-frequency data will allow us to monitor this variations much more efficiently and enable us to model and correct them in our timing solution.

Table 4.12: The spin and astrometric parameters of PSR J1744−1134.

Parameters	Effelsberg
α (J2000)	17:44:29.391592(6)
δ (J2000)	-11:34:54.5762(5)
ν (s^{-1})	245.4261199021225(10)
$\dot{\nu}$ (s^{-2})	-5.38180×10^{-16}(5)
PEPOCH (MJD)	50434.000113033
POSEPOCH (MJD)	50434.000113033
DMEPOCH (MJD)	50434
DM (cm^{-3} pc)	3.1364(3)
μ_α (mas/yr)	18.842(13)
μ_δ (mas/yr)	-9.33(7)
π (mas)	2.68(17)
No of TOAs	85
Post-fit rms (μs)	0.62

Figures in parentheses are the nominal 1σ TEMPO2 uncertainties in the list-significant digits quoted

4.13 PSR J2051−0827

PSR J2051−0827 is an eclipsing millisecond pulsar system discovered (Stappers et al. 1996) as part of Parkes survey of the southern sky for low-luminosity and millisecond pulsars. The pulsar has a period of 4.5 ms and is in a very compact circular orbit of 1.03 R$_\odot$ and period of P$_b$=2.38 h, with a companion of mass ~ 0.03 M$_\odot$. From the low frequency part of the observations Stappers et al. (1996) showed that the eclipse duration is 10% of the orbital period, while at the high frequencies ($\sim$1.4 GHz) there were no visible eclipses. The small dispersion-derived distance (Taylor & Cordes 1993) to the pulsar, $d = 1.3$ kpc, indicates that there might be a significant contribution to the measured value of $\dot{P}$ from the Shklovskii effect (Shklovskii 1970). Thus, their estimates of the magnetic field strength 2.4×10^8 G and the characteristic age 5×10^9 yr may not be very accurate.

Stappers et al. (1998) perform the first high precision timing analysis of PSR J2051−0827 with 3.3 years of Parkes TOAs at 5 frequencies. They measure a decrease in the orbital period at a rate of $\dot{P}_b = (-11 \pm 1) \times 10^{-12}$ which implies a decay time of the orbit of only 25 Myr, much shorter than the expected timescale for the ablation of the companion. Another significant measurement is that of the proper motion of 5 ± 3 mas/yr which implies a slow transverse velocity $v_t = 30 \pm 20$ km/s and a negligible contribution to the period derivative (3.4×10^{-22}) of just 3% of the measured one.

Optical detection of the companion to PSR J2051−0827 showed that a significant fraction of the spin-down energy flux of the pulsar is heating the surface of the companion (Stappers et al. 1996; Stappers et al. 1999). This, in combination with the observation of eclipse material well beyond the Roche lobe, suggests that PSR J2051−0827 is in the process of ablating its companion.

Doroshenko et al. (2001) presented the most precise timing analysis of PSR J2051−0827 using 6.5 yr of radio timing measurements with the Effelsberg 100m radio telescope and the Lovell 76m dish at Jodrell Bank. Among the most important measurements is the variation of the projected semi-major axis of the pulsar at a rate of $\dot{x} = d(a_1 \sin i)/dt = (-0.23 \pm 0.03) \times$

10^{-12}, probably caused by the Newtonian spin-orbit coupling in this binary system leading to a precession of the orbital plane. They also confirmed the previous value of the decrease of the orbital period and they measured in addition second and third orbital period derivatives $dP_b^2/dt^2 = (2.1 \pm 0.3) \times 10^{-20} \, \mathrm{s}^{-1}$, $dP_b^3/dt^3 = (3.6 \pm 0.6) \times 10^{-28} \, \mathrm{s}^{-2}$. Finally they give a value for the radius of the companion of $R_{cmax} \sim 0.06 \, \mathrm{R}\odot$ which is about half the size of its Roche lobe (R_l=0.13 $\mathrm{R}_\odot$, its under-filling its Roche lobe by 50%)

PSR J2051-0827 has been observed with Effelsberg regularly from 1997 at 1.4 GHz, from 2006 also at 2.7 GHz and irregularly at 800 MHz from 1999 until 2006. After performing the usual calibration of the data and updating the solar system ephemeris considerable drifting was detected in the data. For that reason we did not carry out the usual profile "alignment". Instead, for this source we finally used 528 "individual" Effelsberg TOAs, but still a peculiar behaviour was detected in the post-fit residuals. By fitting those 14 years of TOAs and analysing the toas with tempo using the ELL1 binary model there was no improvement in the rms (overall 49 μs) which is inexplicable high for this pulsar. After closer investigation we detected that this was caused by extreme and strange periodical variations of the residuals for most of our time-span as shown in Figure 4.28 (the unexplained increase and decrease of the residuals). It was unclear if this effect is caused by systematics in Effelsberg data or it is intrinsic to the source.
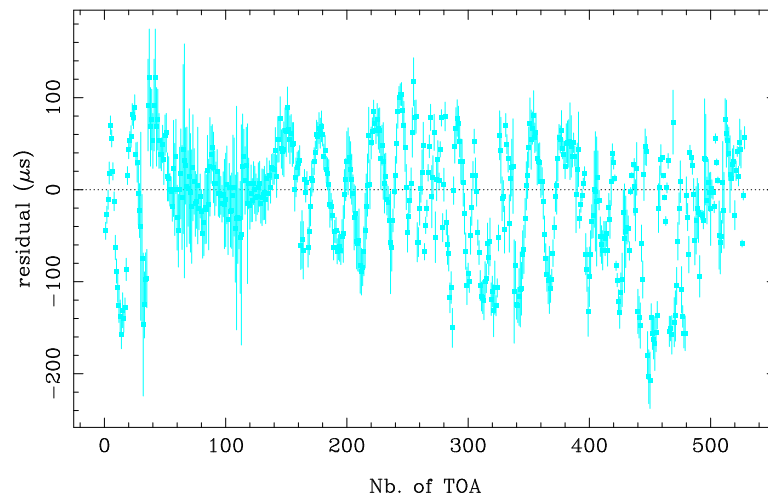
Figure 4.28: **The post-fit residuals in μs versus number of TOA for PSR J2051−0827, as produced by tempo. Clear big residual variations are present after TOA ∼120.**

Here the access to EPTA data becomes important. PSR J2051−0827 has been observed at Jodrell Bank from 1994 at 400, 600 and 1400 MHz. In addition, at Westerbork at 300 and 1400 MHz from 2007 and finally at Nançay from 2004 at 1400 MHz (technical information about these observations can be found in Chapters 2 and 3). Work is still in progress (Lazaridis et al. in prep.) to complete the analysis of all the EPTA data (in combination also with old Parkes data) and in the current section we will present only the preliminary analysis of the 1400 MHz ones. When plotting all the EPTA TOAs together we end up with 4147 high quality TOAs, 80% of which provided from Nançay radiotelescope. Investigation of the the other telescopes data revealed the same strange variations of the residuals, excluding the possibility of systematic measurement errors in Effelsberg. The next step was to try to fit these variations

with tempo properly. The model used so far, was fitting for the binary parameters of x (projected semi-major axis), P_b (orbital period) and their first derivatives without however improving the post-fit. After suspecting non-linear variation of these parameters we had to turn to higher order derivatives. For that reason we used the binary model BTX, a model for non-linear frequency variation which allows fitting of higher order orbital frequency ν_b and x derivatives. Before start fitting for the high-order derivatives we constructed, in order to inspect the variation of x and ν_b through time, a plot of them versus the MJD (as described in section 3.3.4). In Figure 4.29 the clearly non-linear variation of the x and ν_b is shown. Just by comparing the left and right part of this picture we see that both can be described better by possibly 3rd order polynomial fits (although the left is too noisy we can still distinguish that it could be described better by a polynomial fit). The second important fact is that the two polynomials would have an opposite
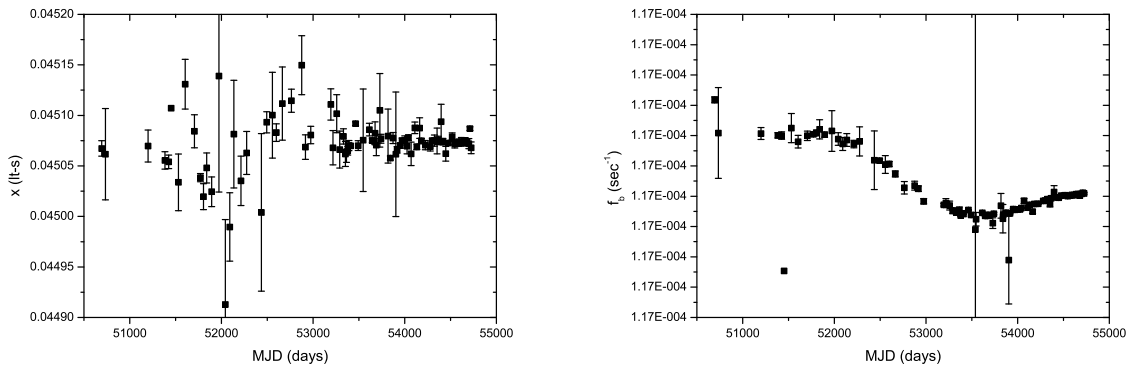
Figure 4.29: **(Left) The non-linear variation of x versus time. The early error bars are bigger due to the less TOAs used. (Right) The non-linear variation of ν_b versus time.**

sign. The reason we consider this, is because if those variations were arising just from the emission of gravitational waves from the system we would expect from Keplers 3rd law to have:

$$\frac{\dot{x}}{x} = \frac{2}{3}\frac{\dot{P}_b}{P_b} = -\frac{2}{3}\frac{\dot{\nu}_b}{\nu_b}. \tag{4.3}$$

Although the opposite sign agrees with this prediction, the order of the polynomial does not. Thus, we immediately have the first proof that the variation must have more contributions, as already discussed in Doroshenko et al. (2001).

We then ran tempo using the BTX model and fitted for higher order derivatives of the afore-mentioned parameters. We only achieved a reduced $\chi^2 \sim 1$ and make the TOA variations disappear almost completely, after fitting for 4th and 5th orbital frequency derivative and projected semi-major axis respectively. The pre and post-fit of all the 1.4 GHz EPTA TOAs are shown in Figure 4.30, where we achieved an improved post-fit rms of 11.1 μs.

As mentioned before, work and analysis is still in progress (Lazaridis et al. in prep.). The fact that such high order of derivatives should be fitted cannot be easily explained through physical processes. Thus, deeper investigation has to be made to be certain about the exact origin of the observed variations. The next step will be to re-visit PSR J2051−0827 performing high precision timing with all the available EPTA (+old Parkes) data.
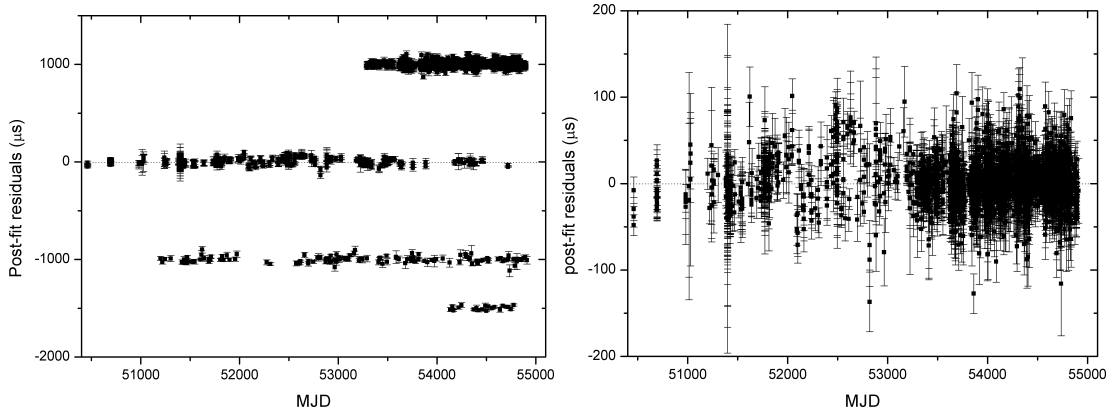
Figure 4.30: **(Left) The pre-fit residuals versus time of PSR 2051−0827. From top to bottom are Nançay, Effelsberg, Jodrell Bank and WSRT residuals. (Right) The post-fit of the EPTA 1.4 GHz residuals versus time.**

4.14   PSR J2145−0750

PSR J2145−0750 is a binary millisecond pulsar with a period of 16.05 ms in circular orbit of 6.8 days with a low mass companion close to the ecliptic plane with an ecliptic latitude of only β=5.3^o. It was discovered by Bailes et al. (1994) in a survey of the southern sky with the Parkes radio telescope. They also reported that the companion should be a white dwarf with mass $m_c \geq 0.43 \, \mathrm{M_\odot}$.

Löhmer et al. (2004) present the results from high precision measurements of PSR J2145−0750 with the Effelsberg and Lovell radio telescopes. They report the measurement for the first time of the parallax of π=2.0(6) mas which gives a distance of 500 pc to the pulsar. This value is consistent with both the distance estimations from the DM combined with the Taylor & Cordes (1993) model (500 pc) and the NE2001 model (Cordes & Lazio 2001) (570 pc). They also derived a transverse velocity of v_t=33 km/s, which is also consistent with scintillation velocities of 31±25 km/s, obtained by Nicastro & Johnston (1995). The second very important detection was the secular change of the projected semi-major axis of the orbit $\dot{x}$=1.8(6)×10^{-14} lts/s which is caused by the proper motion of the system. Using that measurement they give an upper limit for the inclination angle i <61°. In addition the non-detection of a Shapiro delay is inducing a limit for the companion mass of 0.7≤ m_c ≤1.0 $\mathrm{M_\odot}$. Finally by applying their measurement to white dwarf cooling models they calculated an effective temperature of T_{eff}=5750±600 and a cooling age of τ_{cool}=3.6(2) Gyr for the companion, values very close to the ones derived from optical observations by Lundgren et al. (1996).

The latest high precision timing analysis for PSR J2145−0750 was made by Hotan et al. (2006) with 3 years of data from the Parkes radio telescope. In their analysis they question the previous parallax and $\dot{x}$ measurements. For the former they give an upper limit of 0.9 mas, which implies a distance above 1.1 kpc and for the latter by adopting it and fitting for parallax they get a result below zero, which is clearly false.

PSR J2145−0750 has been observed with Effelsberg regularly from 1995 (until 1997 with EPOS) at 1.4 GHz, from 2006 also at 2.7 GHz and irregularly at 800 MHz from 1999 until 2006. Its a millisecond pulsar with a broad multi-component profile consisting of narrow features,

making it easier to time in high accuracy (Figure 4.31, taken from the EPN). After performing the usual calibration of the data and updating the solar system ephemeris, which almost doubled our timing accuracy, we "aligned" the individual scans. Unfortunately, we observed a decrease in the accuracy, because of possible changes of features of the profile, since there was no drifting detected in any of the data. We finally used 508 "individual" TOAs from 1997 to derive an rms of 2.6 μs, two times worse than the value of Hotan et al. (2006), but with four times longer time span.
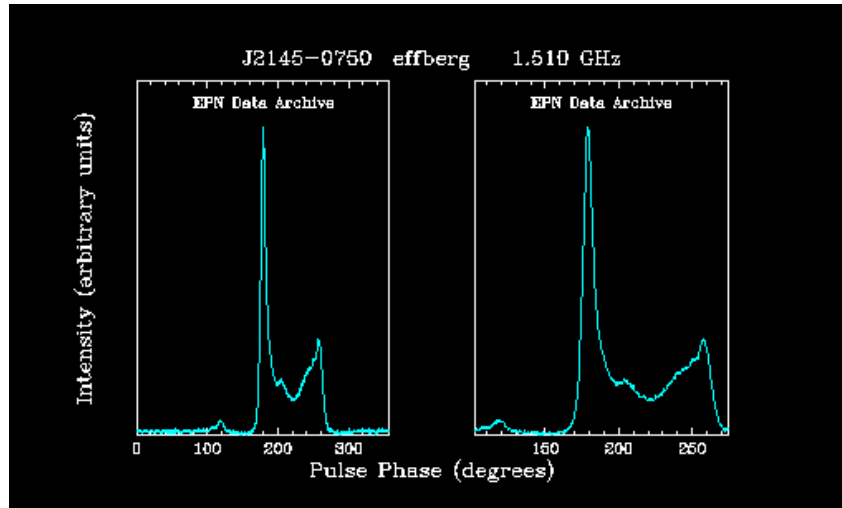
Figure 4.31: **The integrated profile of PSR J2145−0750 at 1.5 GHz taken from the EPN.**

By fitting those 14 years of TOAs we get the post-fit residuals versus time presented in Figure 4.32. All the toas were analysed by tempo using the ELL1 binary model. At the time of the analysis, a tempo2 software bug would not allow to fit some of the needed parameters in combination with the used binary model. In Table 4.13 all the improved astrometric, spin and binary parameters produced by tempo are presented. The uncertainties of the TOAs are scaled by a factor of 1.8 at 1.4 GHz and 800 MHz and 1.5 at 2.7 GHz to achieve a uniform reduced $\chi^2 \approx 1$. As shown, we measure with high accuracy all the fitted parameters. When we compare our values with the previously published ones by Hotan et al. (2006) we are consistent in most of them. In addition almost all our errors are smaller at least by an order of magnitude. Thus, we are confident about the quality of our data. Since, it has been a matter of debate, our first concern was to check the measurements of the parallax and of the secular change of the projected semi-major axis ($\dot{x}$) of Löhmer et al. (2004). We acquire values for both of them. Our parallax measurement $\pi = 1.1 \pm 0.4$ mas is significantly smaller (half) than the reported one (Löhmer et al. 2004) and consistent within the error with the upper limit provided by Hotan et al. (2006). From the parallax we derive a distance estimate of $d = 909 \pm 364$ pc. Our results for $\dot{x} = (1.5 \pm 0.3) \times 10^{-14}$ is a bit smaller than the one from Löhmer et al. (2004), but consistent within the errors. Thus, we confirm the previous measurement. In addition, we get a 2σ value for DM variations. Finally, we manage for the first time to measure a change in the eccentricity of the system of $\dot{e} = (-0.0019 \pm 0.0006) \times 10^{-12}$, value that is following the upper limit given by Löhmer et al. (2004).
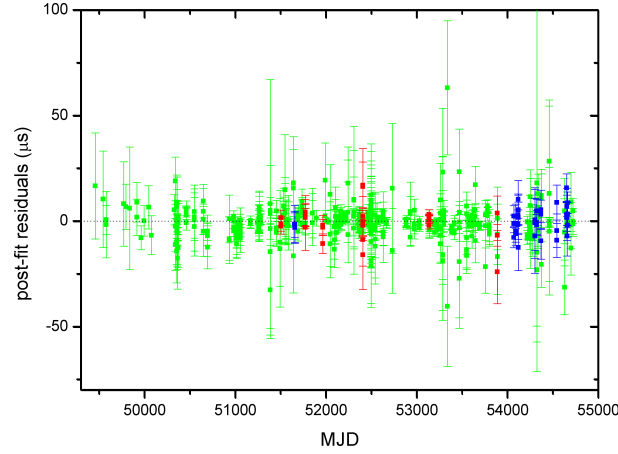
Figure 4.32: **The post-fit residuals in** μ**s versus time in years for PSR J2145**$-$**0750, as produced by tempo. With green are the 1.4 GHz TOAs, with red the 800 MHz and with blue the 2.7 GHz.**

Table 4.13: **The spin and astrometric parameters of PSR J2145**$-$**0750.**

Parameters	Effelsberg
λ (degrees)	326.02465894(6)
β (degrees)	5.3130746(6)
ν (s^{-}1)	62.2958888452464(6)
$\dot{\nu}$ (s^{-}2)	-1.15582$\times 10^{-16}$(2)
PEPOCH (MJD)	50800
DM (cm^{-}3 pc)	8.984(1)
$\dot{\text{DM}}$ (cm^{-}3 pc/yr)	0.0002(1)
μ_λ (mas/yr)	-11.81(4)
μ_β (mas/yr)	-6.5(3)
π (mas)	1.1(4)
P$_b$ (d)	6.8389025094(2)
x (lt-s)	10.1641043(6)
T$_{ASC}$ (MJD)	50802.29811056(5)
η	-0.00000691(5)
κ	-0.00001815(5)
$\dot{x}$ (ss^{-1})	1.5$\times 10^{-14}$(3)
No of TOAs	508
Post-fit rms (μs)	2.6

Figures in parentheses are the nominal 1σ TEMPO2 uncertainties in the list-significant digits quoted

Since we think that the $\dot{x}$ is arising from a change in the observed inclination i of the orbit (the relativistic and Doppler corrections are much smaller than the measured value), better constrains of this measurement and of the proper motions would provide tighter constrains to the inclination angle. Thus, combination of the EPTA data could easily provide such desirable improvements. Furthermore, a tighter limit for the companion mass can be derived providing

more information about the nature of the WD companion. Finally, as in most of the discussed sources in this chapter, improvement of the timing accuracy possibly at the 1μs level could be achieved with EPTA data and constant monitoring of the DM variations.

4.15 Conclusions

We have presented preliminary results from the precision timing analysis of 14 millisecond pulsars using the re-calibrated Effelsberg datasets. We have shown that the application of these new calibration techniques have improved significantly the timing accuracy for almost all the cases. For most of the pulsars we obtained a post-fit rms comparable or slightly worse than the previously published values, while for six sources we achieved an improvement (PSR J0218+4232, PSR J0751+1807, PSR J1623−2631, PSR J1640+2224, PSR J1643−1224, PSR J2051−0827). In addition, we measured all the spin, astrometric and binary parameters for these systems, to be consistent with the published results and in many cases improved. Finally, for some cases a PK parameter has been measured to be either consistent with the published value or even for the first time (e.g. PSR J0613−0200, PSR J0751+1807and PSR J1623−2631).

We have shown that at least 11 of the analysed ms pulsars can be good candidates for the EPTA efforts in detecting the stochastic background of gravitational radiation. With the new calibration procedures we achieved a post-fit rms below 10μs for all these sources and below 5μs for eight of them. Work is in progress for combination of the datasets from all the EPTA telescopes for all of these sources, which will improve the current measurements and takes us closer to the desired detection limit.

5. Bursting Neutron Stars

What is now proved was once only imagined.

William Blake

In this chapter the work done on slowly rotating neutron stars will be described. The major part of the work, about the Anomalous X-ray Pulsar (AXP) J1810-197, will be presented in the first section and can also be found in Lazaridis et al. (2008). In the second section a summary of Serylak et al. (2009) will be given, on the analysis of its single pulse properties.

5.1 Radio spectrum of the AXP J1810-197 and of its profile components

As part of a European Pulsar Network (EPN) multi-telescope observing campaign, we performed simultaneous multi-frequency observations at 1.4, 4.9 and 8.4 GHz during July 2006 and quasi-simultaneous multi-frequency observations from December 2006 until July 2007 at 2.7, 4.9, 8.4, 14.6, 32 and 43 GHz, in order to obtain flux density measurements and spectral features of the 5.5-sec radio-emitting magnetar AXP J1810$-$197. We monitored the spectral evolution of its pulse shape which consists of a main pulse (MP) and an interpulse (IP). We present the flux density spectrum of the average profile and of the separate pulse components of this first-known radio-emitting transient anomalous X-ray pulsar. We observe a decrease of the flux density by a factor of 10 within 8 months and follow the disappearance of one of the two main components. Although the spectrum is generally flat, we observe large fluctuations of the spectral index with time. For that reason we have made some measurements of modulation indices for individual pulses in order to also investigate the origin of these fluctuations.

5.1.1 Introduction

The AXP XTE J1810$-$197 was discovered by Ibrahim et al. (2004) in Rossi X-ray Timing Explorer (RXTE) data of the source SGR 1806$-$20, taken in January 2003. With a period of 5.54 seconds and a period derivative $\sim 1.15 \times 10^{-11} \, \mathrm{s s}^{-1}$, a magnetic field of $\sim 2.6 \times 10^{14}$ Gauss is implied. Although the previous observations clearly identified it as an AXP, the extreme variation in the X-ray flux also classified it as the first transient AXP.

The detection of a radio source coincident with the position of AXP J1810$-$197 by Halpern et al. (2005) raised the possibility that this was the first radio emitting magnetar. This was confirmed with the detection of strong, narrow and highly variable radio pulses, with the same

pulse period as determined at high-energies, by Camilo et al. (2006). For a dispersion measure of DM=178 ± 5 cm^{-3}pc a distance of d~ 3.3 kpc was also derived, using a model for the Galactic free electron distribution Cordes & Lazio (2002). Furthermore, timing measurements of period and $\dot{P}$ and mass estimations excluded the possibility of a companion to the source. Further observations have shown that the emission is $\sim$80-95 per cent polarised, mostly linear, but with a significant degree of circular polarisation at all observed frequencies (Kramer et al. 2007; Camilo et al. 2007c). One of the most remarkable features of the radio emission from this source is its flat radio spectrum. Radio pulsars are normally characterised by the steepness of their spectrum ($\sim \nu^{-1.8}$) (Kramer et al. 1999a; Maron et al. 2000; Löhmer et al. 2008), which makes their detection at frequencies above 30 GHz very difficult. However, soon after the discovery of its radio emission, it became clear that AXP J1810$-$197 had a surprisingly flat radio spectrum $S \propto \nu^{-0.5}$ (Camilo et al. 2006, 2007b) and for a time became the brightest neutron star at frequencies greater than about 40 GHz. Strong variations in the pulsed intensity and the profile phase were visible in the initial observations (Camilo et al. 2007a), although it also became evident that the average pulsed flux density was decreasing with time.

5.1.2 Observations

The simultaneous observations were made using the Effelsberg radiotelescope of the Max-Planck Institute for Radioastronomy (MPIfR), Germany, the Lovell radiotelescope at Jodrell Bank observatory of the University of Manchester, UK and the Westerbork Synthesis Radio Telescope (WSRT) in the Netherlands. The quasi-simultaneous observations were made with the Effelsberg radiotelescope. In total there were 8 simultaneous multi-telescope multi-frequency sessions during July 2006 and 10 quasi-simultaneous multi-frequency between December 2006 and July 2007. For the latter sessions the new sub-reflector of the Effelsberg telescope was used. The integration time for every session depended on the observing frequency and the observational circumstances. In general, the time needed for 1.42, 2.64, 4.85 and 4.90 GHz was around 5-15 min, for 8.35 GHz around 20 min and for 14.6 and 32 GHz around 25-40 min. Details of the observing sessions are summarised in Tables 5.1 and 5.2. The observing and calibration procedures for all the telescopes were described in section 2.1.

5.1.3 Data analysis & results

Until August 2006, the integrated pulse profile of AXP J1810$-$197 consisted of two major features with a separation of ~ 4 seconds ($\sim 260°$), as described in Kramer et al. (2007). Following the same convention, we refer to them as the *main pulse* (MP, right feature in Figure 5.3a) and *interpulse* (IP, left feature in Figure 5.3a). The MP is the more complex and wider of the two, with a varying width of about 0.7 seconds (or 45 deg in pulse longitude) while the IP is much narrower with a width of typically 0.2 seconds (or 12 deg longitude). In some cases, three or more distinct sub-components were visible in the MP. The simpler IP was not always visible and was only strongly detected during parts of our observations, as indicated in Figure 5.2 where we present the daily average flux densities of the two components as measured at 8.4 GHz as a function of time. Timing analysis only with the Effelsberg observations, as described in section 2.2.2, to identify the remaining visible pulse feature (see e.g. Figure 5.3b) is not capable of producing any proper results. The reported parameters of P, $\dot{P}$, position and DM were used while during the fitting only the period and its derivative were allowed to vary while the rest held fixed. The failure of this timing effort is caused by the intense phase changes of the source,

Table 5.1: **Summary of simultaneous observing sessions in July 2006.**

| Date	Session	Telescope	Frequency (GHz)	BW (MHz)
31/05/06	1	Lovell	1.42	32
		WSRT	4.90	160
		Effelsberg	8.35	1000
10/07/06	2	Lovell	1.42	32
		Effelsberg	8.35	1000
17/07/06	3	Lovell	1.42	32
		WSRT	4.90	160
		Effelsberg	8.35	1000
21/07/06	4	Lovell	1.42	32
		WSRT	4.90	160
22/07/06	5	Lovell	1.42	32
		WSRT	4.90	160
		Effelsberg	8.35	1000
		Effelsberg	14.60	2000
23/07/06	6	Lovell	1.42	32
		WSRT	4.90	160
26/07/06	7	Lovell	1.42	32
		Effelsberg	4.85	500
		WSRT	4.90	160
		Effelsberg	8.35	1000
		Effelsberg	14.60	2000
28/07/06	8	Lovell	1.42	32
		Effelsberg	4.85	500
		WSRT	4.90	160
		Effelsberg	8.35	1000
		Effelsberg	14.60	2000

as can be seen in the post-fit in Figure 5.1. All the points in yellow are at 8.35 GHz and all the ones in green are at 14.6 GHz. In the July sessions both MP (points at zero phase) and IP (points at 0.3 phase) are visible, but we cannot say with certainty if the features appearing later are the MP or the IP. Finally, the identification of the remaining visible pulse feature with the MP is possible due to timing information obtained from regular monitoring observations with the Lovell telescope at the Jodrell Bank observatory (Lyne et al. in preparation). It is important to mention that phase changes of 20 per cent in the timescale of a day are not possible to emerge from effects intrinsic to the source. The difference of the spin down luminosity between the two days, if a spin up (or down) of the magnetar was happening, would be $\Delta \dot{E} = 2.8 \times 10^{33}$ erg s^{-1}, where $\dot{E} = 3.93 \times 10^{31}$ erg sec^{-1} $(\dot{P}/10^{-15})(P/\text{sec})^{-3}$ and we assumed a change of 1.14 sec in the period of the magnetar (0.2 of the phase). This is a strong hint that the variations are emerging from magnetospheric effects (twisted magnetosphere, look at the discussion). After the disappearance of the IP in summer 2006, both MP and IP were visible again simultaneously

Table 5.2: **Summary of quasi-simultaneous observing sessions from December 2006 to July 2007.**

Date	Session	Telescope	Frequency (GHz)	BW (MHz)
09/12/06	1	Effelsberg	2.64	100
			4.85	500
			8.35	1000
			14.60	2000
26/12/06	2	Effelsberg	2.64	100
			4.85	500
			8.35	1000
			14.60	2000
04/02/07	3	Effelsberg	2.64	100
			4.85	500
			8.35	1000
			14.60	2000
06/02/07	4	Effelsberg	4.85	500
			32.00	2000
12/02/07	5	Effelsberg	4.85	500
			14.60	2000
17/02/07	6	Effelsberg	4.85	500
			8.35	1000
			14.60	2000
			32.00	2000
18/02/07	7	Effelsberg	4.85	500
			8.35	1000
			14.60	2000
			32.00	2000
26/03/07	8	Effelsberg	4.85	500
			14.60	2000
			32.00	2000
05/05/07	9	Effelsberg	4.85	500
			8.35	1000
			32.00	2000
06/07/07	10	Effelsberg	4.85	500
			8.35	1000
			14.60	2000

only during one short session in May 2007. The IP remains undetected since.

Overall, the flux density of the source has significantly decreased since its first detection at radio frequencies (see Figure 5.2), which is consistent with the earlier findings by Camilo et al. (2007a). It was also not detected in an combined effort with Effelsberg and Nançay radiotelescope in March 2009. Due to differences in the frequency range of the simultaneous and quasi-simultaneous observations we discuss further results from these campaigns separately.
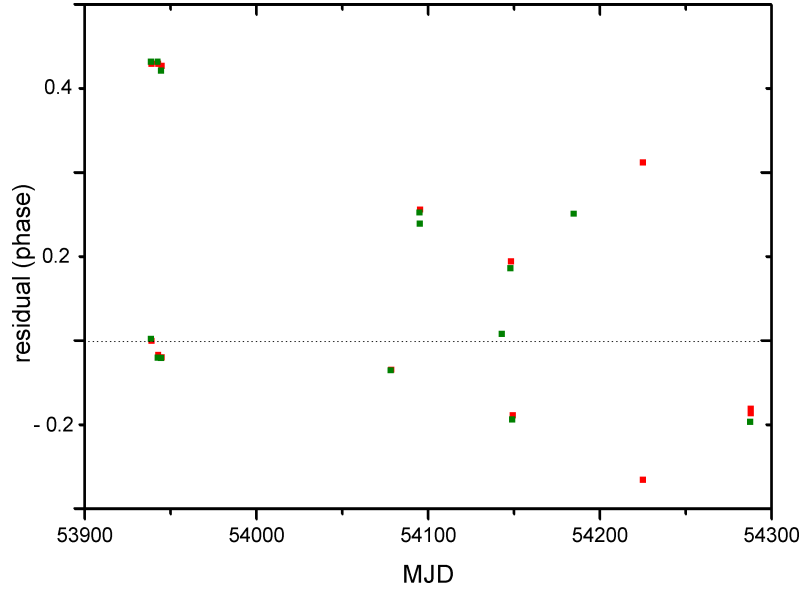
Figure 5.1: **The extreme phase changes of AXP J1810−197 from the Effelsberg timing solution. The red points are at 8.35 GHz and the green at 14.6 GHz.**
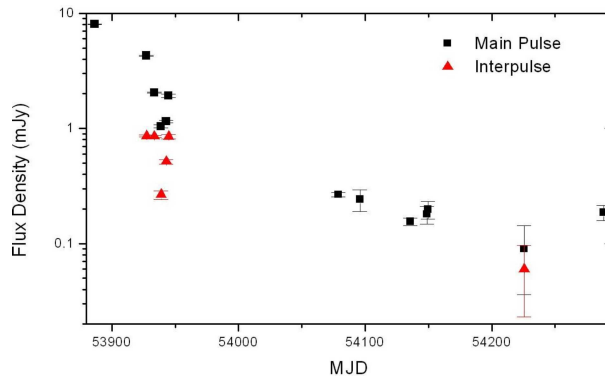
Figure 5.2: **The average flux density for each observing session as measured at 8.35 GHz for the main pulse and the interpulse (when detected).**

Simultaneous observations

The flux densities measured during the simultaneous observations and the spectral indices derived from power law fits, ($S \propto \nu^{\alpha}$) to these data, are listed in Table 5.3 and are shown in Figures 5.4 and 5.5. For each observation we summed all individual pulses to obtain an integrated total power profile that was flux calibrated. The Jodrell and WSRT data were average profiles in EPN format without explicit error information. In these cases it is customary to use an error of 10% as a conservative estimate (Kramer private communication). For Effelsberg measurements we used the normal calibration errors caused by the system noise. In addition to our flux densities, we also utilise published flux densities measured at 1.42 and 4.8 GHz with the VLA (Camilo et al. 2007b) and at 1.4 and 4.8 GHz at the Mount Pleasant observatory (Hotan et al. 2007) (see Fig. 5.4). Our flux densities observed for the MP at similar epochs for these frequencies are
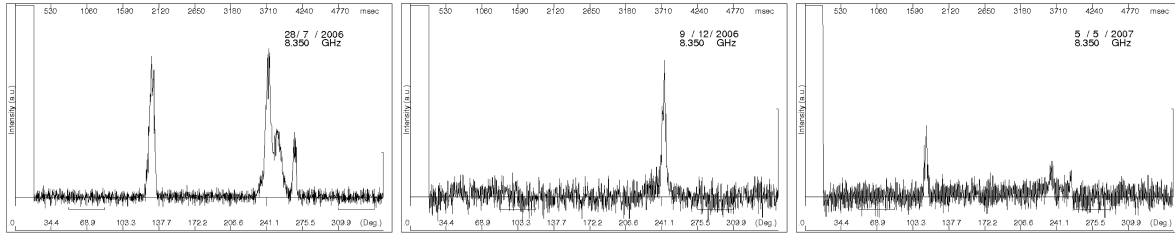
Figure 5.3: **Phase aligned integrated profiles of AXP J1810−197 in 2006 July (left), 2006 December (middle) and 2007 May (right). The source becomes significantly weaker while the IP eventually disappears. Only in 2007 May, both the MP and the IP are visible again. Note that each shown profile contains the signal of the calibrating noise diode which was switched on synchronously with the pulse period for the first 50 phase bins.**

in good agreement with these values. This indicates that the effect of interstellar scintillation may be small for the large observing bandwidths employed, but we will discuss the possible impact of the interstellar medium on our results in more detail later. Overall, a large decrease in the signal strength with time is observed. At the same time, the spectrum is generally flat with an average spectral index of $\alpha = -0.31 \pm 0.06$ for the MP and $\alpha = -0.41 \pm 0.21$ for the IP (see Figure 5.4 and 5.5), consistent with results by Camilo et al. (2006, 2007b). However, around MJD 53938 (2007 July 22) we observe a strong time variability, with the spectrum being initially steep and then flattening day by day for both MP and IP.

Quasi-Simultaneous observations

All quasi-simultaneous observations were performed with Effelsberg alone. The short time needed to switch between the different receivers (i.e. $\sim 30 - 60$s between secondary focus receivers, and $\sim 2 - 4$min between secondary and primary receivers) made it possible to observe at a wide range of frequencies in a single observing session. The longest multi-wavelength observing session (without counting the calibration scans) of AXP J1810−197 was about four hours, during which frequency bands were repeatedly cycled in order to detect any short-term variability. Using these data, we not only studied the long term variability of AXP J1810−197, but also the medium-term intra-day flux density fluctuations as well as the modulation of individual pulses during the sessions. An example of such measurements is shown in Figure 5.6 where we present the flux density as measured repeatedly at 4.85 GHz over two consecutive days. The observed variation is consistent with a constant flux density over this period. The results of all our quasi-simultaneous observations are summarised in Table 5.5.

The average flux density values were then used to determine the spectra and their indices. This was done for each session and the results are shown in Figure 5.7. The results are consistent with and extend those of the simultaneous measurements. We find again that the spectrum is generally flat with a mean spectral index of $\alpha = 0.00 \pm 0.09$ but it is also variable on a day-to-day basis with significant variations around its mean value. This is reflected also by the variation of the flux densities measured at 8.35 GHz and above which appear to sometimes follow a common pattern that is anti-correlated with changes seen below that frequency. There is an indication of a general increase of α over the 210 days covered by our observations, starting with initial values around $\alpha \sim -0.2$ and reaching $\alpha \sim 1.2$ near the end of the observing period.

Table 5.3: **Summary of flux densities and spectral indices for the main pulse.**

Date	Frequency (GHz)	S_m (mJy)	α
31/05/06	1.42	8.23 ± 0.82	$+0.01 \pm 0.11$
	4.90	9.73 ± 0.97	
	8.35	8.03 ± 0.01	
10/07/06	1.42	6.90 ± 0.69	-0.27 ± 0.06
	8.35	4.28 ± 0.03	
17/07/06	1.42	6.06 ± 0.61	-0.64 ± 0.14
	4.90	2.27 ± 0.23	
	8.35	2.05 ± 0.03	
21/07/06	1.42	2.14 ± 0.21	-0.33 ± 0.11
	4.90	1.42 ± 0.14	
22/07/06	1.42	2.59 ± 0.26	-0.79 ± 0.30
	8.35	1.04 ± 0.03	
	14.60	0.33 ± 0.03	
23/07/06	1.42	3.24 ± 0.32	-0.55 ± 0.11
	4.90	1.61 ± 0.16	
26/07/06	1.42	0.99 ± 0.10	-0.03 ± 0.11
	4.85	1.40 ± 0.03	
	4.90	0.86 ± 0.09	
	8.35	1.15 ± 0.03	
	14.60	1.06 ± 0.04	
28/07/06	1.42	1.32 ± 0.13	$+0.15 \pm 0.28$
	4.85	1.66 ± 0.03	
	4.90	0.65 ± 0.06	
	8.35	1.92 ± 0.07	
	14.60	1.70 ± 0.04	

Modulation indices

In order to characterise the observed flux density variations and to obtain reliable estimates for the measurement uncertainties, we also studied the modulation of the *single pulse* flux densities (see e.g. Kramer et al. (2003)). We can use these results also to estimate the impact of the interstellar medium on our measurements, following similar studies such as that conducted for pulsars by Malofeev et al. (1996) at very similar frequencies, i.e. 4.75 GHz and 10.55 GHz.

We concentrate on the flux densities measured at 4.85 GHz and 14.6 GHz during our quasi-simultaneous sessions. The flux densities at these frequencies were measured in every session, often at the beginning and the end of a session, providing a densely sampled data set that gives a good representation of the behaviour between widely spaced frequencies.

In Figure 5.8 the variability of the normalised flux density of single pulses of AXP J1810-197 is presented for one day at 4.85 and 14.6 GHz, where we show only values with S/N above $4\,\sigma$. As a comparison, we also studied data for our reference source PSR B1929+10 to rule

Table 5.4: **Summary of flux densities and spectral indices for the interpulse.**

Date	Frequency (GHz)	S_m (mJy)	α
10/07/06	8.35	0.86 ± 0.02	-
17/07/06	1.42	0.13 ± 0.01	$+1.12 \pm 0.33$
	4.90	0.83 ± 0.08	
	8.35	0.86 ± 0.02	
21/07/06	4.90	0.44 ± 0.04	-
22/07/06	4.90	0.58 ± 0.06	-1.61 ± 0.08
	8.35	0.27 ± 0.02	
	14.60	0.10 ± 0.04	
23/07/06	4.90	0.58 ± 0.06	-
26/07/06	4.85	0.81 ± 0.02	-1.29 ± 0.26
	8.35	0.51 ± 0.02	
	14.60	0.19 ± 0.03	
28/07/06	1.42	0.49 ± 0.05	$+0.15 \pm 0.28$
	4.85	0.42 ± 0.02	
	4.90	0.28 ± 0.03	
	8.35	0.85 ± 0.04	
	14.60	0.58 ± 0.03	

out systematic effects, impact of weather, or instabilities in the receivers chain. We find, as expected, only minor variations in the flux density of this well known pulsar at high frequencies, in line with the findings of Malofeev et al. (1996).

For each session, we calculated the pulse-to-pulse modulation index m according to $m^2 = \frac{\langle (S - \langle S \rangle)^2 \rangle}{\langle S \rangle^2} = \sigma_S^2 / < S >^2$ (e.g. Kramer et al. 2003), where S is the measured flux density, $\langle S \rangle$ its mean value and σ_S its standard deviation. We present the results in Figure 5.9. As already expected from the discussion in Kramer et al. (2007) and consistent with early observations of AXP J1810−197 by Camilo et al. (2006), the pulses are very highly modulated and variable for both frequencies. For the densely covered period of time around epoch MJD 54150 (04 February-26 March 2007) the data occasionally suggest a behaviour that is anti-correlated between 4.85 GHz and 14.6 GHz. Overall, the higher frequency shows greater modulation, but it is possible that weaker single pulses are more difficult to detect at these frequencies. Despite the large modulation of the single pulses, averaging over sufficient time as done for all our observations essentially removes the variation for a given measurement, leading to relative uncertainties in S of the order $m/\sqrt{n}$ where n is the number of averaged pulses. This is consistent with our estimated flux density errors and confirmed by the repeatability of our flux density measurements over consecutive days (see Figure 5.6). We therefore expect the impact of slow-varying effects caused by refractive scintillation to be more important, as will be shown in the discussion below.
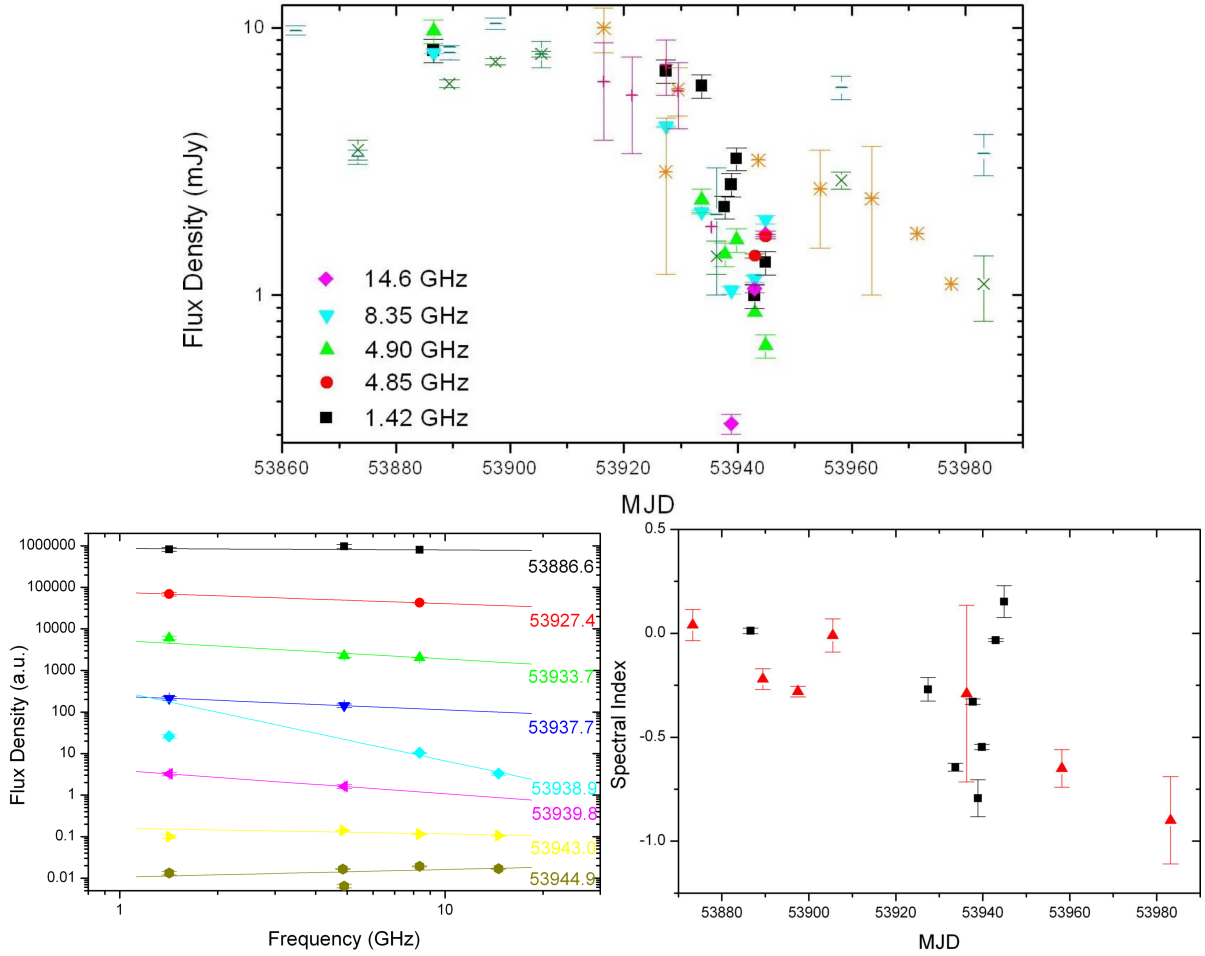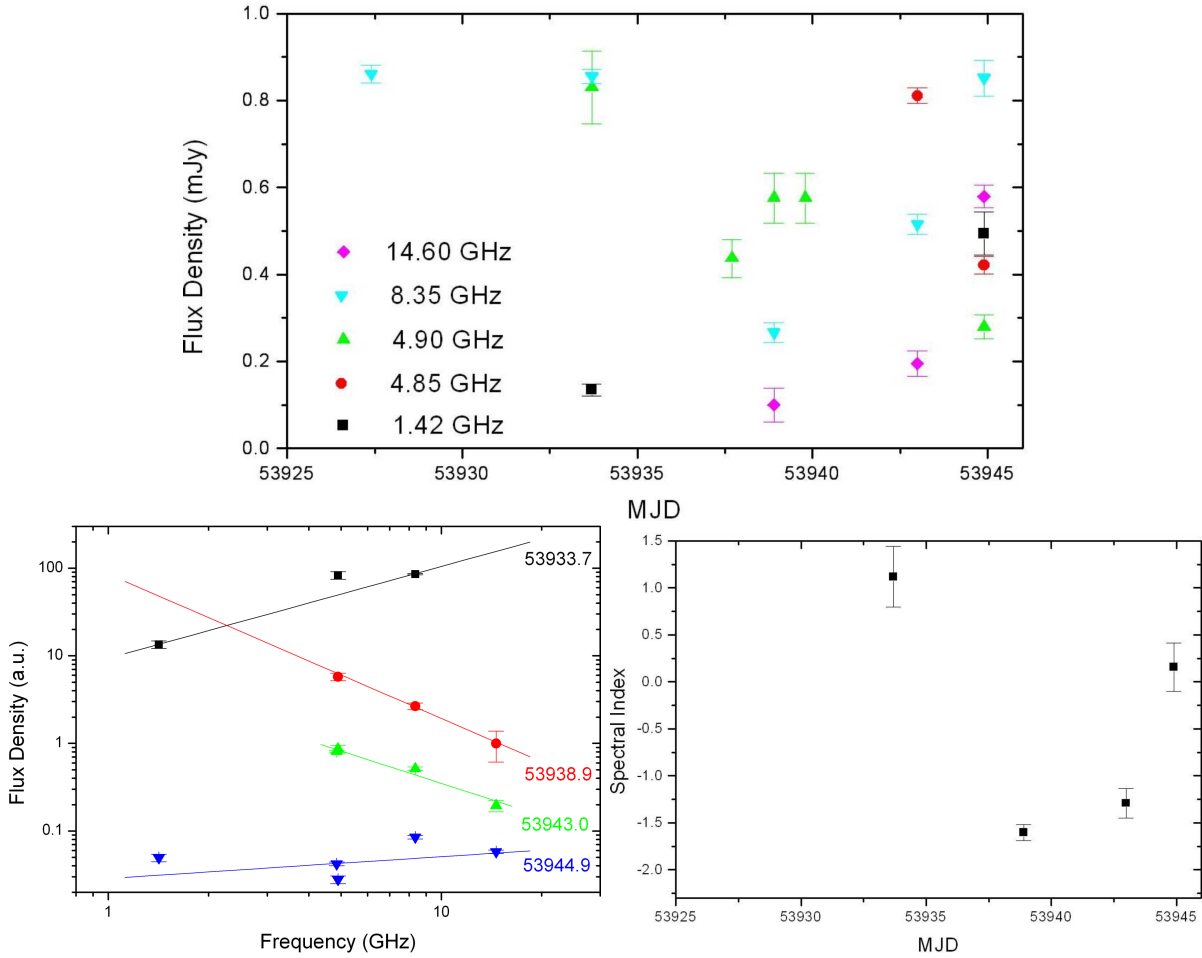
Figure 5.4: **(Top) Flux density and its variability as measured at various frequencies as a function of time. We also added data measured by Hotan et al. (2007) at 1.4 and 4.8 GHz (shown as crosses and stars, respectively) and Camilo et al. (2007c) at 1.42 and 4.8 GHz (shown as bars and exes, respectively). (Bottom) (Left) Flux density spectrum of the MP as determined during our simultaneous observations. For plotting purposes the flux densities of each day were multiplied by a different factor to distinguish the dates more clearly. (Right) Derived spectral indices of the MP as a function of time. The average value is determined $\alpha = -0.31 \pm 0.06$. In comparison, we show spectral indices derived by Camilo et al. (2007c) from VLA measurements as triangles.**

5.1.4 Discussion

Our monitoring observations of AXP J1810−197 and its flux density spectrum over the course of more than one year appears to confirm the earlier conclusion, that AXP J1810−197 behaves unlike any known radio pulsar. Several observed properties support this fact. In our range of studied frequencies, the source exhibits a generally flat flux density spectrum, with values of spectral index consistent with those measured by Camilo et al. (2006, 2007b). These flat spectra allowed us to observe the source up to very high frequencies. An example is our detection of the magnetar at 43 GHz in May 2007 with the Effelsberg radiotelescope (Figure 5.10). This is only the fifth neutron star detected at λ7mm (Kramer et al. 1997) and the only one where single pulses could be observed. Our result is also consistent with observations at the IRAM 30m telescope

Figure 5.5: **(Top) Flux density and its variability as measured at various frequencies as a function of time. (Bottom) (Left) Flux density spectrum of the IP as determined during our simultaneous observations. For plotting purposes the flux densities of each day were multiplied by a different factor to distinguish the dates more clearly. (Right) Derived spectral indices of the IP as a function oft time. The average value is determined $\alpha = -0.41 \pm 0.21$.**

at 88 and 144 GHz by Camilo et al. (2007b), representing the highest radio frequency at which a neutron star has been detected. For normal pulsars, we often see breaks in their power law spectra at high frequencies (Maron et al. 2000; Kijak et al. 2007) or even occasionally a turn-up at mm-wavelengths (Kramer et al. 1997). However, in our range of frequencies, the spectrum of AXP J1810−197 is well described by just a single, flat power law, of the form $S_\nu \propto \nu^\alpha$ with $\alpha = 0.0 \pm 0.5$.

In those cases where both the MP and IP were detected, their spectral indices were found to be differing slightly, with the IP showing a significantly greater variation. Even though the spectra appear to change in the same manner from day to day, becoming steeper or flatter together, the IP exhibited many more extreme positive and negative steepness values. This is somewhat surprising since the MP spectral index reflects emission from a wider range of emission components, in comparison to an IP that is always observed as a rather simple emission feature. The variation of the spectrum is roughly consistent with the model by Thompson
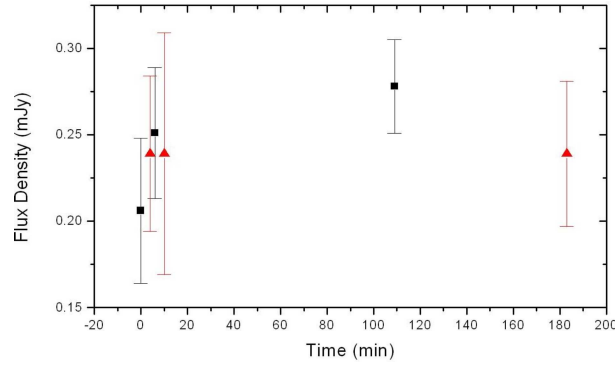
Figure 5.6: **Flux density measured at 4.85 GHz during an observing session for two consecutive days (square and up triangle points). The first two measurements for each day correspond to a 5 minutes integration time while the third measurement corresponds to 15 minutes.**

(2008a) where timescales of ~ 0.1 day may be explained by current-driven instabilities on the closed magnetic field lines. The observation that it affects the IP and MP in a different way is interesting and may support the idea of a rather twisted magnetosphere. Although the spectrum is generally flat, the spectral index shows significant variation, with a slight trend of becoming more positive with time.

While we have shown that the effect of the significant pulse-to-pulse modulation can be removed by averaging a sufficient number of pulses, another well known cause for flux density variations, and hence possible spectral index variations, is interstellar scintillations (ISS). Based on studies of the ISS at 4.75 GHz and 10.55 GHz by Malofeev et al. (1996), the relatively large dispersion measure of DM = $178\,\mathrm{pc\,cm^{-3}}$ and the estimated distance of 3.3 kpc, suggests a critical scintillation frequency f_c of $\sim$14 GHz, well within our observing band at 14.6 GHz. At this frequency, we may therefore expect a large variation of the measured flux density, whereas above the critical frequency we expect low flux density variations as a result of weak scintillation. Below f_c strong scintillation will occur, with a branch caused by diffractive scintillation and one caused by refractive scintillation. Lorimer & Kramer (2005) use a different functional dependence for the transition frequency which yields an $f_c \simeq 60$ GHz which agrees with the estimates by Camilo et al. (2007b) but is also smaller than $f_c \simeq 140$ GHz as derived from the NE2001 electron density model (Cordes & Lazio 2002). Despite these differences, the usage of large integration times and observing bandwidths will effectively average a number of scintils, resulting in reliable flux density measurements if bandwidth and integration time are sufficiently large. Following Lorimer & Kramer (2005), at 15 GHz we estimate a diffractive scintillation bandwidth $\Delta\nu_d = 320$ MHz and a diffractive scintillation timescale of $t_d = 600\,\mathrm{s}$ which is in good agreement with the characteristics of features seen in the dynamic spectrum at the same frequency by Ransom et al. (2007). Our observations always average over several diffractive scintles in frequency and in time, but will be affected by refractive scintillations at high frequencies. Around 15 GHz, the modulation index for refractive scintillations is estimated as $m_r = 0.6$ and the timescale for refractive modulations turns out to be $t_r = 12.8$ hours. Our observatories could not track the source for such a long time, so that we account for these possible variations with an increased quoted flux density error. For typical integration times of $t_{int} = 40\,\mathrm{min}$, our observing set-up should result in typical errors of our individual flux density measurements due to refractive and diffractive scintillations of about 20 per cent at 1.4 GHz,

Table 5.5: **Summary of flux densities and spectral indices for the MP measured during our quasi-simultaneous observing sessions.**

Date	Frequency (GHz)	S_m (mJy)	α
09/12/06	2.64	0.39 ± 0.05	-0.35 ± 0.11
	4.85	0.40 ± 0.03	
	8.35	0.27 ± 0.01	
	14.60	0.23 ± 0.03	
26/12/06	2.64	0.56 ± 0.09	-0.67 ± 0.17
	4.85	0.25 ± 0.05	
	8.35	0.24 ± 0.05	
	14.60	0.16 ± 0.01	
04/02/07	2.64	0.55 ± 0.08	-0.24 ± 0.49
	4.85	0.15 ± 0.05	
	8.35	0.15 ± 0.01	
	14.60	0.36 ± 0.03	
06/02/07	4.85	0.20 ± 0.05	-0.18 ± 0.25
	32.00	0.14 ± 0.06	
12/02/07	4.85	0.20 ± 0.03	$+0.11 \pm 0.15$
	14.60	0.22 ± 0.02	
17/02/07	4.85	0.24 ± 0.02	$+0.06 \pm 0.13$
	8.35	0.18 ± 0.03	
	14.60	0.23 ± 0.01	
	32.00	0.25 ± 0.05	
18/02/07	4.85	0.24 ± 0.03	$+0.03 \pm 0.08$
	8.35	0.20 ± 0.03	
	14.60	0.21 ± 0.02	
	32.00	0.25 ± 0.06	
26/03/07	4.85	0.33 ± 0.03	-0.80 ± 0.17
	14.60	0.10 ± 0.02	
	32.00	0.08 ± 0.04	
05/05/07	4.85	0.09 ± 0.03	$+0.86 \pm 0.27$
	14.60	0.09 ± 0.05	
	32.00	0.42 ± 0.08	
06/07/07	4.85	0.15 ± 0.04	$+1.20 \pm 0.44$
	8.35	0.19 ± 0.03	
	14.60	0.55 ± 0.02	

rising to a maximum of 77 per cent at 14.6 GHz and levelling off at about 62 per cent at 33 GHz and above. Similar estimates for the low-DM reference source PSR B1929+10 are in good agreement with the observations. We therefore conclude that the ISS plays a significant role
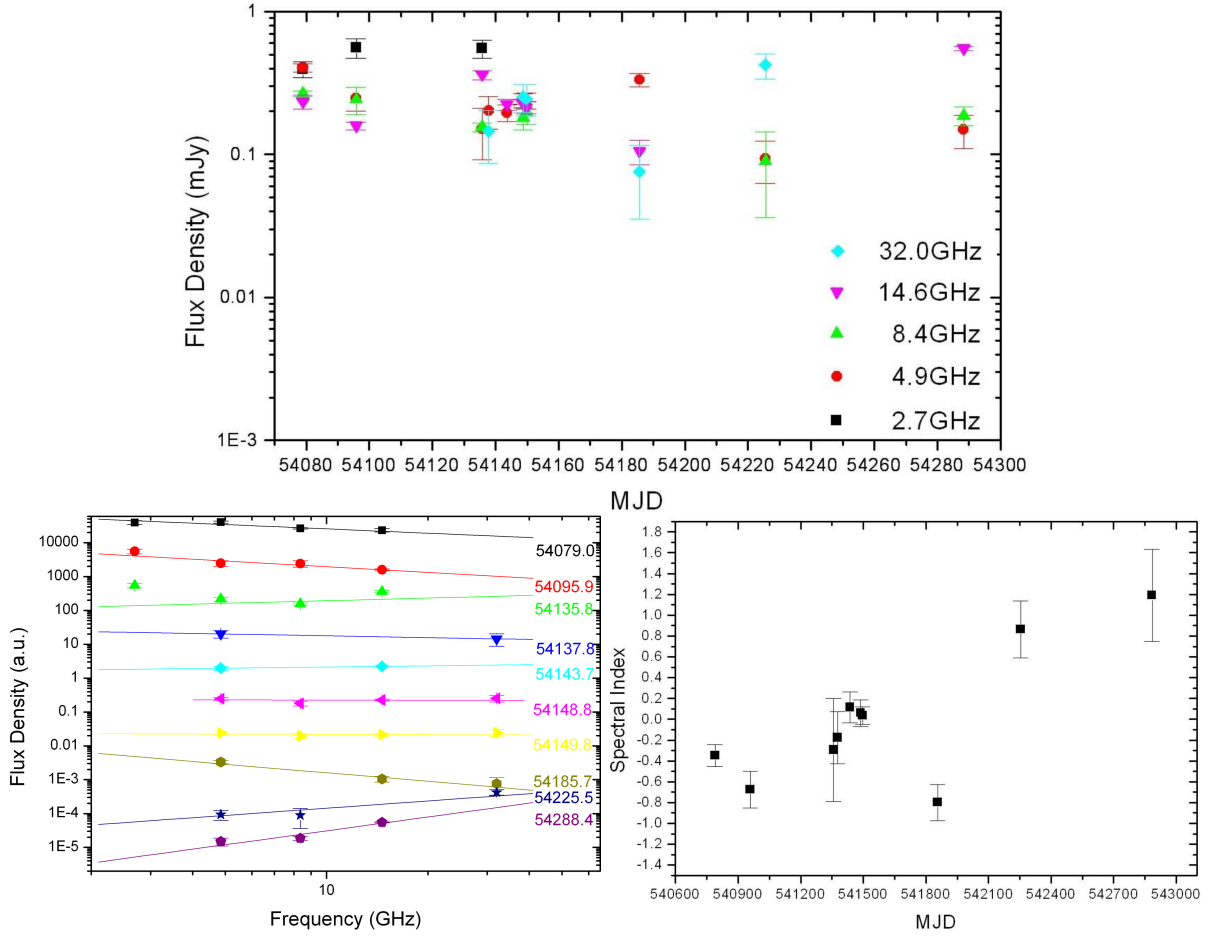
Figure 5.7: (Top) Flux density and its variability as measured at various frequencies as a function of time. (Bottom) (Left) Flux density spectrum of the MP as determined during our quasi-simultaneous observations. For plotting purposes the flux densities for each day were multiplied by a different factor to distinguish the dates more clearly. (Right) Derived spectral indices of the MP as a function oft time. The nominal average value is determined as $\alpha = -0.003 \pm 0.089$.

in the individual flux density measurements, although it cannot be responsible for the pulse-to-pulse modulation index, and the described variations of the spectral index for different features of the profile between individual sessions.

Considering the overall flux density of AXP J1810−197, we divide our observations, spanning more than a year, into four intervals. The first lasts until July 2006 when the average flux density from the source was above 6 mJy. The second lasted from July to September 2006 when the average flux density was above 1 mJy. The third epoch lasted from October 2006 to July 2007 when the flux density was below 0.5 mJy and, finally the time after July 2007 when the source became too weak for regular detection. At the same time, we observe a trend that the flux density variations become larger in the low-flux stages. Naturally the flux density spectrum computations are less certain.

Due to the variability of the flux densities, it is difficult to compute an average spectrum. Especially when we inspect the flux density measurements from the third epoch, we see many cases in which the high and the low frequencies vary in a completely different manner for the
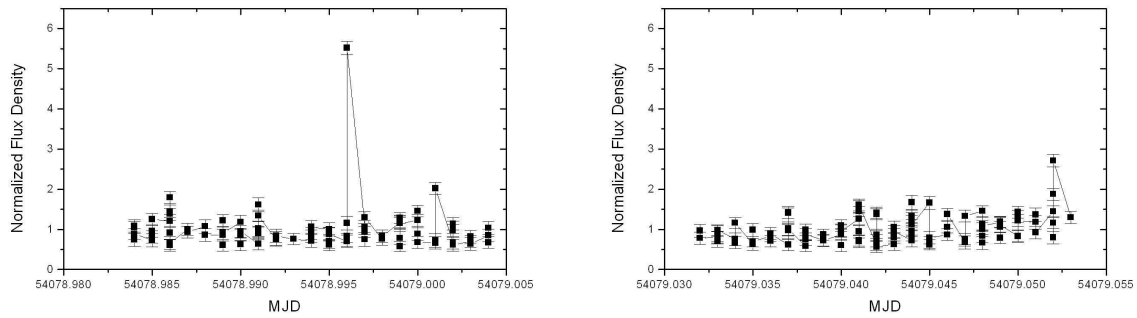
Figure 5.8: **The intra-day variability of the normalised flux density of individual pulses for 09/12/06, at 4.85 GHz (left) and 14.6 GHz (right).**
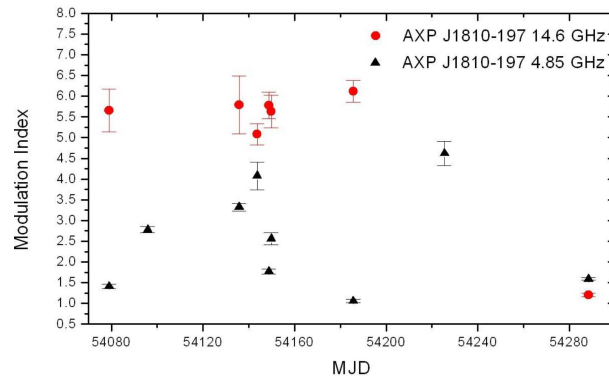
Figure 5.9: **Variation of the pulse-to-pulse modulation index of AXP J1810$-$197 at 4.85 GHz (squares) and 14.6 GHz (triangle). At 14.6 GHz the indices were computed for time series covering 25-30 min while the 4.85 GHz data cover 10-30 mins.**

same day. As we have seen, some anti-correlation in flux density variations between high and low frequencies appears present, and given our discussion above, we consider these variations to be intrinsic to the source and not due to ISS. They can in part be explained by the assumption that we observe different components of the MP on different days. However, a similar variation is also observed for the IP, where always the same emission component is visible. Therefore, we conclude that in contrast to pulsars, the radio emission of magnetars is not intrinsically stable. That is consistent with the overall decay of the flux density in recent months and may indicate that the radio emission is a transient phenomenon that was preceded the high-energy outburst. As the conditions for radio emission may revert back to the pre-outburst stage, it will be interesting to monitor the source during and after the next outburst. As part of this monitoring programme, Effelsberg and Nançay observed in March 2009 at two frequencies (8.35 and 1.4 GHz respectively) the magnetar, simultaneously with the XMM-Newton satellite, however no detection was achieved in radio.
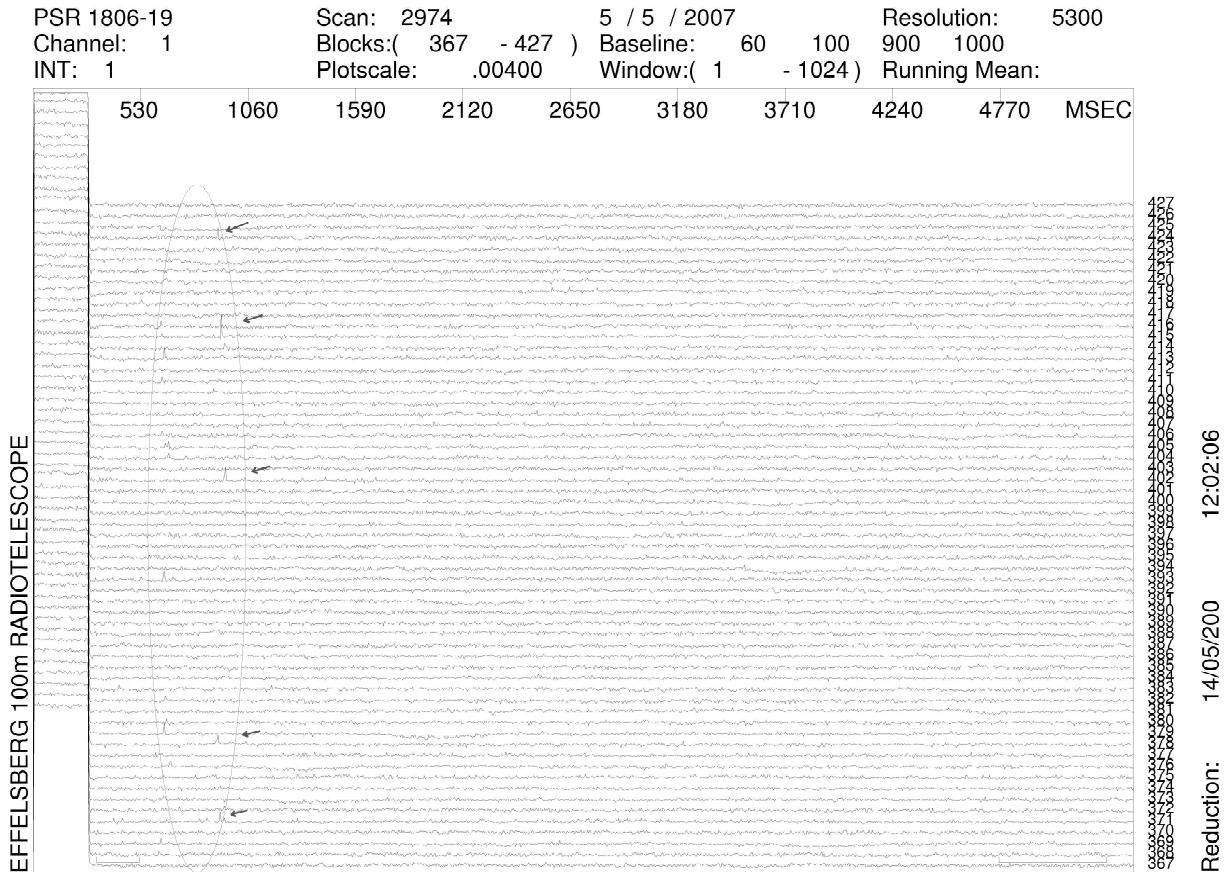
Figure 5.10: **Sequence of single pulses in May 2007 of AXP J1810−197. For the first time single pulses are observed at 43 GHz with Effelsberg. The detected single pulses are pointed with arrows. For the first 50 bins the calibration signal from the noise diode is on.**

5.2 Single pulse properties of AXP J1810-197

This section summarises the work of Serylak et al. (2009). Being the continuation of the polarisation and spectral properties of AXP J1810−197 (Kramer et al. 2007; Lazaridis et al. 2008) it is presented here for completeness.

We have used the Lovell, WSRT and Effelsberg radio telescopes to investigate the simultaneous single-pulse properties of the radio emitting magnetar AXP XTE J1810-197 at frequencies of 1.4, 4.8 and 8.35 GHz during May and July 2006. We study the magnetar's pulse-energy distributions which are found to be very peculiar as they are changing on time-scales of days and cannot be fit by a single statistical model. The magnetar exhibits very strong spiky sub-pulses, but they do not fit the definition of the giant pulse or giant micro-pulse phenomena. Measurements of the longitude-resolved modulation index reveal a high degree of intensity fluctuations on day-to-day time-scales and dramatic changes across pulse phase. We find that the frequency evolution of the modulation index values differs significantly from what is observed in normal radio pulsars. We do not identify any regular drifting sub-pulse phenomenon at any of the observed frequencies at any observing epoch. However, we discover a quasi-periodicity of the sub-pulses in the majority of the observing sessions. A correlation analysis indicates a relationship between components from different frequencies. We discuss the results of our analysis in

light of the emission properties of normal radio pulsars and a recently proposed model which takes radio emission from magnetars into consideration.

5.2.1   Data analysis

Observations of individual pulses from AXP J1810−197 allowed us to perform a variety of analysis techniques which are summarised below and are described in full in Serylak et al. (2009). The analysis was conducted at the frequencies of 1.4, 4.9 and 8.35 GHz (Lovell, WSRT and Effelsberg respectively) during 3 observing sessions in May and July 2006. Before performing the analysis, all data sets have been corrected for any RFI present and in the case of the Lovell and WSRT observations re-binning was applied to increase the S/N ratio and to match the 5.4 ms time resolution of the Effelsberg data set. For the current analysis the component classification used is presented in Figure 5.11, following the one from Kramer et al. (2007). In Table 5.6 all the observing sessions and the visible components on each are shown.
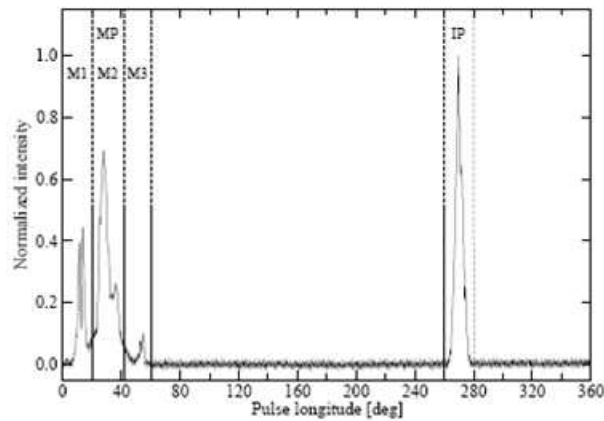
Figure 5.11: **The average pulse profile of AXP J1810−197 from the observation made with Effelsberg during session 3, showing component designations from Kramer et al. (2007).**

Table 5.6: **Summary of observing sessions.**

Session	Date MJD/dd.mm.yy	Telescope	Frequency (GHz)	Total number of pulses	Component presence
1	53886/31/05/06	Lovell	1.42	2101	M1 M2 – –
		WSRT	4.90	2151	M1 M2 M3 –
		Effelsberg	8.35	972	M1 M2 M3 –
2	53926/10/07/06	Lovell	1.42	1947	M1 M2 – –
		Effelsberg	8.35	2583	M1 M2 M3 IP
3	53933/17/07/06	Lovell	1.42	2275	M1 M2 M3 IP
		WSRT	4.90	3855	M1 M2 – IP
		Effelsberg	8.35	2454	M1 M2 M3 IP

The initial part of the current analysis is on the shape and stability of the pulse profile. This procedure demands the inspection of the sequences of individual pulses of all data sets. While

performing this we easily noticed that the sub-pulses are much narrower than the width of the average profile and appear at the longitude ranges which correspond to different components. Also, it is worth noticing, that the sub-pulses associated with M1 are stronger than the rest of the MP components, at all the frequencies and epochs, except the Effelsberg data set in session 3 where M2 becomes the strongest component. The strong and spiky sub-pulses tend to be separated by $\sim 4\,deg$ ($\sim 61\,ms$) throughout the data.

The second part of our investigation is the fluctuation analysis of the sub-pulses in order to identify the phenomenon of "drifting" (Drake & Craft 1968) and measure their modulation. The techniques used to investigate the sub-pulse drifting are known as the longitude-resolved fluctuation spectrum (LRFS; Backer (1970)) and two-dimensional fluctuation spectrum (2DFS; Edwards & Stappers (2002)). All the details of the aforementioned techniques and analysis can be found in Weltevrede et al. (2007). Briefly, in the fluctuation analysis an average profile from a pulse stack is being formed by vertically integrating each phase bin within the same longitude along consecutive pulses. In addition, the longitude-resolved modulation index (LRMI) is calculated as an indicator of the sub-pulse modulation. The modulation index is the LRMI m_i at the pulse longitude bin i where m_i has its minimum value (Weltevrede et al. 2007). In order to investigate whether this modulation is systematic the 2DFS has to be calculated. This is actually done by dividing the pulse stack into blocks of 512 pulses and applying the discrete Fourier Transformation along lines with different slopes in the pulse stack. As mentioned in the next subsection, we do not identify sub-pulse drifting in any of the sessions, however the values of the LRMI are quite high and the intensity fluctuations happen over short periods of time, even within the same session.

In the third part of the single pulse analysis we study the pulse-amplitude characteristics of AXP J1810$-$197. In order to accomplish that we have made pulse-energy distributions for all frequencies and epochs for both MP and IP. Then, for each of the components of the MP and for the IP we fit their pulse-energy distributions with two well known models. For the spiky giant-like sub-pulses we used power law statistics to model this behaviour (Lundgren et al. 1995a) and for the "normal" pulses the lognormal statistic as discussed by Cairns et al. (2001):

$$P_{powerlaw}(E) \propto E^p, \qquad\qquad (5.1)$$

$$P_{lognormal} = \frac{<E>}{\sqrt{2\pi}\sigma E} \exp[-\frac{(ln\frac{E}{<E>} - \mu)^2}{2\sigma^2}] \qquad\qquad (5.2)$$

In general it is not possible to fit the distributions well with a single model. An example is shown in Figure 5.12 where the components of the MP region are compared for session 1. In this session, only the M1 from the Lovell and WSRT data sets is best fit by lognormal pulse-energy distributions (equation (5.2)). The remaining components and the 8.35 GHz Effelsberg data sets follow power-law-like statistics (equation (5.1)).

The last part of our analysis is the single pulse correlation. Before the analysis all the pulse arrival times have been corrected to a common reference frame, as described in section 2.3.2. Then the times of the pulses were transferred to the SSB and the overlapping data sets at the different frequency pairs were taken for alignment, by comparing the TOAs of the pulses. Each data set was aligned in time with a one phase bin accuracy for each frequency pair. With the time resolution of 5.4 ms, the data sets were sufficiently aligned and all the telescope-specific delays were negligible. We used two techniques of single pulse correlation, the longitude-resolved linear correlation (LRLC) and the longitude-resolved cross-correlation (LRCC), for checking the linear dependency of intensity variations of individual pulses at different frequencies and
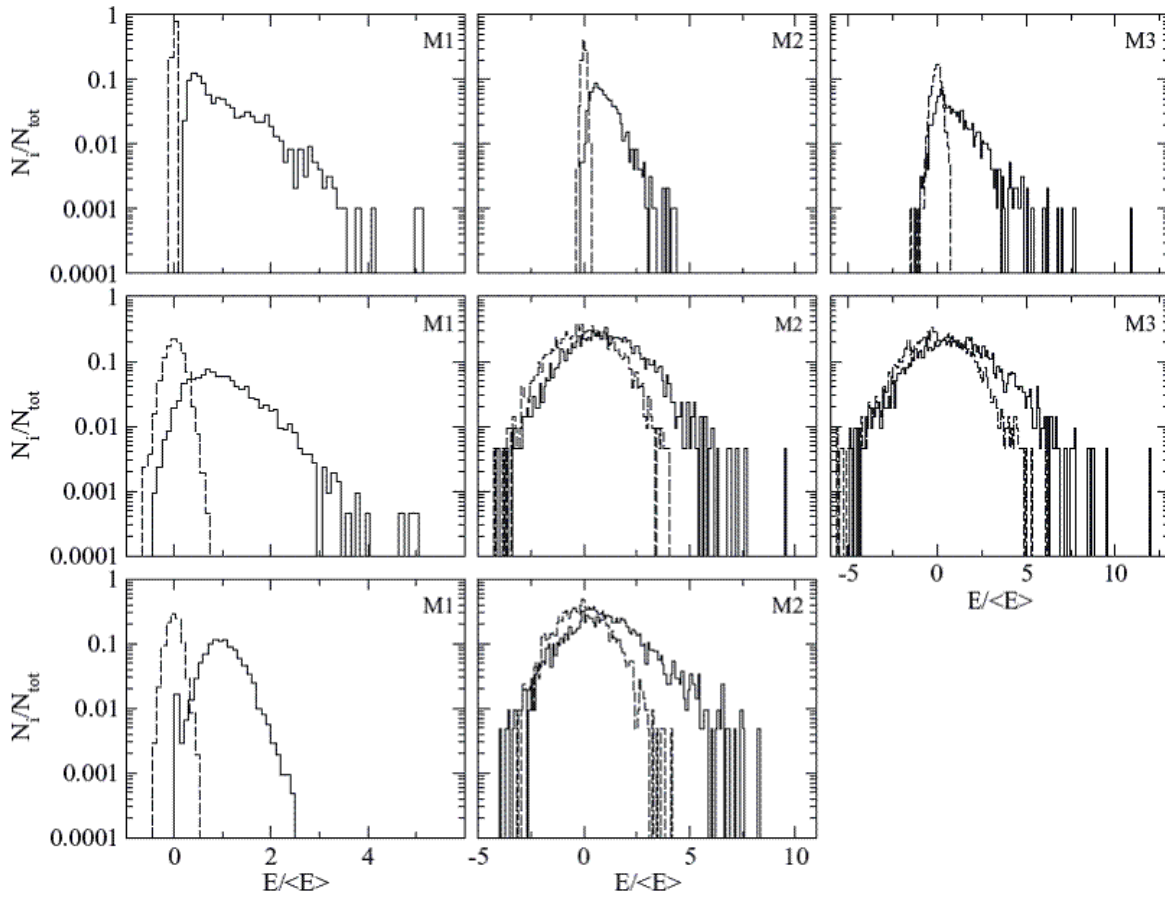
Figure 5.12: **Pulse energy distributions of the MP for the first session. From top to bottom, 8.35 GHz Effelsberg, 4.9 GHz WSRT and 1.4 GHz Lovell. Comparison of the components of the MP. From left to right, M1, M2 and M3. The horizontal axis denote energies normalised and scaled to the average pulse energy of the component. With dashed-lines the off-pulse-energy distributions of the components are shown.**

for getting information on the shape and the non-linear dependencies, respectively, as described in Serylak et al. (2009). We found that the linear correlation of M1 is always strong between all frequency pairs in contrast with M2. In addition the IP shows strong linear correlation. The cross-correlation is also strong in M1 while M2 and M3 are well correlated only between the 4.9 and 8.35 GHz data sets.

5.2.2 Discussion

All the phenomena revealed by the current analysis indicate that the radio emission of the AXP J1810−197 is clearly different to the known radio pulsar properties. Previous work, as presented also in the previous section, has shown many of the peculiarities of the radio emission from this magnetar (e.g flat spectral index, high degree of polarisation, long-term evolution of the polarisation angle swing with time; (Camilo et al. 2007b; Lazaridis et al. 2008; Camilo et al. 2007c; Kramer et al. 2007)). The results on single pulses presented in this work confirm that the mechanism responsible for the magnetar radio emission appears to have a different origin or perhaps even multiple origins, compared to the normal radio pulsars.

The modulation index changes dramatically from one component to another even within a single observing frequency and the magnitude of the values is close to the values reported for the Crab Pulsar (m = 5). This agrees with the conclusion that the infrequent occurrence of the strong sub-pulses with narrow widths and broad distribution of the sub-pulse intensities, results in the modulation index being on average significantly larger in AXP J1810−197. We must note, however, that in few cases, frequent occurrence of many strong and narrow sub-pulses with similar intensities at certain pulse phases of MP results in lower LRMI values. The lowest values of the modulation indices occur during session 1, but even in this session they increase with increasing frequency. Such behaviour is in contrast to the normal radio pulsars where the LRMI values from lower frequencies are on average higher than that at higher frequencies (Weltevrede et al. 2007). As we move in to session 2, the intensity fluctuations grow stronger with minimum modulation indices at values of around 4 for the 1.4 GHz Lovell data sets. For the 8.35 GHz Effelsberg data, we calculate the minimum modulation indices to be one in the MP and two in the IP region. It is remarkable, that for both data sets in this session the modulation indices in the MP peak at values of 7.5 and 10 for the Lovell and Effelsberg data, respectively. These values are extremely high and except for the Crab Pulsar, unprecedented in the results from modulation analysis from normal radio pulsars (Weltevrede et al. 2007). In session 3, for the 4.9 GHz WSRT data sets due to the low S/N ratio, the LRMI values are not sampled densely throughout the whole pulse profile range, but available values are comparable with session 1. The Lovell and Effelsberg LRMI values are similar to that of session 1. The longitude-resolved modulation analysis results presented above show the variation of the LRMI values on day-to-day time-scales and dramatic changes with pulse phase. In all sessions, we find the frequency evolution of the LRMI values in contradiction with properties of normal radio pulsars.

The following steps of our analysis, the 2DFS, do not show any regular drifting behaviour in any sessions or any frequencies. However, we find other phenomena manifesting which we interpret as the tendency of the sub-pulses to be equally separated in the consecutive pulses profiles throughout observation. Also in some cases (at 1.4 GHz Lovell, 4.9 GHz WSRT from session 1 and 8.35 GHz Effelsberg from session 3) the data sets are influenced by the baseline variations, which are obvious when checking the vertically collapsed 2DFS. The lack of regular drift from the magnetar might be associated with its rapidly changing emission properties and young age ($\tau < 10\,kyr$). In their work, Weltevrede et al. (2007) have shown that the fraction of young pulsars showing regular drifting is very low. Although, one could also argue that the strong radio variability might mask any regular structures or the physics of the magnetars radio emission is different from radio pulsars.

The high variability of the magnetar emission is also reflected in its pulse-energy distributions. For all sessions at all observed frequencies, we have made pulse-energy distributions for each of the MP component as well as for the IP (whenever present). We fit each of the pulse-energy distribution with models based on a power law or lognormal statistics for comparison between our observations and existing pulsar emission models. As justified later in this section, propagation effects in the interstellar medium are negligible for our data analysis and are therefore ignored. The significance of the best-fit models is low due to the oversimplified models, but mostly peculiar are the changes in the best-fit models of the components in different sessions. We interpret that as indicating the possible presence of multiple emission mechanisms with different statistical behaviour embedded in the same pulse phases.

In the case of AXP J1810−197, we see strong spiky sub-pulses which could be associated with the giant pulse phenomenon, but their widths are larger than that of giant pulses of

normal radio pulsars. Also, their occurrence, which covers the whole longitude range of that component, stands in contradiction to this definition. The most prominent example illustrating the above phenomenon in our observations is the first component, especially in the Effelsberg data sets from sessions 2 and 3. This component has many strong and spiky sub-pulses appearing within its whole longitude range, which dominates the high-energy tail in its pulse-energy distributions. This makes fitting the pulse-energy distributions with only one of the two considered laws impossible. A similar case occurs for PSR B0656+14 (Weltevrede et al. 2007), where weak emission is coupled with a component responsible for high energy bursts. In the case of AXP J1810$-$197, there may be more than two mechanisms contributing at one phase in the observed distributions. The magnetars very dynamic magnetosphere may be an explanation for such multicomponent pulse-energy distributions. This requires that the emission is in general broad-band, but the degree of variability can be very different. The components average together in pulse-energy distributions, which makes them difficult to fit properly using known statistical models.

Despite the changes in the pulse profile and pulse-amplitude characteristics on short time-scales, the correlation analysis gave results which contradict the overall picture of unstable emission from AXP J1810$-$197. The LRLC analysis shows significant correlation results in the majority of the frequency pairs used. The narrow and high correlation regions denote significant dependence between the intensities of the sub-pulses on small time- and spatial scales. The correlation always occurs between the first components in all of the analysed frequency pairs, with sporadic correlation between the third components. In contrast, the second component, which was found to be a stable emission region with lower modulation indices, was very weakly correlated. To examine the non-linear dependency between frequencies we used the LRCC method. The correlation is weaker when compared to the LRLC method, but correlated regions are also very narrow, showing that there are similarities in the phase and shape of the sub-pulses at different observed frequencies.

As presented in section 5.1.4, interstellar scintillation cannot be responsible for the variability over short time scales, which points that the origin of it must be intrinsic to the source. The lack of a regular drift, broad pulses, the presence of sub-pulses with quasi-periodic modulation, difficulties with fitting the data with single lognormal or power-law models allow us to draw a conclusion of non-stable emission due to the possible turbulent magnetar magnetosphere. As in the previous section the model better explaining that emission is the one by Thompson (2008a,b). In this work Thompson gives an extensive explanation of the pair creation processes in ultra strong magnetic field and particle heating in a dynamic magnetosphere. He considers the details of the QED processes that create electron-positron pairs in high magnetic fields of the order of 10^{14} G. He discusses the possibility of a strong enhancement of the pair creation rate in the open-field circuit and outer magnetosphere by instabilities near the light cylinder. He also refers to the flat radio spectra as a possible result of the high plasma density in the open magnetic field lines. One of the model explanations of the magnetar's broad pulse profile, is its beam geometry. In normal radio pulsars, wide pulse profiles are usually caused by the alignment between rotation and magnetic pole axis. The line of sight of the observer stays within the emission beam for a large fraction of the pulse period resulting in the long duty cycle. In the case of AXP J1810$-$197, the solution of fitting the position angle swing with the Rotating Vector Model (Radhakrishnan & Cooke 1969) results in non-aligned geometry ($\alpha = 44°, \beta = 39°$), but the beam radius inferred from the MP has a width of about $\rho \sim 44°$ as shown by Kramer et al. (2007). This result excludes viewing geometry as a reason for a wide pulse profile in

AXP J1810−197 . The model of the dynamic outer magnetosphere has a promising application in explaining the radio emission from the magnetars and is consistent with the magnetars emission features such as flat radio spectra, broad pulses and rapid variability.

Another suggestion for the AXP J1810−197 is the relation with RRATs. The detection of the periodic X-ray pulsations from RRAT J1819-1458 aligned with the radio bursts by McLaughlin et al. (2007) was the first time there was a comparison of its X-ray emission properties with AXP J1810−197 and excluded a close relationship with this specific RRAT. However, a link between magnetars and RRATs is still under investigation.

A. Appendix

A.1   Effelsberg observing system

In here a brief description and some useful technical information are provided about the basic pulsar observing systems at the Effelsberg radiotelescope (Jessner 2007).

A.1.1   EPOS

The Effelsberg Pulsar Observation System (EPOS) is used in Effelsberg since 1988. In its synchronous observing mode we use four Voltage-to-frequency (V/f) inputs of the Pulsar backend connected to a patchboard to acquire data from the,
1) broadband polarimeters built into the receivers in the telescope with Bandwidth (BW) 0.2-2 GHz
2) narrow-band polarimeter with BW < 200 MHz
3) pulsar de-disperser, 4×40 MHz BW in 60 channels of 0.666 MHz
4) polarisations $\times$ 8 $\times$ 60 = 480 MHz filter-bank
5) polarisations $\times$ 8 $\times$ 4 = 32 MHz filter-bank
as shown in Figure A.1. The unit named PUB86 is a fast data acquisition device with 4 input
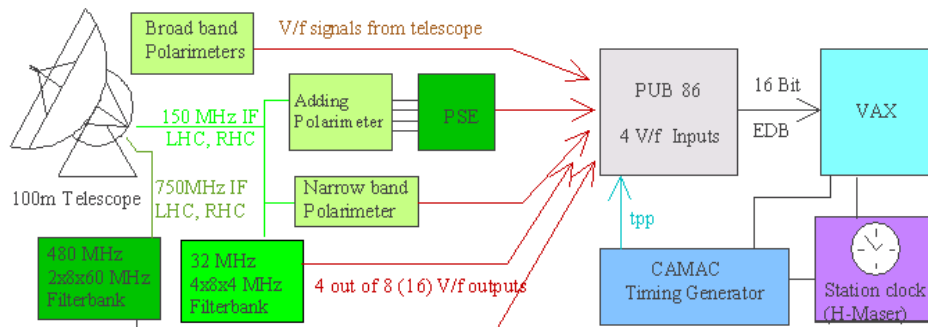
Figure A.1: **The Effelsberg Pulsar Observing System (EPOS) where all the input signals to the PUB 86 are shown.**

channels. Its timing is controlled by a signal synchronous with the pulsar period that defines the beginning of the measurement window. Pulsar periods from 1.024 ms to about 10000 s are possible and sampling intervals (phase bins) range from 1 μsec to 4096 μsec. 1024 samples can be stored per pulsar period and synchronously integrated over 1 to 65535 periods, before the data are transferred to the main computer system.

Most of Effelsberg receivers have two or more channels and can be used for polarisation measurements. By supplying the Intermediate Frequency (IF)-polarimeters with the 2 initial circularly polarised channels (LHC and RHC) we can finally calculate (after calibration in the EPOS) the Stokes parameters (A.2).
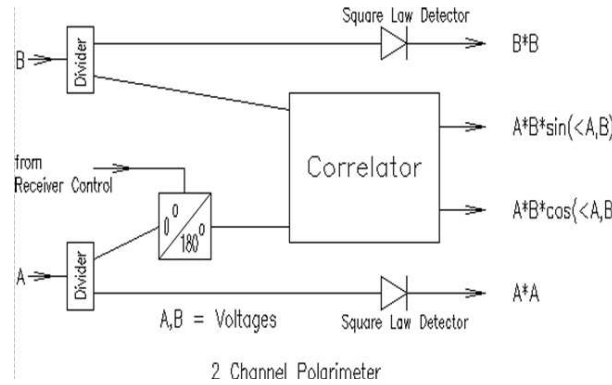
Figure A.2: **The IF-polarimeters where the LHC and RHC polarisation signals enter from the receiver, they are being correlated and polarisation measurements are being acquired.**

One of the most important parts of EPOS is the PSE, the incoherent de-disperser. In general, initially the incoming frequency band is split into a large number of independent frequency channels. Then, we apply to each channel appropriate time delays at the same time and finally we add the frequency channels together to get the de-dispersed signal. The PSE is presented in Figure A.3. Following the numbers on this figure we have in 1, the IF LHC and RHC signals
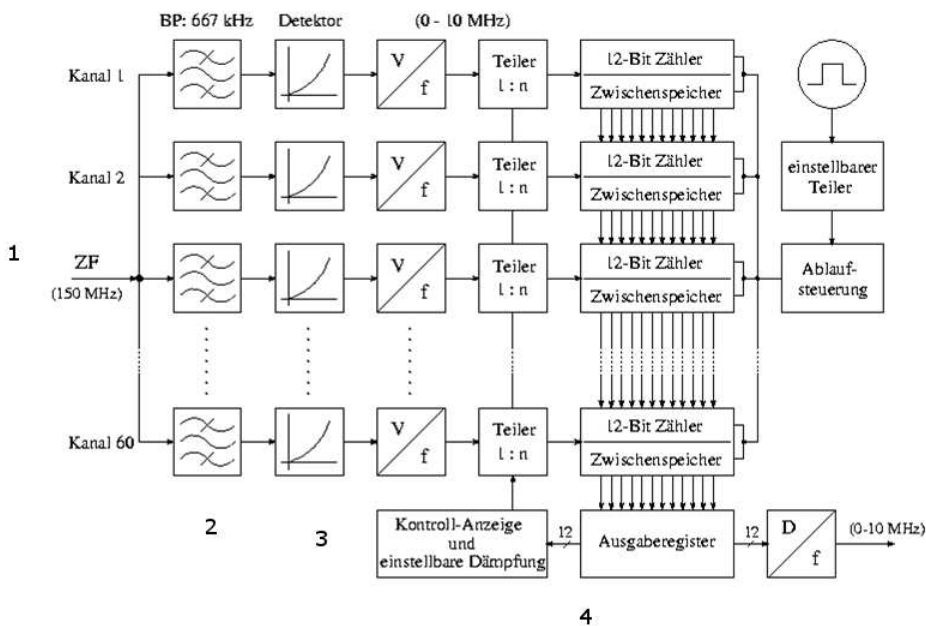
Figure A.3: **The steps of pulsar incoherent de-dispersion in PSE.**

passed through an adding polarimeter to the PSE. In 2, the 40 MHz total bandwidth is being split into 60 channels of 666 KHz each. In 3, the signals are being detected and in 4 they are digitally delayed and converted to a V/f signal.

A.1.2   EBPP

The Effelsberg-Berkeley Pulsar Processor (EBPP) (Backer et al. 1997) is the Effelsberg coherent de-dispersion machine as presented in Figure A.4. Following the letters on this figure we
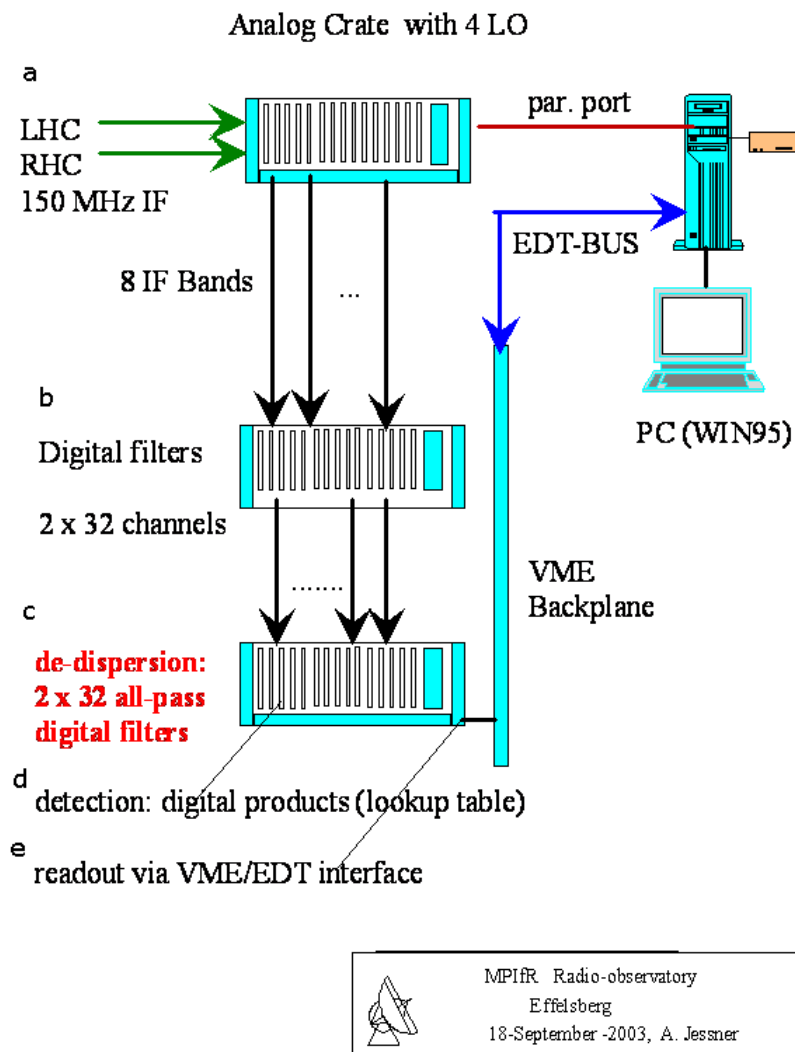

Figure A.4: **The steps of pulsar coherent de-dispersion in EBPP.**

can follow the procedure of coherent de-dispersion in EBPP. In a, splitting of the bandwidth into 8 sub-bands by analog splitters and filters is performed. In b, each sub-band is being digitally split and filtered again into 8 narrow band channels. In c, 1024-tap lateral all-pass filters are being used for dispersion removal of individual narrow band channels. In d, the digital signal

is square law detected using a programmable lookup table and in e, we transfer the data via VME-PC interface for storage and processing.

Bibliography

Abdo, A. A., Ackermann, M., Atwood, W. B., et al. 2009, ApJ, 699, 1171

Abramovici, A., Althouse, W. E., Drever, R. W. P., et al. 1992, Science, 256, 325

Angelakis, E. 2007, Ph.D. Thesis

Archibald, A. M., Stairs, I. H., Ransom, S. M., et al. 2009, Science, 324, 1411

Arzoumanian, Z., Joshi, K., Rasio, F. A., & Thorsett, S. E. 1996, in Astron. Soc. Pac., San Francisco, Vol. 105, IAU Colloq. 160, Pulsars: Problems and Progress, ed. S. Johnston, M. A. Walker, & M. Bailes, 525

Baade, W. & Zwicky, F. 1934, Proc. Nat. Acad. Sc., 20, 259

Backer, D. C. 1970, Nature, 228, 42

Backer, D. C., Dexter, M. R., Zepka, A., et al. 1997, PASP, 109, 61

Backer, D. C., Foster, R. F., & Sallmen, S. 1993, Nature, 365, 817

Backer, D. C., Kulkarni, S. R., Heiles, C., Davis, M. M., & Goss, W. M. 1982, Nature, 300, 615

Bailes, M., Harrison, P. A., Lorimer, D. R., et al. 1994, ApJ, 425, L41

Bailes, M., Johnston, S., Bell, J. F., et al. 1997, ApJ, 481, 386

Barish, B. C. 2000, Adv. Sp. Res., 25, 1165

Bassa, C. G., van Kerkwijk, M. H., & Kulkarni, S. R. 2006, A&A, 450, 295

Bell, J. F., Bailes, M., Manchester, R. N., et al. 1997, MNRAS, 286, 463

Bertotti, B., Carr, B. J., & Rees, M. J. 1983, MNRAS, 203, 945

Bhat, N. D. R., Bailes, M., & Verbiest, J. P. W. 2008, Phys. Rev. D, 77, 124017

Blandford, R. & Teukolsky, S. A. 1976, ApJ, 205, 580

Blandford, R. D., Narayan, R., & Romani, R. W. 1984, J. Astrophys. Astron., 5, 369

Burgay, M., D'Amico, N., Possenti, A., et al. 2003, Nature, 426, 531

Cairns, I. H., Johnston, S., & Das, P. 2001, ApJ, 563, L65

Callanan, P. J., Garnavich, P. M., & Koester, D. 1998, MNRAS, 298, 207

Camilo, F., Cognard, I., Ransom, S. M., et al. 2007a, ApJ, 663, 497

Camilo, F., Nice, D. J., Shrauner, J. A., & Taylor, J. H. 1996, ApJ, 469, 819

Camilo, F., Ransom, S. M., Halpern, J. P., et al. 2006, Nature, 442, 892

Camilo, F., Ransom, S. M., Peñalver, J., et al. 2007b, ApJ, 669, 561

Camilo, F., Reynolds, J., Johnston, S., et al. 2007c, ApJ, 659, L37

Caron, B. & et al. 1998, State of the Art of the VIRGO Experiment

Chadwick, J. 1932, Royal Society of London Proceedings Series A, 136, 692

Chatterjee, S., Brisken, W. F., Vlemmings, W. H. T., & et al. 2009, ApJ, 698, 250

Cordes, J. M. & Lazio, T. J. W. 2001, ApJ, 549, 997

Cordes, J. M. & Lazio, T. J. W. 2002, pre-print (astro-ph/0207156)

Cordes, J. M. & Lazio, T. J. W. 2003, http://xxx.lanl.gov/abs/astro-ph/0301598

Cudworth, K. M. & Hanson, R. B. 1993, AJ, 105, 168

D'Amico, N. 2000, in Astronomical Society of the Pacific Conference Series, Vol. 202, IAU Colloq. 177: Pulsar Astronomy - 2000 and Beyond, ed. M. Kramer, N. Wex, & R. Wielebinski, 27

Damour, T. 2007, submitted (arXiv:0704.0749)

Damour, T. & Deruelle, N. 1985, Ann. Inst. Henri Poincaré Phys. Théor, 43, 107

Damour, T. & Esposito-Farèse, G. 1992, Class. Quantum Grav., 9, 2093

Damour, T. & Esposito-Farese, G. 1993, Phys. Rev. Lett., 70, 2220

Damour, T. & Esposito-Farese, G. 1996, Phys. Rev. D, 54, 1474

Damour, T., Gibbons, G. W., & Taylor, J. H. 1988, Phys. Rev. Lett., 61, 1151

Damour, T. & Taylor, J. H. 1991, ApJ, 366, 501

Damour, T. & Taylor, J. H. 1992, Phys. Rev. D, 45, 1840

Danzmann, K. 2000, Adv. Sp. Res., 25, 1129

Danzmann, K. & et al. 1995, Geo 600 - a 600-M Laser Interferometric Gravitational Wave Antenna

Deller, A. T., Verbiest, J. P. W., Tingay, S. J., & Bailes, M. 2008, ApJ, 685, L67

Dicke, R. H. 1946, Rev. Sci. Instrument, 17, 268

Doroshenko, O., Lö hmer, O., Kramer, M., et al. 2001, A&A, 379, 579

Drake, F. D. & Craft, H. D. 1968, Nature, 220, 231

Driebe, T., Schoenberner, D., Bloecker, T., & Herwig, F. 1998, A&A, 339, 123

Duncan, R. C. & Thompson, C. 1992, ApJ, 392, L9

Dwarakanath, K. S. & Shankar, N. U. 1990, J. Astrophys. Astron., 11, 323

Edwards, R. T. & Stappers, B. W. 2002, A&A, 393, 733

Eisenhauer, F., Schödel, R., Genzel, R., et al. 2003, ApJ, 597, L121

Ergma, E., Sarna, M. J., & Gerskevits-Antipova, J. 2001, MNRAS, 321, 71

Esposito-Farese, G. 2005, in The Tenth Marcel Grossmann Meeting. On recent developments in theo-
    retical and experimental general relativity, gravitation and relativistic field theories, ed. M. Novello,
    S. Perez Bergliaffa, & R. Ruffini, 647

Feast, M. & Whitelock, P. 1997, MNRAS, 291, 683

Foster, R. S., Cadwell, B. J., Wolszczan, A., & Anderson, S. B. 1995, ApJ, 454, 826

Foster, R. S., Fairhead, L., & Backer, D. C. 1991, ApJ, 378, 687

Freire, P. C., Kramer, M., & Lyne, A. G. 2001, MNRAS, 322, 885

Gaensler, B. M., Madsen, G. J., Chatterjee, S., & Mao, S. A. 2008, Publications of the Astronomical
    Society of Australia, 25, 184

Gold, T. 1968, Nature, 218, 731

Hales, S. E. G., Baldwin, J. E., & Warner, P. J. 1993, MNRAS, 263, 25

Halpern, J. P., Gotthelf, E. V., Becker, R. H., Helfand, D. J., & White, R. L. 2005, ApJ, 632, L29

Hessels, J. W. T., Ransom, S. M., Stairs, I. H., et al. 2006, Science, 311, 1901

Hewish, A., Bell, S. J., Pilkington, J. D. H., Scott, P. F., & Collins, R. A. 1968, Nature, 217, 709

Hobbs, G. 2008, Classical and Quantum Gravity, 25, 114032

Hobbs, G., Edwards, R., & Manchester, R. 2006, Chinese Journal of Astronomy and Astrophysics Sup-
    plement, 6, 020000

Hobbs, G., Lorimer, D. R., Lyne, A. G., & Kramer, M. 2005, MNRAS, 360, 974

Holmberg, J. & Flynn, C. 2004, MNRAS, 352, 440

Hotan, A. W., Bailes, M., & Ord, S. M. 2004, MNRAS, 355, 941

Hotan, A. W., Bailes, M., & Ord, S. M. 2006, MNRAS, 369, 1502

Hotan, A. W., Long, S. R., Dickey, J. M., & Dolley, T. J. 2007, ApJ, 668, 449

Hulse, R. A. & Taylor, J. H. 1974, ApJ, 191, L59

Ibrahim, A. I., Markwardt, C. B., Swank, J. H., et al. 2004, ApJ, 609, L21

Janssen, G. 2009, Ph.D. Thesis

Janssen, G. H., Stappers, B. W., Kramer, M., et al. 2008, A&A, 490, 753

Jenet, F. A., Hobbs, G. B., Lee, K. J., & Manchester, R. N. 2005, ApJ, 625, L123

Jenet, F. A., Hobbs, G. B., van Straten, W., et al. 2006, ApJ, 653, 1571

Joshi, K. J. & Rasio, F. A. 1997, ApJ, 479, 948

Karastergiou, A., von Hoensbroech, A., Kramer, M., et al. 2001, A&A, 379, 270

Karuppusamy, R., Stappers, B., & van Straten, W. 2008, PASP, 120, 191

Kaspi, V. M., Lackey, J. R., Mattox, J., et al. 2000, ApJ, 528, 445

Kaspi, V. M., Taylor, J. H., & Ryba, M. 1994, ApJ, 428, 713

Keane, E. F. & Kramer, M. 2008, MNRAS, 391, 2009

Kijak, J., Gupta, Y., & Krzeszowski, K. 2007, A&A, 462, 699

Kopeikin, S. M. 1996, ApJ, 467, L93

Kouveliotou, C., Dieters, S., Strohmayer, T., et al. 1998, Nature, 393, 235

Kramer, M., Backer, D. C., Cordes, J. M., et al. 2004, New A Rev., 48, 993

Kramer, M., Jessner, A., Doroshenko, O., & Wielebinski, R. 1997, ApJ, 489, 364

Kramer, M., Karastergiou, A., Gupta, Y., et al. 2003, A&A, 407, 655

Kramer, M., Lange, C., Lorimer, D. R., et al. 1999a, ApJ, 526, 957

Kramer, M., Stairs, I. H., Manchester, R. N., et al. 2006, Science, 314, 97

Kramer, M., Stappers, B. W., Jessner, A., Lyne, A. G., & Jordan, C. A. 2007, MNRAS, 377, 107

Kramer, M., Wielebinski, R., Jessner, A., Gil, J. A., & Seiradakis, J. H. 1994, A&AS, 107, 515

Kramer, M., Xilouris, K. M., Camilo, F., et al. 1999b, 520, 324

Kramer, M., Xilouris, K. M., Lorimer, D. R., et al. 1998, ApJ, 501, 270

Kuijken, K. & Gilmore, G. 1989, MNRAS, 239, 571

Kuiper, L., Hermsen, W., Verbunt, F., & Belloni, T. 1998, A&A, 336, 545

Kuiper, L., Hermsen, W., Verbunt, F., et al. 2000, A&A, 359, 615

Löhmer, O., Lewandowski, W., Wolszczan, A., & Wielebinski, R. 2005, ApJ, 621, 388

Lange, C., Camilo, F., Wex, N., et al. 2001, MNRAS, 326, 274

Lazaridis, K., Jessner, A., Kramer, M., et al. 2008, MNRAS, 390, 839

Lazaridis, K., Wex, N., Jessner, A., et al. 2009, ArXiv e-prints:0908.0285

Löhmer, O., Jessner, A., Kramer, M., Wielebinski, R., & Maron, O. 2008, A&A, 480, 623

Löhmer, O., Kramer, M., Driebe, T., et al. 2004, A&A, 426, 631

Lommen, A. N., Kipphorn, R. A., Nice, D. J., et al. 2006, ApJ, 642, 1012

Lommen, A. N., Zepka, A., Backer, D. C., et al. 2000, ApJ, 545, 1007

Lorimer, D. R. 2005, Living Reviews in Relativity, http://relativity.livingreviews.org/Articles/lrr-2005-7/

Lorimer, D. R. & Kramer, M. 2005, Handbook of Pulsar Astronomy (Cambridge: Cambridge University Press)

Lorimer, D. R., Lyne, A. G., Festin, L., & Nicastro, L. 1995a, Nature, 376, 393

Lorimer, D. R., Nicastro, L., Lyne, A. G., et al. 1995b, ApJ, 439, 933

Lundgren, S. C., Cordes, J. M., Foster, R. S., Wolszczan, A., & Camilo, F. 1996, ApJ, 458, L33

Lundgren, S. C., Cordes, J. M., Ulmer, M., et al. 1995a, ApJ, 453, 433

Lundgren, S. C., Zepka, A. F., & Cordes, J. M. 1995b, ApJ, 453, 419

Lyne, A. G., Biggs, J. D., Brinklow, A., Ashworth, M., & McKenna, J. 1988, Nature, 332, 45

Lyne, A. G., Burgay, M., Kramer, M., et al. 2004, Science, 303, 1153

Lyne, A. G. & Graham-Smith, F. 2006, Pulsar Astronomy (Cambridge: Cambridge University Press)

Lyne, A. G., Manchester, R. N., Lorimer, D. R., & et al. 1998, MNRAS, 295, 743

Lyne, A. G., Manchester, R. N., & Taylor, J. H. 1985, MNRAS, 213, 613

Maitia, V., Lestrade, J.-F., & Cognard, I. 2003, ApJ, 582, 972

Malofeev, V. M., Shishov, V. I., Sieber, W., et al. 1996, A&A, 308, 180

Maron, O., Kijak, J., Kramer, M., & Wielebinski, R. 2000, A&AS, 147, 195

McKenna, J. & Lyne, A. G. 1988, Nature, 336, 226

McLaughlin, M. A., Rea, N., Gaensler, B. M., et al. 2007, ApJ, 670, 1307

Navarro, J., de Bruyn, G., Frail, D., Kulkarni, S. R., & Lyne, A. G. 1995, ApJ, 455, L55

Nicastro, L. & Johnston, S. 1995, MNRAS, 273, 122

Nicastro, L., Lyne, A. G., Lorimer, D. R., et al. 1995, MNRAS, 273, L68

Nicastro, L., Nigro, F., D'Amico, N., Lumiella, V., & Johnston, S. 2001, A&A, 368, 1055

Nice, D. J., Sayer, R. W., & Taylor, J. H. 1996, ApJ, 466, L87

Nice, D. J., Splaver, E. M., Stairs, I. H., et al. 2005, ApJ, 634, 1242

Nice, D. J., Stairs, I. H., & Kasian, L. E. 2008, in American Institute of Physics Conference Series, Vol. 983, 40 Years of Pulsars: Millisecond Pulsars, Magnetars and More, ed. C. Bassa, Z. Wang, A. Cumming, & V. M. Kaspi, 453–458

Nordtvedt, K. 1990, Phys. Rev. Lett., 65, 953

Oppenheimer, J. R. & Volkoff, G. 1939, Phys. Rev. E, 55, 374

Pacini, F. 1967, Nature, 216, 567

Paczyński, B. 1990, ApJ, 348, 485

Peters, P. C. 1964, Phys. Rev. Lett., 136, 1224

Phinney, E. S. 1992, Phil. Trans.:Phys. Sc. & Eng., 341, 39

Phinney, E. S. & Kulkarni, S. R. 1994, ARA&A, 32, 591

Radhakrishnan, V. & Cooke, D. J. 1969, ApL, 3, 225

Ransom, S. M., Camilo, F., Halpern, J. P., et al. 2007, Transient, wacky and strong radio pulses from a magnetar

Rasio, F. A. 1994, ApJ, 427, L107

Richer, H. B., Ibata, R., Fahlman, G. G., & Huber, M. 2003, ApJ, 597, L45

Riess, A. G., Macri, L., Casertano, S., & et al. 2009, ApJ, 699, 539

Sandhu, J. S., Bailes, M., Manchester, R. N., et al. 1997, ApJ, 478, L95

Sayer, R. W., Nice, D. J., & Taylor, J. H. 1997, ApJ, 474, 426

Serylak, M., Stappers, B. W., Weltevrede, P., et al. 2009, MNRAS, 176

Shklovskii, I. S. 1970, Soviet Ast., 13, 562

Sigurdsson, S. 1995, ApJ, 452, 323

Somer, A. 2000, in Astronomical Society of the Pacific Conference Series, Vol. 202, IAU Colloq. 177: Pulsar Astronomy - 2000 and Beyond, ed. M. Kramer, N. Wex, & R. Wielebinski, 17–20

Splaver, E. M., Nice, D. J., Arzoumanian, Z., et al. 2002, ApJ, 581, 509

Splaver, E. M., Nice, D. J., Stairs, I. H., Lommen, A. N., & Backer, D. C. 2005, 620, 405

Spruit, H. C. 2008, in American Institute of Physics Conference Series, Vol. 983, 40 Years of Pulsars: Millisecond Pulsars, Magnetars and More, ed. C. Bassa, Z. Wang, A. Cumming, & V. M. Kaspi, 391–398

Stairs, I. H., Thorsett, S. E., & Camilo, F. 1999, ApJS, 123, 627

Standish, E. M. 1998, JPL Planetary and Lunar Ephemerides, DE405/LE405, Memo IOM 312.F-98-048 (Pasadena: JPL), http://ssd.jpl.nasa.gov/iau-comm4/de405iom/de405iom.pdf

Standish, E. M. 2004, A&A, 417, 1165

Stappers, B. W., Bailes, M., Lyne, A. G., et al. 1996, 465, L119

Stappers, B. W., Bailes, M., Manchester, R. N., Sandhu, J. S., & Toscano, M. 1998, ApJ, 499, L183

Stappers, B. W., van Kerkwijk, M. H., Lane, B., & Kulkarni, S. R. 1999, ApJ, 510, L45

Taylor, J. H. 1992, Philosophical Transactions of the Royal Society of London, 341, 117-134 (1992), 341, 117

Taylor, J. H. & Cordes, J. M. 1993, ApJ, 411, 674

Thompson, C. 2008a, ApJ, 688, 1258

Thompson, C. 2008b, ApJ, 688, 499

Thompson, C. & Duncan, R. C. 1993, ApJ, 408, 194

Thompson, C., Duncan, R. C., Woods, P. M., et al. 2000, ApJ, 543, 340

Thorsett, S. E. 1991a, ApJ, 377, 263

Thorsett, S. E. 1991b, PhD thesis, Princeton University

Thorsett, S. E., Arzoumanian, Z., Camilo, F., & Lyne, A. G. 1999, ApJ, 523, 763

Toscano, M., Britton, M. C., Manchester, R. N., et al. 1999a, ApJ, 523, L171

Toscano, M., Sandhu, J. S., Bailes, M., et al. 1999b, MNRAS, 307, 925

van Haasteren, R., Levin, Y., McDonald, P., & Lu, T. 2009, MNRAS, 395, 1005

Verbiest, J. P. W., Bailes, M., van Straten, W., & et al. 2008, ApJ, 679, 675

Verbunt, F., Kuiper, L., Belloni, T., et al. 1996, A&A, 311, L9

Voûte, J. L. L., Kouwenhoven, M. L. A., van Haren, P. C., et al. 2002, A&A, 385, 733

Wall, J. V. & Jenkins, C. R. 2003, Practical Statistics for Astronomers (Cambridge: Cambridge University Press)

Webb, N. A., Olive, J.-F., Barret, D., et al. 2004, A&A, 419, 269

Weisberg, J. M. & Taylor, J. H. 1984, Phys. Rev. Lett., 52, 1348

Weisberg, J. M. & Taylor, J. H. 2005, in Astronomical Society of the Pacific Conference Series, Vol. 328, Binary Radio Pulsars, ed. F. A. Rasio & I. H. Stairs, 25

Weltevrede, P., Stappers, B. W., & Edwards, R. T. 2007, A&A, 469, 607

Wex, N., Johnston, S., Manchester, R. N., et al. 1998, MNRAS, 298, 997

Will, C. 2001, Living Reviews in Relativity, 4, 1, uRL (Cited on 2006/02/01): http://www.livingreviews.org/Irr-2001-4

Will, C. M. 1993, Theory and Experiment in Gravitational Physics (Cambridge: Cambridge University Press)

Williams, J. G., Turyshev, S. G., & Boggs, D. H. 2004, Phys. Rev. Lett., 93, 261101

Wolszczan, A., Doroshenko, O., Konacki, M., et al. 2000, ApJ, 528, 907

Wolszczan, A. & Frail, D. A. 1992, Nature, 355, 145

Xilouris, K. M., Kramer, M., Jessner, A., Wielebinski, R., & Timofeev, M. 1996, A&A, 309, 481

Zavlin, V. E. 2006, ApJ, 638, 951

Acknowledgments

I would like to express my gratitude to certain people for the various ways they helped me during the course of my PhD studies.

First of all, I would like to thank from the bottom of my heart my scientific advisors. Dr. Axel Jessner for always being there when needed, advising and sharing knowledge, for the fruitful scientific and not only discussions and for buying me "frikadellen" lunch at the Effelsberg IMBISS. Also, Prof. Dr. Michael Kramer for his constant help and directions, even from the distance, for all the things he taught me in our discussions and for the extremely useful but also fun travels to Manchester. I thank them for being supportive and understanding and for inspiring me to become better.

I would also like to thank, Prof. Dr. Anton Zensus and Prof. Dr. Andreas Eckart for being in my thesis committee and for the valuable time they spent in reading my manuscript and discussing science with me. Also Prof. Dr. Claus Kiefer for being willing to participate in my examination committee besides his busy schedule. Finally, Dr. Macarena Garcia Marin for kindly accepting to be the final member of my examination committee.

I want to thank Prof. Dr. Zensus additionally for accepting me at the VLBI group in the MPIfR in Bonn and for providing me all the desired support throughout my studies. There have been three beautiful and creative years and for that I want to thank all my colleagues at the VLBI group for their help and friendship.

I want also to thank Dr. Norbert Wex for the extremely productive collaboration in the past few months, for his more than precious theoretical help and for revealing me the peculiar and exciting field of the alternative gravity theories. In addition, Dr. Paulo Freire for the valuable discussions and his valid comments on my work.

I would also like to thank all my EPTA collaborators, Jason, Gemma, Rudger, Ben, Andew, Mark, Chris, Tim, Sotiris, Ismael, Gilles, Gregory, Rob, Andrea, Marta, Maura and Alessandro. Thanks for all the pulsar data and knowledge sharing, the fruitful discussions, your comments on my papers and most important the fun in our EPTA meetings.

I must not forget to thank my diploma advisor Prof. John H. Seiradakis for introducing me to the fascinating world of pulsars and to scientific research.

I really want to thank Dr. Alex Krauss, all the operators and staff at the Effelsberg radiotelescope for their essential help in my observations, for the discussions and the technical information they were providing me during my visits to the telescope. In addition, all the operators at Westerbork, Jodrell Bank and Nançay radiotelescopes for their help with our pulsar observations.

Erklärung

Ich versichere, daß ich die von mir vorgelegte Dissertation selbständig ange- fertigt, die benutzten Quellen und Hilfsmittel vollständig angegeben und die Stellen der Arbeit – einschließlich Tabellen, Karten und Abbildungen –, die anderen Werken im Wortlaut oder dem Sinn nach entnommen sind, in jedem Einzelfall als Entlehnung kenntlich gemacht habe; daß diese Dissertation noch keiner anderen Fakultät oder Universität zur Prüfung vorgelegen hat; daß sie – abgesehen von unten angegebenen Teilpublikationen – noch nicht veröffentlicht worden ist sowie, daß ich eine solche Veröffentlichung vor Abschluß des Promotionsverfahrens nicht vornehmen werde. Die Bestimmungen dieser Promotionsordnung sind mir bekannt. Die von mir vorgelegte Dissertation ist von Prof. Dr. Anton J. Zensus betreut worden.

Köln, 20. 08. 2009

Teilpublikationen

Lazaridis, K., Wex, N., Jessner, A., Kramer, M., Stappers, B. W., Janssen, G. H., Desvignes, G., Purver, M. B., Cognard, I., Theureau, G., Lyne, A. G., Jordan, C. A., Zensus., J. A.:
"Generic tests of the existence of the gravitational dipole radiation and the variation of the gravitational constant", accepted in MNRAS, 2009 (eprint arXiv:0908.0285)

Lazaridis, K., Jessner, A., Kramer, M., Stappers, B. W., Lyne, A. G., Jordan, C. A., Serylak, M., Zensus, J. A.:
"Radio spectrum of the AXP J1810-197 and of its profile components", MNRAS, 390, 839, 2008

Lazaridis, K., Jessner, A., Kramer, M., Stappers, B. W., Lyne, A. G., Jordan, C. A., Serylak, M., Zensus, J. A.:
"Flux density spectrum of the magnetar AXP J1810-197", Proceedings of "Bursts, Pulses and Flickering: wide-field monitoring of the dynamic radio sky", pp. 42, 2008

Weitere Publikationen

Serylak, M., Stappers, B. W., Weltevrede, P., Kramer, M., Jessner, A., Lyne, A. G., Jordan, C. A., **Lazaridis, K.**, Zensus, J. A.:
"Simultaneous multifrequency single-pulse properties of AXP XTE J1810-19", MNRAS, 394, 295, 2009.

Purver, M. B., Jordan, C. A., Kramer, M., Lyne, A. G., Stappers, B. W., Jessner, A., **Lazaridis, K.**, Janssen, G. H., Karuppusamy, R., Cognard, I., Desvignes, G., Theureau, G., Burgay, M., Corongiu, A., DAmico, N., Possenti, A.:

"The European Pulsar Timing Array", Proceedings of "From planets to dark energy: the modern radio universe", pp. 125, 2007

Lebenslauf

Personalangaben

Name:	Kosmas Lazaridis
Anschrift:	Max-Planck-Institut für Radioastronomie
	Auf dem Hügel 69, 53121 Bonn
E-mail:	klazarid@mpifr-bonn.mpg.de
Geburtsdatum und -ort:	15. 04. 1981. in Thessaloniki, Griechenland

Ausbildung

Seit Sep. 2006	Promotionstudent an der Universität zu Köln und dem Max-Planck-Institut für Radioastronomie wiss. Betreuer: Prof. Dr. Anton J. Zensus, Dr. Axel Jessner, Prof. Dr. Michael Kramer Titel: *"Multi-Telescope Studies of Neutron Stars"*
2000 - 2006	Diplom in Physik (Ptychion) an der Aristotle Universität von Thessaloniki, Griechenland wiss. Betreuer: Prof. Dr. John H. Seiradakis Titel: *"Pulsar Nulling Quantitative Analysis"*
1996 - 1999	2nd Gymnasium von Ano Toumba, Thessaloniki, Griechenland

Stipendium:

Seit Sep. 2006	Stipendium der *International Max Planck Research School (IMPRS)*
2004	Stipendium der Staat-Stipendium-Stiftung von Griechenland